Light Scattering Study of Many-Body Interactions in Two Dimensional Electronic Systems

by

Lushalan Boy-Yu Liao

B.S., California Institute of Technology (1988)

Submitted to the Department of Physics
in partial fulfillment of the requirements for the degree of

Doctor of Philosophy

at the

MASSACHUSETTS INSTITUTE OF TECHNOLOGY

August 1994

Author .....
Department of Physics
August 5, 1994

Certified by .....
D. Heiman
Research Scientist, FBNML
Thesis Supervisor

Certified by .....
J. David Litster
Professor
Thesis Supervisor

Accepted by .....
George F. Koster
Chairman, Departmental Committee on Graduate Students

Light Scattering Study of Many-Body Interactions in Two Dimensional Electronic Systems

by

Lushalan Boy-Yu Liao

Submitted to the Department of Physics
on August 5, 1994, in partial fulfillment of the
requirements for the degree of
Doctor of Philosophy

Abstract

Recent advances in material fabrication techniques such as molecular beam epitaxy (MBE) have led to the construction of quantum wells. These wells can be remotely doped to creat electronic systems in which the many-body interactions are dominant. These reduced-dimensionality electron systems have surprised researchers with many novel phenomena. In particular, two-dimensional systems exhibit the integer and fractional quantum hall effects. In this thesis, I have conducted theoretical and experimental studies of the many-body interactions in two types of two-dimensional systems: asymmetrically doped single quantum wells and wide parabolic quantum wells. By studying the collective modes with inelastic light scattering, various types of approximations needed to calculate the effect of electron-electron interactions are quantified. Excitations in single quantum wells can be modelled with time-dependent Hartree-Fock calculations, while wide parabolic quantum wells are more easily modelled using hydrodynamics.

Thesis Supervisor: D. Heiman
Title: Research Scientist, FBNML

Thesis Supervisor: J. David Litster
Title: Professor

Acknowledgments

It is with great pleasure that I write this section to try and thank the people without whom I would not have been able to finish the thesis. First and foremost, I would like to thank my parents for their unwavering faith and support. I would also like to thank my brother for showing me the way to physics and then showing that there is life after physics. I am grateful to my mentor K.K. Thornber for being always encouraging and optimistic even when it looks as though I may never get out of graduate school alive. Many thanks to Allan MacDonald, without whom I would have never been able to explain a big part of my experimental work. Of course, I am very thankful to A. Pinczuk, Art Gossard, and P. Hopkins for providing the great samples, without which there would not even be a thesis. Many thanks to Margaret O'Meara for many hours of equitation, rescuing my plants and listening to my gripes about everything. I am also very grateful to the entertaining company of Gervais, Hide, Irene (the landlady) and George. Last, but not least, I am grateful to my advisor D. Heiman for making my graduate school experience as pleasant as possible.

Contents

1 Introduction **11**

1.1 Quantum Hall Effects and Composite Fermion Approach 12

1.2 Optical Experiments and Collective Modes 19

1.3 Outline of the Thesis 25

2 Hartree-Fock Formalism in Two Dimensional Systems **27**

2.1 Parabolic Confinement Model 28

2.1.1 Transformation of the parabolic Hamiltonian 29

2.1.2 Many-Body Wave Functions 33

2.1.3 Excitation Energy 34

2.1.4 Application to $\Delta n_\sigma = 1$ 37

2.2 Realistic Self-Consistent Calculation 44

2.2.1 Hamiltonian 44

2.2.2 Self-Consistent Single-Particle States 47

2.2.3 Correction to the Single-Particle Energy 48

2.2.4 Random-phase approximation 51

2.2.5 Exchange 52

2.2.6 Local-field correction 53

3 Square Quantum Wells **59**

3.1 Experimental 60

3.1.1 samples 60

3.1.2 Light-scattering set-up 60

3.2 Tilted Magnetic Field 63

4 Wide Parabolic Wells **74**

4.1 Hydrodynamic Model 76

4.1.1 Equilibrium 77

4.1.2 Linearized Problem 78

4.2 Experiment 81

4.2.1 Sample 81

4.2.2 Raman Scattering 85

4.2.3 Results 85

4.2.4 Discussion 87

5 Conclusions **94**

A Coulomb Correction **96**

A.1 Evaluation of $E(\vec{k}, \sigma', \sigma, p)$ 98

A.2 Expectation Values of Intra-Level Operators 99

A.2.1 $\nu = 2$ 102

A.2.2 $\nu = 1$ 104

B Evaluation of $F(n_+, n_-; m_+, m_- : \vec{k})$ **106**

B.1 Semi-Classical States 107

B.2 Evaluation of Matrix Elements 109

List of Figures

1-1 Standard experimental configuration for measuring QHE 13

1-2 Comparison of the classical Hall resistance and the quantum Hall effect. 14

1-3 IQHE and FQHE after Tsui, Stormer, and Gossard 16

1-4 Expected fractions in FQHE from the composite fermion theory . . . 20

1-5 Photoluminescence anomaly at $\nu = 1$ after Dahl *et. al.* 22

1-6 Roton density of states at $\nu = 2$ after Pinczuk *et. al.* 24

2-1 The dispersion of the singlet and triplet excitations. The effective mass is 0.067 times the bare electron mass. The IS transition energy at zero tilt angle is taken to be $27meV$ The curves are calculated with $\nu = 2$ and $B_\perp = 5T$. 40

2-2 The dependence of the singlet and triplet energy as the function of the tilt angle. The in-plane wave vector value is $\frac{0.05}{\ell_o}$. The effective mass is 0.067 times the bare electron mass. The IS transition energy at zero tilt angle is taken to be $27meV$ The curves are calculated with $\nu = 2$ and $B_\perp = 5T$. 42

2-3 The dependence of the singlet and triplet energy as the function of the tilt angle. The in-plane wave vector value is $\frac{0.04}{\ell_o}$. The effective mass is 0.067 times the bare electron mass. The IS transition energy at zero tilt angle is taken to be $27meV$ The curves are calculated with $\nu = 2$ and $B_\perp = 7.2T$. 43

2-4 The dispersion of the charge density and spin flip excitations. The effective mass is 0.067 times the bare electron mass. The IS transition energy at zero tilt angle is $27meV$. The curves are calculated with $\nu = 1$ and $B_\perp = 10T$. 45

2-5 The dispersion of the singlet and triplet excitations. The effective mass is 0.067 times the bare electron mass. The parameters used in the numerical calculation is listed in table 3-1. The curves are calculated with $\nu = 2$ and $B_\perp = 5T$. 55

2-6 The dispersion of the singlet and triplet excitations at 30 deg tilt angle. The effective mass is 0.067 times the bare electron mass. The parameters used in the numerical calculation is listed in table 3-1. The curves are calculated with $\nu = 2$ and $B_\perp = 5T$. 56

2-7 The dispersion of the singlet and triplet excitations at 60 deg tilt angle. The effective mass is 0.067 times the bare electron mass. The parameters used in the numerical calculation is listed in table 3-1. The curves are calculated with $\nu = 2$ and $B_\perp = 5T$. 58

3-1 Two-fiber optical probe 61

3-2 Optical dewar set up for light scattering. 62

3-3 Resonant Raman spectra at 60 ^{o} tilt angle for sample A at various filling factor values. 65

3-4 Temperature dependence at 60 ^{o} tilt angle for sample A. 66

3-5 Raman spectra at various tilt angles for the higher density sample. . . 67

3-6 Resonant Raman spectra at 60 ^{o} tilt angle for sample A. 68

3-7 The curves are the energy curves for the singlet and triplet excitations as a function of tilt angle for sample A. The in-plane wave vector value is taken to be $|k_\perp|\ell_o = 0.05$. 70

3-8 The curves are the energy curves for the singlet and triplet excitations as a function of tilt angle for sample B. The curves are calculated with $|k_\perp|\ell_o = 0.04$. 71

3-9 The solid dots are the experimental spectra while the dashed and solid curves are the calculated density of states. The parameters used for the calculation are those of sample B. 73

4-1 Schematic diagram of the potential profile of the parabolic quantum well. 82

4-2 Schematic diagram of the superlattice structure of the parabolic quantum well. The shaded layers are made of $Al_{0.3}Ga_{0.7}As$ while the white region is made of GaAs. 84

4-3 Typical inelastic light scattering spectra from $GaAs/Al_xGa_{1-x}As$ parabolic quantum well. Representative spectra for $qa = 0.05$ at B=5 T, where $a = 380\mathring{A}$ is half the well width and q is the in-plane wave vector. The spectra are labeled by the exciting laser energy. The temperature for the experiment was 1.6 K. 86

4-4 Inelastic light scattering spectra from a wide $GaAs/Al_xGa_{1-x}As$ parabolic quantum well. Representative spectra (normalized) for $qa = 0.05$ at various perpendicular magnetic fields, where $a = 380\mathring{A}$ is half the well width and q is the in-plane wave vector. The spectra were taken with laser energy near 1550 meV and temperature of 1.6 K. The laser energy was varied slightly at the different magnetic fields. 88

4-5 Inelastic light scattering spectra from a wide $GaAs/Al_xGa_{1-x}As$ parabolic quantum well. Representative unnormalized spectra for $qa = 0.21$ at various magnetic fields. The laser is set at 1550 meV. The solid curves are Gaussian line-shape fits to the experimental spectra, including a substantial background due to photoluminescence. 89

4-6 The solid curves represent the calculated odd-symmetry density oscillation modes of a wide parabolic quantum well in the hydrodynamic model with hard-wall boundary conditions. We used 10.8 meV as the value of the bare harmonic energy, and $qa = 0.05$. 91

4-7 The solid curves represent the calculated odd-symmetry density oscillation modes of a wide parabolic quantum well in the hydrodynamic model with hard-wall boundary conditions. We used 10.6 meV as the value of the bare harmonic energy and $qa = 0.21$. The insets are the normalized density fluctuations inside the well for the odd-symmetry modes at low fields (left hand side) and high fields (right hand side).. 92

4-8 Theoretical wave vector dispersion curves and experimental points for the lowest two odd-symmetry intersubband plasma modes at various magnetic fields. 93

List of Tables

2.1 Parameters Used in Parabolic Model Calculations 37

3.1 Single Quantum Well Sample Parameters 60

Chapter 1

Introduction

Recent advances in material fabrication techniques have allowed physicists to study new material systems which present novel physical phenomena. In particular, the molecular beam epitaxy (MBE) has allowed crystal growers to tailor material systems with desired optical and electrical properties [33]. One of the most interesting systems that have been studied extensively is the two-dimensional electron gas (2DEG). Applications of 2DEG systems made with GaAs/$Al_xGa_{1-x}As$ include extremely fast and low power transistors, analog amplifiers operating up to 60 gigahertz [5], and optical devices. In attempts to better understand these 2DEG systems, interesting phenomena such as the Integer Quantum Hall Effect (IQHE) and the Fractional Quantum Hall Effect (FQHE) were observed by von Klitzing *et. al.* [36] and Tsui, Stormer and Gossard [34]. Interesting new concepts such as anyons, fractional statistics, and composite fermions were introduced. The study of 2DEG systems not only broadens basic understanding of physics but also advances the development of new devices based on 2DEG systems. In order to take advantage of the unique properties of 2DEG systems in device design, it is essential to be able to quantify the behavior of electrons. The purpose of this manuscript is to study the optical properties of 2DEG system. This thesis describes the use of inelastic light scattering in the study of elementary excitations in 2DEG systems and how optical spectroscopy can be used to quantify exchange and correlation effects beyond the usual self-consistent Hartree approximation.

1.1 Quantum Hall Effects and Composite Fermion Approach

Nearly a century after the discovery of the Hall effect, IQHE and FQHE were observed in 2DEG. 2DEG refers to electronic systems where the motion in one of the dimension is quantized due to an externally imposed potential. When electrons are subjected to an externally applied magnetic field, the system kinetic energy in the direction perpendicular to the magnetic field becomes quantized and its density of state becomes highly singular. As the result of this highly singular density of states which is periodic in $1/H$, many properties of the system also oscillate as a function of $1/H$. When electrons in 2DEG are subjected to extremely high magnetic field perpendicular to the 2DEG, their kinetic energy is quantized in the remaining two directions and they exhibit dramatic deviation from classical behavior. The usual configuration for the measurement of IQHE has crossed electric ($\vec{E}$) and magnetic ($\vec{B}$) fields. Figure (1-1) shows the standard configuration for measuring the Hall effect. $\vec{B}$ in this case will be out of the plane of the paper while $\vec{E}$ is directed along the horizontal. If we make the relativistic transformation to a reference frame with the velocity $\vec{v} = \frac{c\vec{E}\times\vec{B}}{B^2}$, the electric field vanishes [15]. This is the usual $\vec{E} \times \vec{B}$ drift. For a system with translational invariance, the current density will be

$$\vec{j} = -n_s e\vec{v} \tag{1.1}$$

$$= \frac{n_s ec\vec{E} \times \vec{B}}{B^2}. \tag{1.2}$$

The current is directed perpendicular to both the magnetic field and the electric field. The magnitude of the coefficient relating the current density to the electric field is just the Hall resistivity. In two-dimensions, the Hall resistance is the same as the Hall resistivity. We conclude that the Hall resistance should be a linear function of the perpendicular magnetic field, $\vec{B}$.

$$R_h = \frac{B}{n_s ec}, \tag{1.3}$$

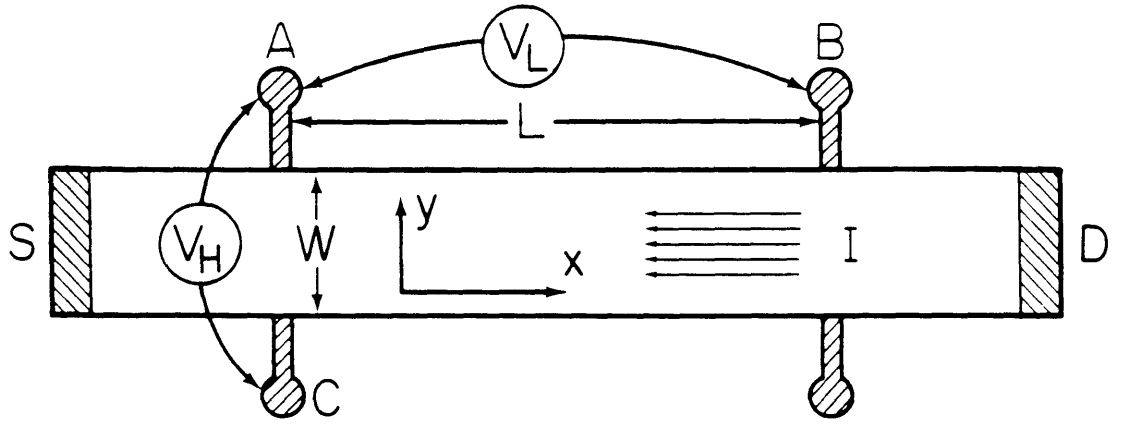

Figure 1-1: Standard experimental configuration for measuring QHE

where n_s is the charge density. The argument leading to Eq. (1.3) is an extremely general argument. It depends only on translational invariance and gauge invariance, and is entirely independent of the electron-electron interaction. Eq. (1.3) is correct in 2DEG only for some special magnetic field values. It is observed that as one sweeps the magnetic field perpendicular to the plane of 2DEG, there are plateaus of constant Hall resistance while the longitudinal resistance simultaneously goes to zero. The values of the Hall resistance at the plateaus are precisely quantized to the values of

$$R_h = \frac{h}{be^2}. \tag{1.4}$$

The values of b in Eq. (1.4) can either be a positive integer or some rational fraction with odd denominators. If b is an integer, it is the IQHE. If b is defined as

$$b = \frac{b_{cf}}{2pb_{cf} \pm 1}, \tag{1.5}$$

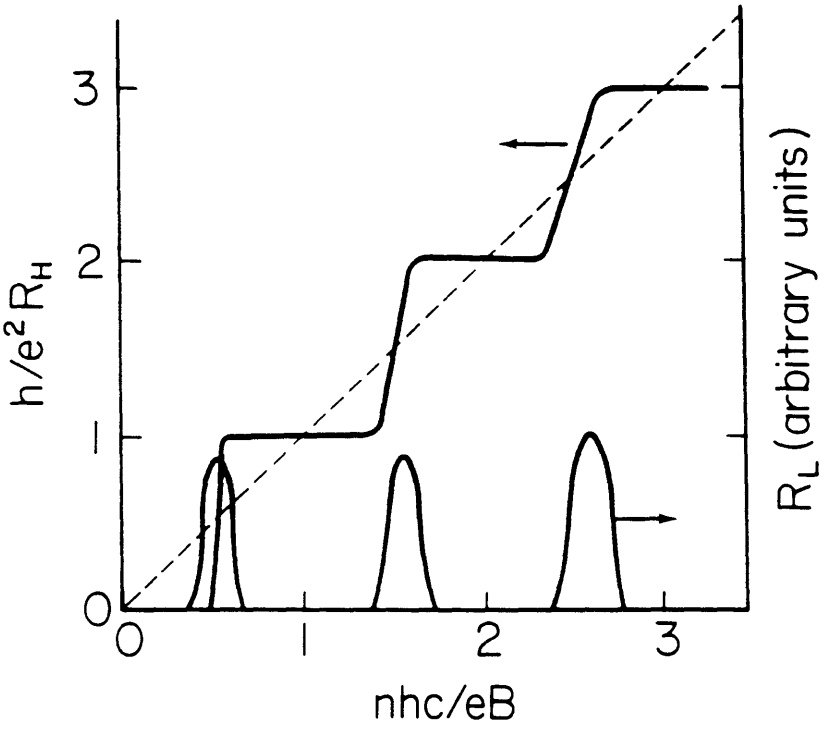

Figure 1-2: Comparison of the classical Hall resistance and the quantum Hall effect.

then it is the FQHE. In Eq. (1.5), p is an integer and b_{cf} is the pseudo Landau-level index number which will be discussed later. The classical and the quantum Hall effects coincide in value only at integral filling factors where every Landau level is either completely filled or completely empty. Figure 1-2 compares Eq. (1.3) with a schematic plot of IQHE. The dashed line plots Eq. (1.3) while the solid line plots what one would observe. The presence of the quantized Hall Resistance plateaus is quite striking. It is a robust phenomena. The quantization of the Hall resistance is completely independent of the material parameters and insensitive to the type

or the location of the impurities as long as the concentration of impurities is not enough to localize all states. Since we derived Eq. (1.3) with only the argument of translational and gauge invariance, we expect that deviation from Eq. (1.3) can only result from broken translational invariance. In beautiful thought experiments [11, 21], Laughlin demonstrated that IQHE can indeed be derived from gauge invariance and the existence of electronic mobility gap. The manifestation of IQHE depends only on the presence of impurities which break the translational invariance and produce the mobility gaps. Without the impurities the plateaus would have no width and one would not observe the striking plateaus as in Fig. 1-2. Instead, one would observe the dashed curve which is a plot of Eq. (1.3).

Figure 1-3 shows the data for both FQHE and IQHE. Phenomenologically, they are very similar: they both exhibit precisely quantized Hall resistance plateaus and dissipationless current flow. On the other hand, the physical principles underlying the FQHE is very different from IQHE. IQHE is explained as a non-interacting electron gas in the presence of mobility gaps. The quantization of the Hall plateau can be interpreted as a measure of the quantization of the electron charge. FQHE, on the other hand, is the result of many-body interaction and observed only in high-mobility (low scattering) samples. In contrast to IQHE, the presence of excessive impurities destroys FQHE. It depends critically on electron-electron interaction [30] for the formation of its strongly-correlated incompressible electron liquid ground state. It appears as though the two phenomena have very different origins while the experimental manifestations of the two phenomena are tantalizingly similar.

In addition to exhibiting precisely quantized Hall plateaus with simultaneous longitudinal resistance minima, it has been shown that IQHE and FQHE have similar scaling behavior [16] in the transition region between resistance minima. Since IQHE and FQHE are similar phenomenologically, it would be satisfying to find some unifying picture of the two phenomena. In the attempt to study this problem, it is useful to look to the study of Fermi liquids by the Landau approach. It consists of replacing the strongly interacting liquid with non-interacting gas of quasi-particles. Instead of attacking the complete problem with the full many-body treatment, one assumes

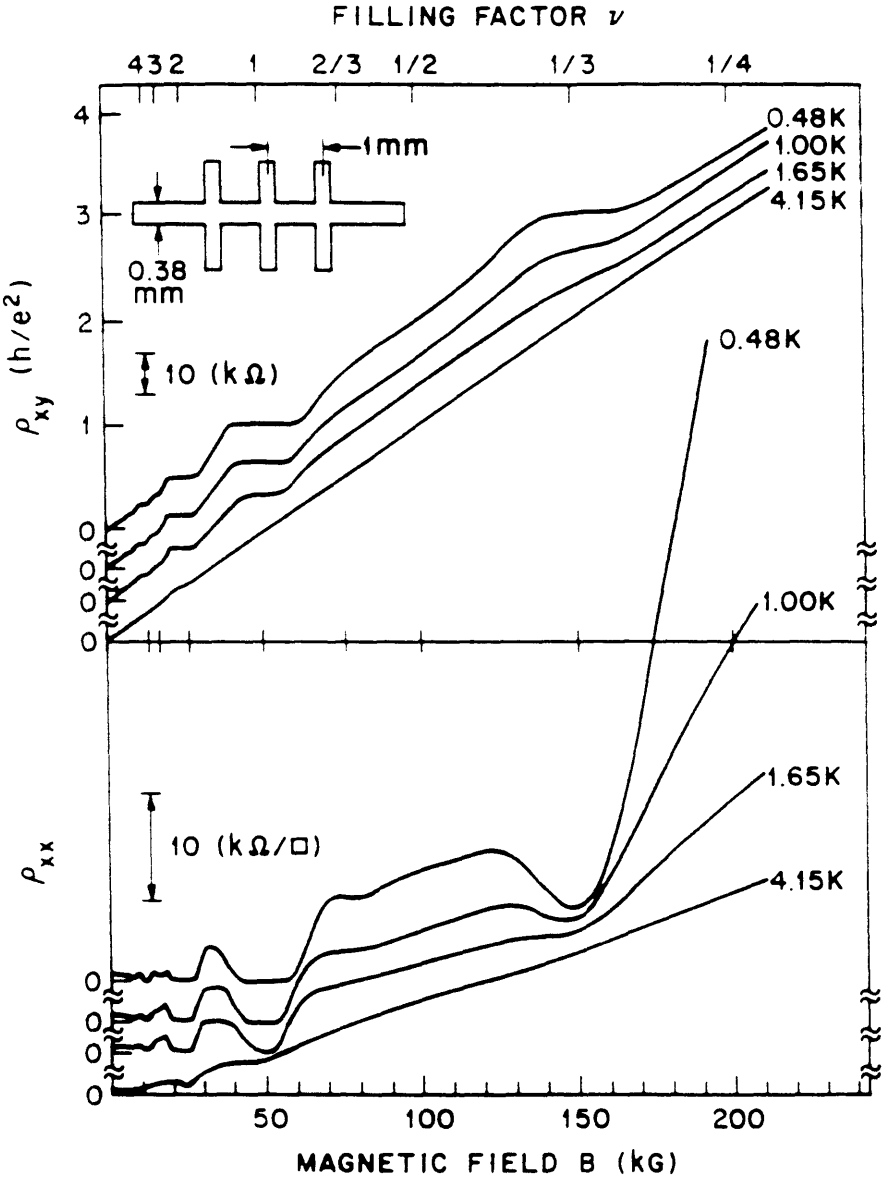

Figure 1-3: IQHE and FQHE after Tsui, Stormer, and Gossard

that the system can instead be described as a collection of weakly interacting quasi-particles. To the lowest order in the interaction of quasi-particles, one assumes the the quasi-particles are non-interacting. The quasi-particles are not the same as the bare interacting particles, but they are dressed particles interacting with each other weakly. In FQHE, these quasi-particles are fractionally charged. We are guided to this conclusion by the fact that the quantization of the IQHE plateaus are due to the charge quantization of the electrons. In IQHE, the quasi-particles are just the free electrons. Similarly, it is natural to think that the quantization of the FQHE plateaus is due to the charge quantization of the quasi-particles. It is now possible to formulate the FQHE in a similar manner as IQHE. The connecting link, the quasi-particle, is the composite fermion. The "single particle" wave function of the composite fermion is,

$$\tilde{\beta}_{n,l}(\vec{r}_j) = \prod_{k \neq j} (\xi_k - \xi_j)^p \beta_{n,l}(\vec{r}_j). \tag{1.6}$$

In Eq.(1.6), the index k is varied from 1 to $\mathcal{N}$ where $\mathcal{N}$ is the total number of electrons in the system. The function $\beta_{n,l}(\vec{r}_j)$ is the wave function of the nth Landau level. The index l labels the different states within a Landau Level. The variable ξ in Eq. (1.6) is the complex coordinate, defined as $\xi = x - iy$. The exact form of the wave function depends on the gauge choice. In order to count the degeneracy of a level, we must chose a gauge. Let us consider the case of symmetric gauge. In this gauge, the vector potential is defined as: $\vec{A} = (B/2)(-y\hat{e_x}, x\hat{e_y}, 0\hat{e_z})$. The lowest Landau level states are,

$$\beta_{0,l} = \frac{\xi^l}{\sqrt{2\pi 2^l l!}} e^{-\frac{1}{4}\xi\xi^*} \tag{1.7}$$

It can be shown by a simple integration that the expectation value of $\xi\xi^*$ with eigen-state of $\beta_{0,l}$ is,

$$\langle \xi\xi^* \rangle_l = 2(l+1)r_0^2 \tag{1.8}$$

where $r_0 = \sqrt{\frac{\hbar c}{eB}}$ is the magnetic length. Thus, the weight of the wave function $\beta_{0,l}$ is located at the radius of $R_l = \sqrt{2(l+1)}r_0$. To calculate the maximum allowed number for l in a sample with radius of R, we must require that the center of the

wave function be less than R,

$$l_{max} = \frac{R^2}{2r_0^2}. \tag{1.9}$$

In Eq. (1.9), we have dropped a factor of 1 in comparison to l_{max} in the thermodynamic limit. We can construct the many-body wave function from Eq. (1.6). Since the composite fermions are fermions, they must obey the Pauli exclusion principle. One possibility is to use the "single particle" wave function from Eq. (1.6) to build the slater determinant. The many-body wave function can be defined as,

$$\tilde{\Phi}_{b_{cf}} = \prod_{k,j}^{k\neq j}(\xi_j - \xi_k)^p \Phi_{b_{cf}} \tag{1.10}$$

$$= \prod_{k<j}(\xi_j - \xi_k)^{2p} \Phi_{b_{cf}} \tag{1.11}$$

In Eq. (1.11), $\Phi_{b_{cf}}$ is the slater determinant of the electron wave functions $\beta_{n,l}(\vec{r_j})$. The number b_{cf} is the integral filling factor of the composite fermion and we must now relate it to the fractional filling factor of the electrons. Due to the vortex factor $(\xi_j - \xi_k)^{2p}$ in Eq. (1.11), the center of the wave function is shifted, $R^{cf}_{l^{cf}} = \sqrt{2(l^{cf} + 2p\mathcal{N})}r_0$. In a sample with radius R, we must require the the center of the composite fermion to be less than R,

$$l^{cf}_{max} = l_{max} - 2p\mathcal{N}. \tag{1.12}$$

The true filling factor of the electrons is defined as $\mathcal{N}/l_{max}$. Similarly, the filling factor of the composite fermion is defined as $\mathcal{N}/l^{cf}_{max}$. Thus, the true filling factor is,

$$b = \frac{\mathcal{N}}{l_{max}} \tag{1.13}$$

$$= \frac{\mathcal{N}}{l^{cf}_{max} + 2p\mathcal{N}} \tag{1.14}$$

$$= \frac{\frac{\mathcal{N}}{l^{cf}_{max}}}{1 + \frac{2p\mathcal{N}}{l^{cf}_{max}}} \tag{1.15}$$

$$= \frac{b_{cf}}{1 + 2pb_{cf}} \tag{1.16}$$

The previous equation describes the attachment of a positive vortex. It is also possible

to attach anti-vortex. In the case of anti-vortex, the sign of b_{cf} is reversed. Thus, the possible fractional filling factor is,

$$b = \frac{b_{cf}}{2pb_{cf} \pm 1}. \tag{1.17}$$

This is just Eq. (1.5). Eq. (1.11) and Eq. (1.5) are the main result of the composite fermion theory. It relates the composite fermion wave function with the non-interacting electron wave function and it clearly predicts the hierarchy as a function of the pseudo-filling factor b_{cf} and a vortex parameter p. The strongly correlated liquid of interacting electrons in the FQHE state can be thought of as a weakly interacting gas of the composite fermions. Now the FQHE of the electrons is simply the result of non-interacting composite fermions in the presence of mobility gaps for the composite fermions. The FQHE for electrons is the IQHE for the composite fermions. In Fig. 1-4, we have plotted Eq. (1.5) in the plane of b_{cf} and p. The filled in points are all the observed fraction (with the exception of 5/2) while the the hollow points have not been observed. We should point out that though the electrons are strongly interacting, the composite fermions are non-interacting. The electron-electron correlation is taken care of in Eq. (1.6) by the factor $(\xi_k - \xi_j)^{2p}$. This factor guarantees that the electrons will repulse each other – the probability of finding two electrons near each other decreases as a polynomial of the distance between them.

1.2 Optical Experiments and Collective Modes

IQHE and FQHE are transport phenomena in 2DEG. They manifest themselves in resistance measurements. One way to measure the excitation energy of 2DEG is to measure the activation energies of IQHE and FQHE. The activation energies from the transport measurements measure the energy cost of creating quasi-hole and quasi-electron pairs from the ground state. Thus, the transport experiments measure the excitation energy as the in-plane wave vector q goes to infinity. As the result of momentum conservation, optical experiments, on the other hand, measure the excitation

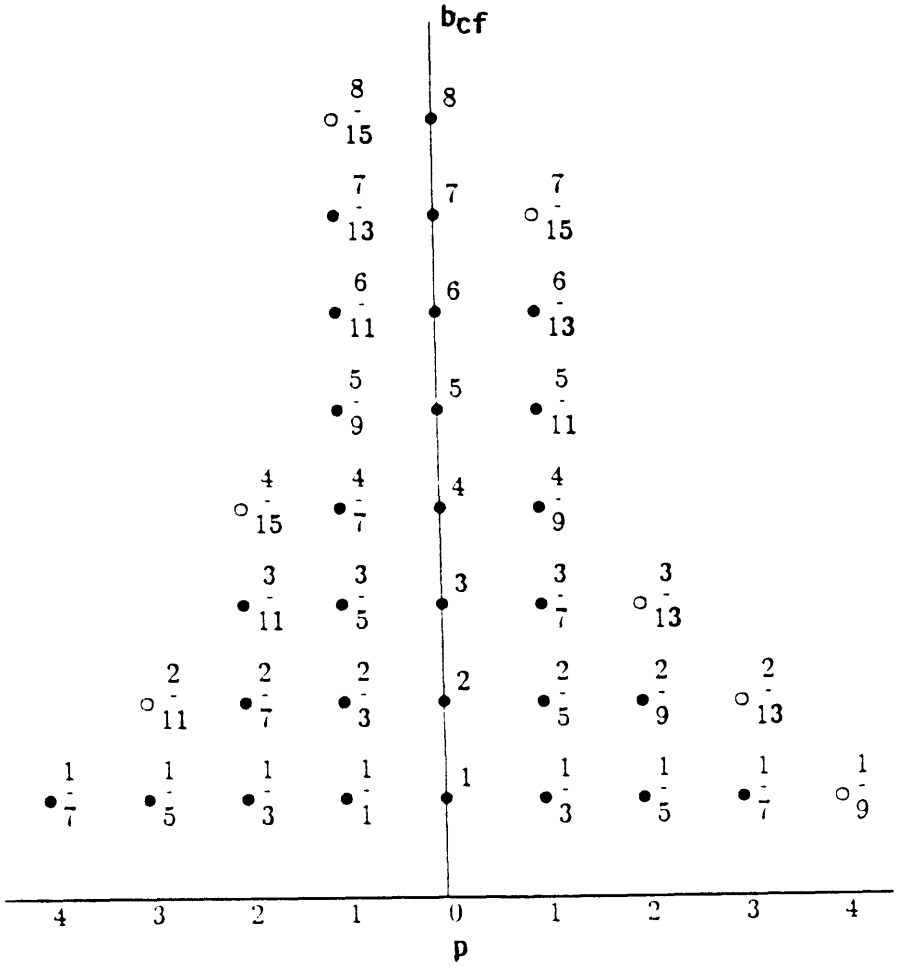

Figure 1-4: Expected fractions in FQHE from the composite fermion theory

energy as $q \rightarrow 0$. In addition to measuring the excitation energies in a completely different region of the momentum space as transport measurements, we can expect optical properties of 2DEG to exhibit interesting anomalies in the IQHE and the FQHE due to the mobility gap or the highly-correlated many-body ground state. In particular, we can expect the 2DEG in magnetic field to be a good laboratory for studying the effect of many-body interaction. By varying the magnetic field, one can change the system continuously from insulating (at exact filling factors) to metallic (at partially filled Landau levels). One might expect to study how the electron screening changes as magnetic field is changed [6]. The spin properties of 2DEG can also be modified as one varies the magnetic field. In particular, at high enough magnetic field, the system will become completely spin polarized. This has tremendous effect on the optical properties through the change in the exchange interaction between electrons [26].

Photoluminescence studies have shown that there are optical anomalies coincident with IQHE and FQHE [6, 8, 13, 35]. These anomalies include intensity minima in the emission intensity at the Landau-level filling factors (ν) of 1 and $\frac{1}{3}$, spectral shifts and peak splittings. Time-resolved [6] measurements showed that an increase in radiative lifetime of the ground state coincided with the the intensity minima. Figure 1-5 shows the data for the photoluminescence anomaly at $\nu = 1$ from Dahl *et. al.*. The upper panel shows the that there is a peak in radiative recombination times (filled in points) coincident with a decrease in photoluminescence intensity at $\nu = 1$. The lower panel of Fig. 1-5 shows the temperature dependence of the radiative recombination time. The peak in recombination time appears to be an activated behavior. The inset of the lower panel shows the similar peak in the radiative recombination time at $\nu = 1$ for a heterojunction. It was suggested that the recombination rate of electron and holes was reduced by the decrease in electron and hole overlap when the 2DEG is in the mobility gap.[6]. The data from Dahl *et. al.* were then explained as a reduction in electron and hole overlap which lead to an increase in life-time and reduction in intensity.

In addition to the photoluminescence studies, there have also been some optical

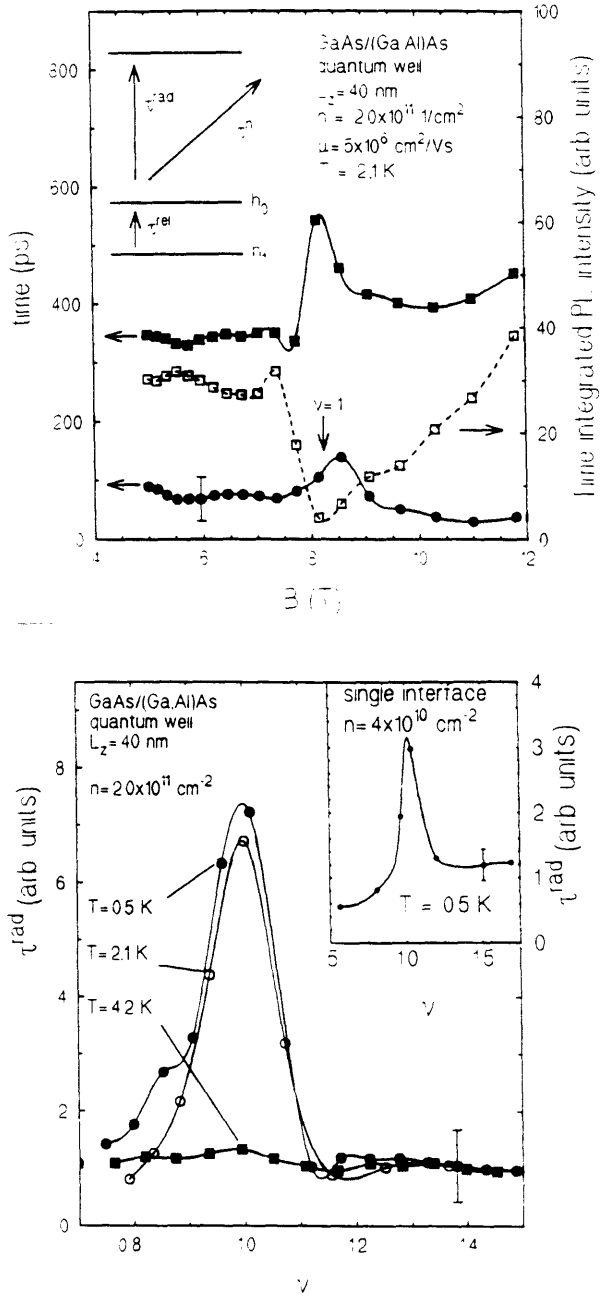

Figure 1-5: Photoluminescence anomaly at $\nu = 1$ after Dahl *et. al.*

absorption and Raman scattering scattering studies of 2DEG which show anomalous behavior at IQHE and FQHE regime. The elementary excitations of the 2DEG at integral filling factors have been the subjects of theoretical [18, 23] and experimental studies [28, 29]. In particular, the inelastic scattering studies of inter-Landau (IL) elementary excitation at integral filling factors of 2 and 1 have shown the importance of exchange and correlation in the IL excitation energy. It was observed that while the IL charge-density excitation must obey Kohn's theorem as the in-plane wave vector q goes to zero, the spin-density excitation need not obey Kohn's theorem and its energy can be significantly different from the charge-density energy. As a result of the spin-polarized ground state at $\nu = 1$, it can be shown that while IL charge- and spin-density excitations are degenerate at $\nu = 2$ as $q \rightarrow 0$, the spin-density excitation has a much higher energy than the charge density excitation energy at $\nu = 1$. It is well known that IL transitions are forbidden to first-order in Raman scattering due to parity considerations. Near integral filling factor, the system is in the localization regime (the plateau region) where the screening is not very effective. This is because the electrons are not allowed to move freely in the mobility gap. This means that the translational symmetry can be broken due to scattering with impurities and remote donors. Therefore, it is possible to observe the density of states of the elementary excitation at integral filling factors. Pinczuk *et. al.* have observed the predicted density of states at integral filling factors [29]. In Fig. 1-6, we have shown the data from Pinczuk *et. al.* [29]. More recently, the intra-Landau level elementary excitation at fractional filling factors has also been observed [27].

In addition to the elementary excitation associated with IL transition, the inter-subband (IS) elementary excitation is often studied. The Raman study of IS transition is usually favored because it is a Raman-active transition. IS transition allows us to study electron-electron interaction by its deviation from expected single particle energy which can be designed by changing the growth parameter. There was much confusion regarding the correct energy of the IS transition [2]. The simplest way to calculate the subband energy levels due to confinement is the self-consistent Hartree approximation. This is basically a mean-field calculation. It is insufficient for opti-

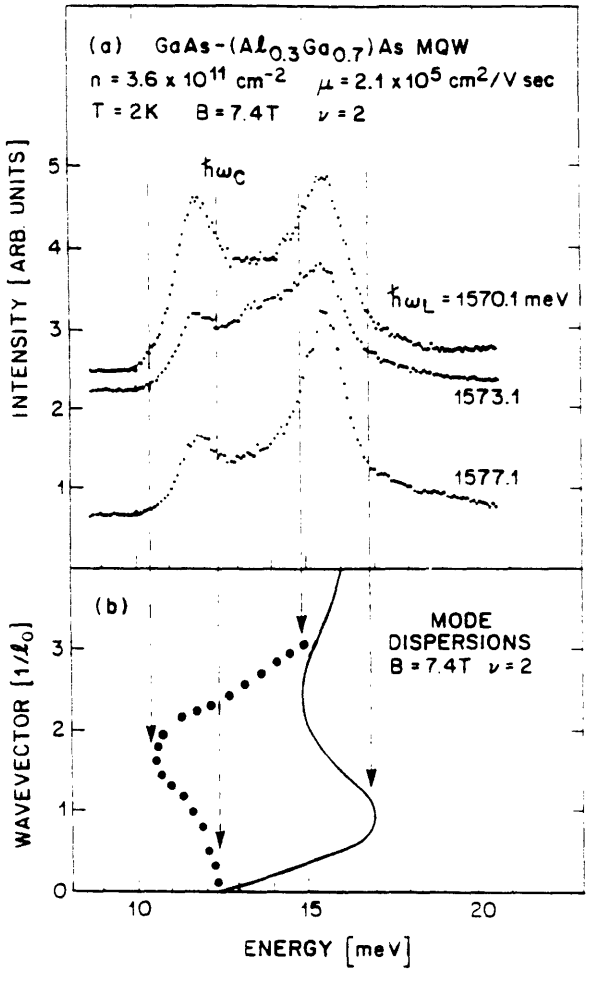

Figure 1-6: Roton density of states at $\nu = 2$ after Pinczuk *et. al.*

cal experiment. The IS optical transition energy is strongly modified by many-body effects. It was found that the largest correction to IS plasmon energy, especially in parabolic quantum wells, is the depolarization shift [22, 28]. The optical IS transition energy also depends on the type of excitation. In contrast with the IL transition at $\nu = 2$, the IS charge- and spin-density excitations are not degenerate as $q \rightarrow 0$. The difference between the IS charge- and the spin- density excitation is just the depolarization shift. (It is also known by other names such as random-phase-approximation and time-dependent Hartree) Experimentally, the IS transition has been observed in remotely-doped single quantum wells and heterojunctions [28], and in remotely-doped parabolic quantum wells using optical absorption [19] and Raman scattering [22].

1.3 Outline of the Thesis

The quantum well structures studied in this thesis are the remotely-doped GaAs/$Al_xGa_{1-x}As$ system. The confinement in the growth direction, referred to here as z, is achieved either by abrupt junctions between the alloys or by grading the alloy. The two types of systems studied here are the single quantum well made from two abrupt junctions of GaAs/$Al_{0.3}Ga_{0.7}As$, and the parabolic quantum well made from graded $Al_xGa_{1-x}As$. The quantum wells are remotely-doped in order to achieve high mobility. The donors are typically set back a few hundred Åfrom the wells where the electrons are confined. For the single quantum well samples, the wells are asymmetrically doped on one side, while the parabolic quantum well is symmetrically doped. These two systems are studied using the technique of resonant Raman scattering. The reason for the use of resonant Raman scattering is that it directly measures the energy dispersion of the elementary excitations. In order to explain the experimental results, I developed a time-dependent Hartree-Fock model for the single quantum wells and a hydrodynamic model for the wide parabolic quantum well. I discuss in Ch. 2 the theoretical formalism developed to handle 2DEG subjected to a tilted magnetic field. In Ch. 3 I discuss the experimental work on single quantum wells and how the experimental results can be interpreted using time-dependent Hartree-Fock formalism developed

in Ch. 2. Finally, in Ch. 4, I present the experimental study of a wide parabolic quantum well. I then discuss how Raman scattering and optical absorption results reveal the importance of going beyond self-consistent Hartree approximation when dealing with the electrons in wide parabolic quantum wells [22]. Finally, I show how the wide parabolic quantum well can be modeled using a hydrodynamics approach.

Chapter 2

Hartree-Fock Formalism in Two Dimensional Systems

In this chapter, the method and models used in calculating the energy levels of single quantum wells in tilted magnetic fields will be discussed. The method used is the time-dependent Hartree-Fock approximation. In the absence of an in-plane component of magnetic field, the Landau levels and subband levels are decoupled: the Landau levels are linearly dependent on magnetic field while the subband levels are independent of magnetic field. With an in-plane magnetic field component, the single-particle states are hybrid states: both sets depend on the magnetic field in complicated ways. The situation is further complicated by the fact that the electron-electron interactions strongly modify the subband wave functions which are now coupled to the Landau levels. We find that in order to achieve numerical agreement between experimental data and theoretical calculation, it is necessary to calculate the wave functions self-consistently and to take into account the finite depth of the well. Before the detailed discussion of the numerical calculation of energy levels, the special case of the parabolic confinement model is considered. The single-particle Hamiltonian of the parabolic confinement model, with an in-plane magnetic field component, is that of the coupled harmonic oscillators. It is diagonalized by the transformations outlined in Eqs. (2.13)-(2.16). In the case of the parabolic confinement model, it is possible to obtain analytical results which are qualitatively correct though not numerically accurate

when compared with experimental data. After setting up the problem in the parabolic confinement potential case, we will to solve the full problem self-consistently. A self-consistent calculation usually starts with a guess of the ground state wave function for the electrons in order to calculate the Hartree potential. Using the approximate Hartree potential, one would then calculate the improved ground state to be used to calculate the Hartree potential for the next iteration. The procedure is repeated until the solution to the Hamiltonian converges. The problem with this scheme is that it can be time consuming and unstable [32]. We solve the self-consistent problem in a different manner. Instead of blindly iterating for a solution, we start with the observation that the Hartree potential must be the solution to the Poisson's Equation. We then define a new variable which is the Hartree potential. Once this transformation is done, the problem is changed from an iterative problem to a non-linear, coupled problem. This would not be a simplification if we want to attempt to solve the problem analytically. Fortunately, the problem is soluble only numerically. In computer computations, a coupled, non-linear approach is no more difficult than an iterative approach.

2.1 Parabolic Confinement Model

One difficulty in calculating the properties of the quasi-two-dimensional system is the derivation of the wave function in the confinement direction. One way to take account of the confinement potential is to model it as a parabolic potential in the z direction. However, care must be taken when attempting to generalize the results to the more general problem of arbitrary confinement potential. The parabolic potential has special properties which are not present in other types of confinement potentials. One example is the energy of the intersubband plasmon. Kohn's theorem which states that in a translationally invariant system, the many-body corrections to the single-particle energy vanish as the in-plane wave vector, $\vec{k}_\perp$, goes to zero. In a parabolic well, the plasmon energy is indeed the single particle energy of the harmonic oscillator as $\vec{k}_\perp \rightarrow 0$. This is not true for arbitrary confinement potential. The reason for using

the parabolic potential is that it allows for analytical results without much effort. It will not give accurate results for the asymmetrically doped single quantum wells that we have studied experimentally. However, we can get a qualitative feel for the effects we expect to find. The parabolic model is especially useful for calculations involving magnetic fields with a component in the plane of the electron gas. In tilted fields, the single particle part of the Hamiltonian with parabolic confinement potential is the Hamiltonian for coupled harmonic oscillators. The solution to the Hamiltonian of coupled harmonic oscillators can be found in many quantum mechanics text books. The ability to calculate the single-particle wave function analytically allows for easy perturbative calculation of the effects of electron-electron interactions. Other types of confinement potentials, on the other hand, do not have analytical solutions for the single-particle part when the magnetic field is tilted with respect to the plane of the electron gas. They require numerical solution.

2.1.1 Transformation of the parabolic Hamiltonian

The Hamiltonian of electrons in magnetic field with confinement potential of $V(z)$ is

$$H = \sum_i \frac{(\vec{p} + \frac{e}{c}\vec{A})_i^2}{2m} + V(z_i) + \frac{1}{2}\sum_{i \neq j} \frac{e^2}{|\vec{r_i} - \vec{r_j}|}. \tag{2.1}$$

In the case of parabolic confinement potential is defined as $V(z) = \frac{m}{2}\Omega^2 z^2$. The vector potential is broken into two parts,

$$\vec{A} = \vec{A}_\perp + \vec{A}_{||}, \tag{2.2}$$

$$\nabla \times \vec{A}_\perp = B_\perp \hat{e}_z, \tag{2.3}$$

and

$$\nabla \times \vec{A}_{||} = B_{||}\hat{e}_x. \tag{2.4}$$

In order to solve Eq. (2.1), a gauge needs to be selected. The gauge to be used is the symmetric gauge

$$\vec{A}_\perp = \frac{B_\perp}{2}(-y, x, 0) \tag{2.5}$$

and

$$\vec{A}_\parallel = B_\parallel(0, -z, 0) \tag{2.6}$$

The single particle part of the Hamiltonian can then be written as

$$H_0 = \frac{1}{2m}(\vec{p}_\perp + \frac{e}{c}\vec{A}_\perp)^2 + \frac{e}{mc}\pi_y A_\parallel + \frac{m}{2}\left[\left(\frac{eB_\parallel}{mc}\right)^2 + \Omega^2\right] z^2 + \frac{p_z^2}{2m}. \tag{2.7}$$

The momentum operators in Eq. (2.7) are

$$\vec{\pi} = \vec{p}_\perp + \frac{e}{c}\vec{A}_\perp \tag{2.8}$$

and

$$\vec{p}_\perp = (p_x, p_y, 0) \tag{2.9}$$

Eq. (2.7) can be written in terms of the ladder operators of harmonic oscillators:

$$H_0 = \hbar\omega_\perp(a^\dagger a + \frac{1}{2}) + \hbar\tilde{\Omega}(d^\dagger d + \frac{1}{2}) + \frac{\hbar\omega_\parallel}{2}\sqrt{\frac{\omega_\perp}{\tilde{\Omega}}}(a - a^\dagger)(d - d^\dagger). \tag{2.10}$$

The various frequencies are defined as: $\omega_\perp = \frac{eB_\perp}{mc}$, $\omega_\parallel = \frac{eB_\parallel}{mc}$, and $\tilde{\Omega} = \sqrt{\Omega^2 + \omega_\parallel^2}$. In Eq. (2.10) a is the lowering ladder operator associated with inter-Landau level transition while d is the lowering ladder operator associated with inter-subband transition. They are defined as

$$a = \sqrt{\frac{c}{2\hbar e B_\perp}}(\pi_x - i\pi_y) \tag{2.11}$$

and

$$d = \frac{p_z}{\sqrt{2m\hbar\tilde{\Omega}}} + i\sqrt{\frac{m\tilde{\Omega}}{2\hbar}}z \tag{2.12}$$

Equation (2.10) is the equation of coupled harmonic oscillator. The coupling term $\frac{\hbar\omega_\parallel}{2}\sqrt{\frac{\omega_\perp}{\tilde{\Omega}}}(a-a^\dagger)(d-d^\dagger)$ is linear in both ladder operators. It can be easily diagonalized by the following transformation:

$$\begin{aligned} a^\dagger &= \frac{\sin\theta}{2}\left(\sqrt{\frac{\omega_\perp}{\Omega_+}}+\sqrt{\frac{\Omega_+}{\omega_\perp}}\right)a_+^\dagger - \frac{\sin\theta}{2}\left(\sqrt{\frac{\omega_\perp}{\Omega_+}}-\sqrt{\frac{\Omega_+}{\omega_\perp}}\right)a_+^\dagger + \frac{\cos\theta}{2}\left(\sqrt{\frac{\omega_\perp}{\Omega_-}}+\sqrt{\frac{\Omega_-}{\omega_\perp}}\right)a_-^\dagger \\ &\quad -\frac{\cos\theta}{2}\left(\sqrt{\frac{\omega_\perp}{\Omega_-}}-\sqrt{\frac{\Omega_-}{\omega_\perp}}\right)a_-, \end{aligned} \tag{2.13}$$

$$\begin{aligned} a &= -\frac{\sin\theta}{2}\left(\sqrt{\frac{\omega_\perp}{\Omega_+}}-\sqrt{\frac{\Omega_+}{\omega_\perp}}\right)a_+^\dagger + \frac{\sin\theta}{2}\left(\sqrt{\frac{\omega_\perp}{\Omega_+}}+\sqrt{\frac{\Omega_+}{\omega_\perp}}\right)a_+^\dagger - \frac{\cos\theta}{2}\left(\sqrt{\frac{\omega_\perp}{\Omega_-}}-\sqrt{\frac{\Omega_-}{\omega_\perp}}\right)a_-^\dagger \\ &\quad +\frac{\cos\theta}{2}\left(\sqrt{\frac{\omega_\perp}{\Omega_-}}+\sqrt{\frac{\Omega_-}{\omega_\perp}}\right)a_-, \end{aligned} \tag{2.14}$$

$$\begin{aligned} d^\dagger &= \frac{\cos\theta}{2}\left(\sqrt{\frac{\tilde{\Omega}}{\Omega_+}}+\sqrt{\frac{\Omega_+}{\tilde{\Omega}}}\right)a_+^\dagger - \frac{\cos\theta}{2}\left(\sqrt{\frac{\tilde{\Omega}}{\Omega_+}}-\sqrt{\frac{\Omega_+}{\tilde{\Omega}}}\right)a_+^\dagger - \frac{\sin\theta}{2}\left(\sqrt{\frac{\tilde{\Omega}}{\Omega_-}}+\sqrt{\frac{\Omega_-}{\tilde{\Omega}}}\right)a_-^\dagger \\ &\quad +\frac{\sin\theta}{2}\left(\sqrt{\frac{\tilde{\Omega}}{\Omega_-}}-\sqrt{\frac{\Omega_-}{\tilde{\Omega}}}\right)a_-, \end{aligned} \tag{2.15}$$

and

$$\begin{aligned} d &= -\frac{\cos\theta}{2}\left(\sqrt{\frac{\tilde{\Omega}}{\Omega_+}}-\sqrt{\frac{\Omega_+}{\tilde{\Omega}}}\right)a_+^\dagger + \frac{\cos\theta}{2}\left(\sqrt{\frac{\tilde{\Omega}}{\Omega_+}}+\sqrt{\frac{\Omega_+}{\tilde{\Omega}}}\right)a_+^\dagger + \frac{\sin\theta}{2}\left(\sqrt{\frac{\tilde{\Omega}}{\Omega_-}}-\sqrt{\frac{\Omega_-}{\tilde{\Omega}}}\right)a_-^\dagger \\ &\quad -\frac{\sin\theta}{2}\left(\sqrt{\frac{\tilde{\Omega}}{\Omega_-}}+\sqrt{\frac{\Omega_-}{\tilde{\Omega}}}\right)a_-. \end{aligned} \tag{2.16}$$

The variables used in the transformation from d and a to a_- and a_+ in Eqs. (2.13)-(2.16)are defined as

$$\tan(2\theta) = -\frac{2\omega_\parallel\omega_\perp}{\tilde{\Omega}^2-\omega_\perp^2} \tag{2.17}$$

$$\text{and}\Omega_\pm = \sqrt{\frac{\omega_\perp^2+\tilde{\Omega}^2}{2}\pm\sqrt{\left(\frac{\omega_\perp^2-\tilde{\Omega}^2}{2}\right)^2+\omega_\perp^2\omega_\parallel^2}}. \tag{2.18}$$

In addition to the operators a_- and a_+, there is a third ladder operator in the symmetric gauge. It is defined as

$$b = \frac{1}{\sqrt{2}}\left(\frac{\zeta}{2\ell_o} + 2\ell_o\frac{\partial}{\partial\zeta^*}\right). \tag{2.19}$$

In Eq. (2.19) the coordinate variable is defined as $\zeta = x + iy$ and magnetic length as $\ell_o = \sqrt{\frac{\hbar c}{eB_\perp}}$. The operator b is the intra-Landau level ladder operator which causes the hopping of electrons from one orbital center to another within a Landau level. It is important to note that because b commutes with both a and d, it also commutes with a_- and a_+. The single-particle Hamiltonian, Eq. (2.10), can now be written in the diagonal representatio:

$$H_0 = \sum_i \hbar\Omega_+(a^\dagger_{+_i}a_{+_i} + \frac{1}{2}) + \hbar\Omega_-(a^\dagger_{-_i}a_{-_i} + \frac{1}{2}). \tag{2.20}$$

From Eq. (2.20), each state is now label by the eigen-values of the number operators $a^\dagger_{+_i}a_{+_i}$ and $a^\dagger_{-_i}a_{-_i}$. The energy for the state with the eigen values of $n_{+_i}, n_{-_i}, n_{b_i}$ are $\sum_i(n_{+_i} + \frac{1}{2})\hbar\Omega_+ + (n_{-_i} + \frac{1}{2})\hbar\Omega-$. The electrons can now make transition between states separated by either $\hbar\Omega_+$ or $\hbar\Omega_-$. The transition between various n_{b_i} states has no effect in the energy of the electron. For a filled orbital level, the b and $b^\dagger$ operator will merely rearrange the electrons. The states separated by $\hbar\Omega_-$ are the lower hybrid (LH) states, while the states separated by $\hbar\Omega_+$ are the upper hybrid (UH) states. In the case of the square well samples we studied experimentally, the cyclotron energy is always less than the intersubband energy for the accessible magnetic fields. In this case, the LH states are Landau-like, while the UH states are subband like.

To calculate the correction to the single particle energy due to electron-electron interaction, it is simpler to work in the Fourier representation

$$V_{e-e}(\vec{r_i}, \vec{r_j}) = \frac{1}{2}\sum_{i\neq j}\int \frac{4\pi e^2}{k^2}e^{i\vec{k}\cdot(\vec{r_i}-\vec{r_j})}\frac{d^3k}{(2\pi)^3}. \tag{2.21}$$

The task is to account for Eq. (2.21) perturbatively. This amounts to evaluating the factor $e^{i\vec{k}\cdot(\vec{r_i}-\vec{r_j})}$ between appropriate many-body wave functions for states corre-

sponding to experimentally observed excitations.

2.1.2 Many-Body Wave Functions

The calculation of the expectation value of Eq. (2.21), requires the construction of many-body wave functions. To make the problem simple, only cases where the lowest orbital level is fully occupied will be studied. This corresponds to $\nu = 2$ if both spin states are occupied and $\nu = 1$ when only the spin states with spin parallel to the magnetic field are occupied. The excited-state wave functions can be constructed from the single-particle wave functions of Eq. (2.20). The ground-state wave function should be totally antisymmetric with respect to the exchange of two particles. This state is labeled Ψ_g. The excited states are states with one electron excited to the next LH or UH state. The cases to be considered are where the excited states are connected to the ground state either by charge density operator or spin density operators. The excited state (not normalized) is then

$$|\Psi_{n\pm}\rangle = \mathcal{C} \sum_i |n_\pm, n_\mp = 0, s\rangle_{i\ i}\langle n_+ = 0, n_- = 0, s|\eta_i B_i(k_\perp)|\Psi_g\rangle. \tag{2.22}$$

In Eq. (2.22), the intra-level operator is defined as

$$B(k_\perp) = e^{i\frac{k_\perp^* \ell_0 b}{\sqrt{2}}} e^{i\frac{k_\perp \ell_0 b^\dagger}{\sqrt{2}}}. \tag{2.23}$$

If the state under consideration is the charge-density excitation, then $\eta_i = 1$. On the other hand if one is interested in the spin-density excitation, then $\eta_i = s_+, s_-$ or s_ξ, where ξ refers to the direction of the magnetic field. For $\nu = 2$ the excitations are split into singlet and triplet states. The singlet state involves the charge density operator and the triplet states involve spin operators. For $\nu = 1$, $\eta_i = s_+$ is not allowed because of the spin polarized ground state. The constant factor $\mathcal{C}$ is the normalization constant such that $\left\langle \Psi_{n\pm} | \Psi_{n\pm} \right\rangle = 1$. To save repeated writings of Eq. (2.22), excitation operators which create the excited states from the ground state can

be defined as

$$\rho_\sigma = \sum_i |n_\sigma, n_{-\sigma} = 0, s\rangle_{i\ i}\langle n_+ = 0, n_- = 0, s|\eta_i B_i(k_\perp). \tag{2.24}$$

In Eq. (2.24), σ is either + or − and $-\sigma$ is − or +. The next step is to evaluate the expectation value of Eq. (2.1) between the wave function defined in Eq. (2.22):

$$\langle \Psi_{\sigma'}|H|\Psi_\sigma\rangle = \mathcal{C}^*\mathcal{C}\langle \Psi_g|\rho^\dagger_{\sigma'} H \rho_\sigma|\Psi_g\rangle. \tag{2.25}$$

After some algebraic manipulation, the expectation value of the Hamiltonian is

$$\langle \Psi_{\sigma'}|H|\Psi_\sigma\rangle = (E_g + n_\sigma\hbar\Omega_\sigma)\delta_{\sigma,\sigma'} + \mathcal{C}^*\mathcal{C}\langle \Psi_g|\rho^\dagger_{\sigma'}\left[V_{e-e}(\vec{r_i},\vec{r_j}),\rho_\sigma\right]|\Psi_g\rangle. \tag{2.26}$$

In Eq. (2.26), E_g is the ground-state energy of the electrons. It is just a constant offset and can be ignored. The single-particle energy cost of exciting a particle into the state n_σ is $n_\sigma\hbar\Omega_\sigma$. The last term involving the commutation of operators is the correction to the single-particle energy from electron-electron interaction.

2.1.3 Excitation Energy

The cases to be considered are : charge- and spin-density excitation at $\nu = 2$ and $\nu = 1$. The evaluation of the correction to the single-particle energy is carried in appendix A. The collective excitation energy is $E_{c\eta}(\sigma',\sigma) = n_\sigma\hbar\Omega_\sigma\delta_{\sigma',\sigma} + E_\eta(\sigma',\sigma)$. For charge-density excitation ($\eta = \rho$) at both $\nu = 1$ and $\nu = 2$, $E_\rho(\sigma',\sigma)$ is

$$\begin{aligned}
E_\rho(\sigma',\sigma) \;=\; & 2N\int \frac{dq_z}{k_\perp^2+q_z^2} e^{-\frac{|k_\perp|^2}{2}} F(n_{\sigma'}, n_{-\sigma'} = 0,0,0 : \vec{k_\perp} - \vec{q_z}) \\
& F(0,0; n_\sigma, n_{-\sigma} = 0 : -(\vec{k_\perp} - \vec{q_z})) + \\
& 2N\int \frac{dq_z}{q_z^2}\Big\{F(n_{\sigma'}, n_{-\sigma'} = 0, n_\sigma, n_{-\sigma} = 0 : \vec{q_z})F(0,0,0,0 : -\vec{q_z}) - \\
& \delta_{\sigma,\sigma'}|F(0,0,0,0 : \vec{q_z})|^2\Big\} - \\
& \int \frac{d^3q}{(2\pi)^3}\frac{4\pi}{q^2}\; e^{-\frac{|q_\perp|^2}{2}}\Big(F(n_{\sigma'}, n_{-\sigma'} = 0,0,0 : -\vec{q})F(0,0; n_\sigma, n_{-\sigma} = 0 : \vec{q}) +
\end{aligned}$$

$$e^{-\frac{k_\perp q_\perp^* - k_\perp^* q_\perp}{2}} F(n_{\sigma'}, n_{-\sigma'} = 0, n_\sigma, n_{-\sigma} = 0 : \vec{q}) F(0,0,0,0 : -\vec{q}) -$$
$$\delta_{\sigma,\sigma'} |F(0,0,0,0 : \vec{q})|^2 \Big) . \tag{2.27}$$

In Eq. (2.27), the wave vectors are written in the unit of of $\frac{1}{\ell_o}$ and the energy is written in the unit of $\frac{e^2}{\epsilon \ell_o}$. The surface particle density N, written in terms of $\frac{1}{\ell_o}$ is $\frac{\nu}{2\pi}$. For spin-density excitations at $\nu = 2$, only the case of s_ξ needs to be considered. The cases of s_+ and s_- are simply separated from s_ξ by the Zeeman energy. $E_s(\sigma', \sigma)$ for the spin-density excitation in this case is the same as the charge-density except the RPA term does not contribute:

$$\begin{aligned} E_s(\sigma', \sigma) \;=\; & \frac{\nu}{\pi} \int \frac{dq_z}{q_z^2} \Big(F(n_{\sigma'}, n_{-\sigma'} = 0, n_\sigma, n_{-\sigma} = 0 : \vec{q_z}) F(0,0,0,0 : -\vec{q_z}) - \\ & \delta_{\sigma,\sigma'} |F(0,0,0,0 : \vec{q_z})|^2 \Big) - \\ & \int \frac{d^3q}{(2\pi)^3} \frac{4\pi}{q^2} \; e^{-\frac{|q_\perp|^2}{2}} \Big(F(n_{\sigma'}, n_{-\sigma'} = 0, 0, 0 : -\vec{q}) F(0,0; n_\sigma, n_{-\sigma} = 0 : \vec{q}) + \\ & e^{-\frac{k_\perp q_\perp^* - k_\perp^* q_\perp}{2}} F(n_{\sigma'}, n_{-\sigma'} = 0, n_\sigma, n_{-\sigma} = 0 : \vec{q}) F(0,0,0,0 : -\vec{q}) - \\ & \delta_{\sigma,\sigma'} |F(0,0,0,0 : \vec{q})|^2 \Big) . \end{aligned} \tag{2.28}$$

At $\nu = 1$, the spin-density excitation with $\eta = s_\xi$ has the same energy as the charge-density excitation energy. The excitation with $\eta = s_+$ is not allowed because the ground state is spin polarized parallel to the magnetic field. The other possible excitation is the spin flip associated with s_-. $E_{flip}(\sigma', \sigma)$ is

$$\begin{aligned} E_{flip}(\sigma', \sigma) \;=\; & \frac{\nu}{\pi} \int \frac{dq_z}{q_z^2} \Big(F(n_{\sigma'}, n_{-\sigma'} = 0, n_\sigma, n_{-\sigma} = 0 : \vec{q_z}) F(0,0,0,0 : -\vec{q_z}) - \\ & \delta_{\sigma,\sigma'} |F(0,0,0,0 : \vec{q_z})|^2 \Big) - \\ & \int \frac{d^3q}{(2\pi)^3} \frac{4\pi}{q^2} \; e^{-\frac{|q_\perp|^2}{2}} \Big\{ F(n_{\sigma'}, n_{-\sigma'} = 0, n_\sigma, n_{-\sigma} = 0 : \vec{q}) F(0,0,0,0 : -\vec{q}) \\ & e^{-\frac{k_\perp q_\perp^* - k_\perp^* q_\perp}{2}} - \delta_{\sigma,\sigma'} |F(0,0,0,0 : \vec{q})|^2 \Big\} . \end{aligned} \tag{2.29}$$

The problem is now reduced to the evaluation of $F(n_+, n_-; m_+, m_- : \vec{k_\perp})$ which is defined as

$$F(n_+, n_-; m_+, m_- : \vec{k_\perp}) = \langle n_+, n_-| \ e^{ik_z z} A(k_\perp) |m_+, m_-\rangle. \tag{2.30}$$

In the case of parabolic confinement potential, $F(n_+, n_-; m_+, m_- : \vec{k_\perp})$ can be written in terms of the ladder operators for the UH and LH states as

$$\langle n_+, n_-| \ e^{ik_z z} A(k_\perp) |m_+, m_-\rangle = \Gamma \langle n_+, n_-| \ e^{\gamma_+ a_+^\dagger} \ e^{\gamma_- a_-^\dagger} \ e^{-\gamma_+^* a_+} \ e^{-\gamma_-^* a_-} |m_+, m_-\rangle. \tag{2.31}$$

The various parameters are defined as

$$\begin{aligned} \Gamma(\vec{k}) \ = \ & exp\left[\frac{\ell_o^2}{4}(kx^2 + ky^2) - \frac{\ell_o^2}{4} ky^2 (sin^2(\theta)\frac{\Omega_+}{\omega_\perp} + cos^2(\theta)\frac{\Omega_-}{\omega_\perp}) \right. \\ & \left. - \frac{\hbar}{4m\Omega_-}(k_x cos(\theta) - k_z sin(\theta))^2 - \frac{\hbar}{4m\Omega_+}(k_x sin(\theta) + k_z cos(\theta))^2 \right], \end{aligned} \tag{2.32}$$

$$\gamma_+(\vec{k}) \ = \ k_z cos(\theta)\sqrt{\frac{\hbar}{2m\Omega_+}} + \frac{\ell_o sin(\theta)}{\sqrt{2}}\left(k_x\sqrt{\frac{\omega_\perp}{\Omega_+}} - ik_y\sqrt{\frac{\omega_\perp}{\Omega_+}}\right), \tag{2.33}$$

and

$$\gamma_-(\vec{k}) \ = \ -k_z sin(\theta)\sqrt{\frac{\hbar}{2m\Omega_-}} + \frac{\ell_o cos(\theta)}{\sqrt{2}}\left(k_x\sqrt{\frac{\omega_\perp}{\Omega_-}} - ik_y\sqrt{\frac{\omega_\perp}{\Omega_-}}\right). \tag{2.34}$$

In appendix B, a derivation of the analytic expression for $F(n_+, n_-; m_+, m_- : \vec{k}_\perp)$ in the case of parabolic confinement potential is presented. The trick is to transform from the eigen-states of the number operators $|n_\pm\rangle$ to the semi-classical states. The evaluation of $F(n_+, n_-; m_+, m_- : \vec{k_\perp})$ is then reduced to simple integration. The final analytic form of $F(n_+, n_-; m_+, m_- : \vec{k_\perp})$ is

$$\begin{aligned} F(n_+, n_-; m_+, m_- : \vec{k}) = & \frac{\Gamma \gamma_+^{n_+} \gamma_-^{n_-} (-\gamma_+^*)^{m_+} (-\gamma_-^*)^{m_-}}{\sqrt{m_+! m_-! n_+! n_-!}} \sum_j^{min(m_+,n_+)} \sum_l^{min(m_-,n_-)} \\ & (-|\gamma_+|^2)^{-j} (-|\gamma_-|^2)^{-l} \frac{m_+! m_-! n_+! n_-!}{(n_+ - j)!(m_+ - j)! j! (n_- - l)!(m_- - l)! l!}. \end{aligned} \tag{2.35}$$

Table 2.1: Parameters Used in Parabolic Model Calculations

	sample A		sample B	
	$\nu = 1$	$\nu = 2$	$\nu = 1$	$\nu = 2$
Ω	27 meV			
Magnetic Field	10 T	5 T	14.4 T	7.2 T
$\omega_\perp$	17.3 meV	8.64 meV	12.44 meV	24.9 meV
$\frac{e^2}{\epsilon \ell_o}$	13.8 meV	9.73 meV	16.5 meV	11.67 meV

2.1.4 Application to $\Delta n_\sigma = 1$

We now specialize to the situation closest to the experimental condition: one electron is excited from the ground state to the excited state. The excited state can be either UH or LH state. In this situation, we need to diagonalize a 2×2 Hamiltonian matrix. The Hamiltonian matrix elements will be the form $H(\sigma, \sigma') = \hbar\Omega_\sigma \delta_{\sigma,\sigma'} + E_\eta(\sigma, \sigma')$. In the case where the UH energy is much greater than the LH energy (as is the case for our experimental set up), we expect the coupling terms $E_\eta(+,-)$ and $E_\eta(-,+)$ to be small.

Charge-density excitation

The charge-density energy has the same form for both $\nu = 2$ and $\nu = 1$. The charge-density energy matrix element for UH transition is

$$\begin{aligned} E_\rho(+,+) &= \frac{\nu}{\pi}\int \frac{dq_z}{k_\perp^2+q_z^2} e^{-\frac{|k_\perp|^2}{2}} \left|F(1,0;0,0:\vec{k_\perp}-\vec{q_z})\right|^2 - \\ &\quad \frac{\nu}{\pi}\int \frac{dq_z}{q_z^2}\left\{F(1,0;1,0:\vec{q_z})F(0,0,0,0:-\vec{q_z}) - |F(0,0,0,0:\vec{q_z})|^2\right\} - \\ &\quad \int \frac{d^3q}{(2\pi)^3}\frac{4\pi}{q^2}\ e^{-\frac{|q_\perp|^2}{2}}\left(F(1,0;0,0:-\vec{q})F(0,0;1,0:\vec{q}) - |F(0,0,0,0:\vec{q})|^2 + \right. \\ &\quad \left. e^{-\frac{k_\perp q_\perp^* - k_\perp^* q_\perp}{2}} F(1,0;1,0:\vec{q})F(0,0,0,0:-\vec{q})\right), \end{aligned} \tag{2.36}$$

where the indices are arranged in the order of $F(n_+, n_-; m_+, m_-)$. The use of Eq. (2.35) results in

$$E_\rho(+,+) = \frac{\nu}{\pi}\int \frac{dq_z}{k_\perp^2+q_z^2} e^{-\frac{|k_\perp|^2}{2}} |\Gamma(\vec{k}_\perp - q_z))|^2 |\gamma_+(\vec{k}_\perp - q_z)|^2 -$$

$$\frac{\nu}{\pi}\int\frac{dq_z}{q_z^2}|\Gamma(q_z)|^2|\gamma_+(q_z)|^2 -$$
$$\int\frac{d^3q}{(2\pi)^3}\frac{4\pi}{q^2}\ e^{-\frac{|q_\perp|^2}{2}}|\Gamma(\vec{q}|^2\left(1-|\gamma_+(\vec{q})|^2\right)$$
$$\left(e^{-\frac{k_\perp q_\perp^* - k_\perp^* q_\perp}{2}}-1\right), \tag{2.37}$$

$$\begin{aligned}E_\rho(-,-) &= \frac{\nu}{\pi}\int\frac{dq_z}{k_\perp^2+q_z^2}e^{-\frac{|k_\perp|^2}{2}}|\Gamma(\vec{k}_\perp-q_z))|^2|\gamma_-(\vec{k}_\perp-q_z)|^2 - \\ &\frac{\nu}{\pi}\int\frac{dq_z}{q_z^2}|\Gamma(q_z)|^2|\gamma_-(q_z)|^2 - \\ &\int\frac{d^3q}{(2\pi)^3}\frac{4\pi}{q^2}\ e^{-\frac{|q_\perp|^2}{2}}|\Gamma(\vec{q}|^2\left(1-|\gamma_-(\vec{q})|^2\right)\left(e^{-\frac{k_\perp q_\perp^* - k_\perp^* q_\perp}{2}}-1\right)\end{aligned} \tag{2.38}$$

and

$$\begin{aligned}E_\rho(+,-) &= \frac{\nu}{\pi}\int\frac{dq_z}{k_\perp^2+q_z^2}e^{-\frac{|k_\perp|^2}{2}}|\Gamma(\vec{k}_\perp-q_z))|^2\gamma_+(\vec{k}_\perp-q_z)\gamma_-^*(\vec{k}_\perp-q_z) - \\ &\frac{\nu}{\pi}\int\frac{dq_z}{q_z^2}|\Gamma(q_z)|^2\gamma_+(q_z)\gamma_-^*(q_z) - \\ &\int\frac{d^3q}{(2\pi)^3}\frac{4\pi}{q^2}\ e^{-\frac{|q_\perp|^2}{2}}|\Gamma(\vec{q}|^2\gamma_+(\vec{q})\gamma_-^*(\vec{q})\left(1-e^{-\frac{k_\perp q_\perp^* - k_\perp^* q_\perp}{2}}\right).\end{aligned} \tag{2.39}$$

$E_\rho(-,+)$ is simply the complex conjugate of $E_\rho(+,-)$. In the limit $\vec{k}\to 0$, Eqs. (2.37), (2.38), and (2.39) all evaluate to zero. This is the result of Kohn's theorem [20] which states that in a translationally invariant system, the energy of the charge-density excitation energy approaches the single-particle energy as $\vec{k}\to 0$. Since the Hamiltonian with parabolic confinement potential is that for coupled harmonic oscillators, both UH and LH satisfy Kohn's theorem. In agreement with reference [4], we see from Eqs. (2.37), (2.38), and (2.39) that the Hartree energy is exactly cancelled by the RPA correction while the exchange self-energy is exactly cancelled by the local field correction. This is demonstrated in Figs. 2-1 and 2-4 for the case with zero tilt angle: the charge density (singlet at $\nu=2$) excitations associated with both IL and IS transitions have the single particle energy as $k_\perp\to 0$. In Fig. 2-1 and 2-4, the IS single particle transition energy is $27meV$ and cyclotron energy is $8.64meV$ at $\nu=2$

and $17.3meV$ at $\nu = 1$.

Spin-density and spin-flip excitations

At $\nu = 2$, the spin-density excitation energy is the charge-density excitation energy minus the RPA term. The spin-density energy matrix elements are:

$$E_s(+,+) = -\frac{\nu}{\pi}\int \frac{dq_z}{q_z^2}|\Gamma(q_z)|^2|\gamma_+(q_z)|^2 - \int \frac{d^3q}{(2\pi)^3}\frac{4\pi}{q^2}\; e^{-\frac{|q_\perp|^2}{2}}|\Gamma(\vec{q})|^2\left(1-|\gamma_+(\vec{q})|^2\right)\left(e^{-\frac{k_\perp q_\perp^* - k_\perp^* q_\perp}{2}}-1\right) \quad (2.40)$$

$$E_s(-,-) = -\frac{\nu}{\pi}\int \frac{dq_z}{q_z^2}|\Gamma(q_z)|^2|\gamma_-(q_z)|^2 - \int \frac{d^3q}{(2\pi)^3}\frac{4\pi}{q^2}\; e^{-\frac{|q_\perp|^2}{2}}|\Gamma(\vec{q})|^2\left(1-|\gamma_-(\vec{q})|^2\right)\left(e^{-\frac{k_\perp q_\perp^* - k_\perp^* q_\perp}{2}}-1\right) \quad (2.41)$$

and

$$E_s(+,-) = -\frac{\nu}{\pi}\int \frac{dq_z}{q_z^2}|\Gamma(q_z)|^2\gamma_+(q_z)\gamma_-^*(q_z) - \int \frac{d^3q}{(2\pi)^3}\frac{4\pi}{q^2}\; e^{-\frac{|q_\perp|^2}{2}}|\Gamma(\vec{q})|^2\gamma_+(\vec{q})\gamma_-^*(\vec{q})\left(1-e^{-\frac{k_\perp q_\perp^* - k_\perp^* q_\perp}{2}}\right). \quad (2.42)$$

Figure 2-4 shows the dispersion for the singlet and triplet excitations when the magnetic field is perpendicular to the 2DEG plane. The spin-density excitation is degenerate with the charge-density excitation for IL transition, but not for the IS transition. The reason for this is that the RPA term is zero at $k_\perp = 0$ for the IL transition but not the IS transition. The energy gap between the charge- and spin-density excitations is a measure of the strength of RPA. The energy gap for the IS transition is present for arbitrary confinement potential, but its value is dependent on the type of confinement potential. Figures 2-2 and 2-3 show the dependence of the charge-density (singlet) energy and spin-density (triplet) energy on the tilt angle at the in-plane wave vector value of $k_\perp \ell_o = 0.05$ and $k_\perp \ell_o = 0.04$. The parameters used to calculate the curves are listed in table 2.1. The dependence on the angle of $\vec{k}_\perp$ has been averaged out.

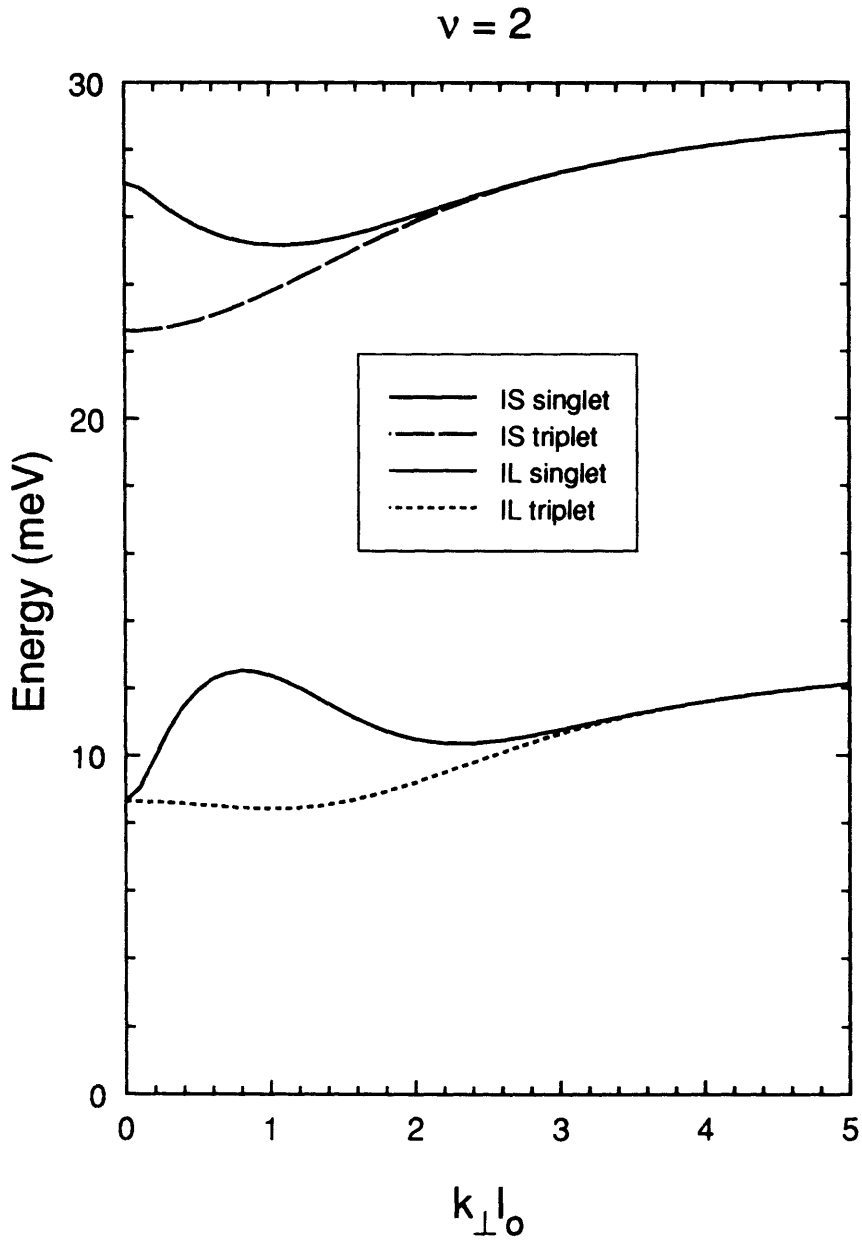

Figure 2-1: The dispersion of the singlet and triplet excitations. The effective mass is 0.067 times the bare electron mass. The IS transition energy at zero tilt angle is taken to be $27meV$ The curves are calculated with $\nu = 2$ and $B_\perp = 5T$.

The reason is that in the experiments, we did not have precise control of the angle between the incident wave vector and the in-plane component of the magnetic field. This is not a severe problem because at the very small in-pane wave vector of interest, the variation of the charge-density energy as a function of the angle is minor. As the tilt angle goes to $\frac{\pi}{2}$, the UH energy goes to infinity while the LH energy goes to zero. This is because the perpendicular magnetic field component is kept at $5T$. As tilt angle approaches $\frac{\pi}{2}$, the total magnetic field is required to increase to infinity in order to keep $B_\perp$ at 5 T. In Fig. 2-2, the experimental data for sample A is also plotted. As can be seen that the experimental points do not agree with the calculated curves. This is as expected since sample A is an asymmetrically doped single quantum well, not a parabolic quantum well. Only after the realistic confinement potential and self-consistent Hartree potential are included will the theoretical curve agree with the experimental data.

At $\nu = 1$ the spin-density excitation energy elements are given by Eqs. (2.37)-(2.39). The spin-flip excitation energy elements are

$$\begin{aligned}
E_{flip}(+,+) &= -\frac{\nu}{\pi}\int \frac{dq_z}{q_z^2}|\Gamma(q_z)|^2|\gamma_+(q_z)|^2 - \\
&\int \frac{d^3q}{(2\pi)^3}\frac{4\pi}{q^2}\; e^{-\frac{|q_\perp|^2}{2}}|\Gamma(\vec{q})|^2\left\{\left(1-|\gamma_+(\vec{q})|^2\right)e^{-\frac{k_\perp q_\perp^* - k_\perp^* q_\perp}{2}} - 1\right\}, \\
E_{flip}(-,-) &= -\frac{\nu}{\pi}\int \frac{dq_z}{q_z^2}|\Gamma(q_z)|^2|\gamma_-(q_z)|^2 - \\
&\int \frac{d^3q}{(2\pi)^3}\frac{4\pi}{q^2}\; e^{-\frac{|q_\perp|^2}{2}}|\Gamma(\vec{q})|^2\left\{\left(1-|\gamma_-(\vec{q})|^2\right)e^{-\frac{k_\perp q_\perp^* - k_\perp^* q_\perp}{2}} - 1\right\},
\end{aligned} \tag{2.43}$$

and

$$\begin{aligned}
E_{flip}(+,-) &= -\frac{\nu}{\pi}\int \frac{dq_z}{q_z^2}|\Gamma(q_z)|^2\gamma_+(q_z)\gamma_-^*(q_z) + \\
&\int \frac{d^3q}{(2\pi)^3}\frac{4\pi}{q^2}\; e^{-\frac{|q_\perp|^2}{2}}|\Gamma(\vec{q})|^2\gamma_+(\vec{q})\gamma_-^*(\vec{q})e^{-\frac{k_\perp q_\perp^* - k_\perp^* q_\perp}{2}}.
\end{aligned} \tag{2.44}$$

It is interesting to note that the spin-flip excitation at $\nu = 1$ can have higher energy than the charge density excitation as $k_\perp \to 0$. This is the case for IL transition in Fig. 2-4. The reason for this is that the local field correction is no longer cancelled by

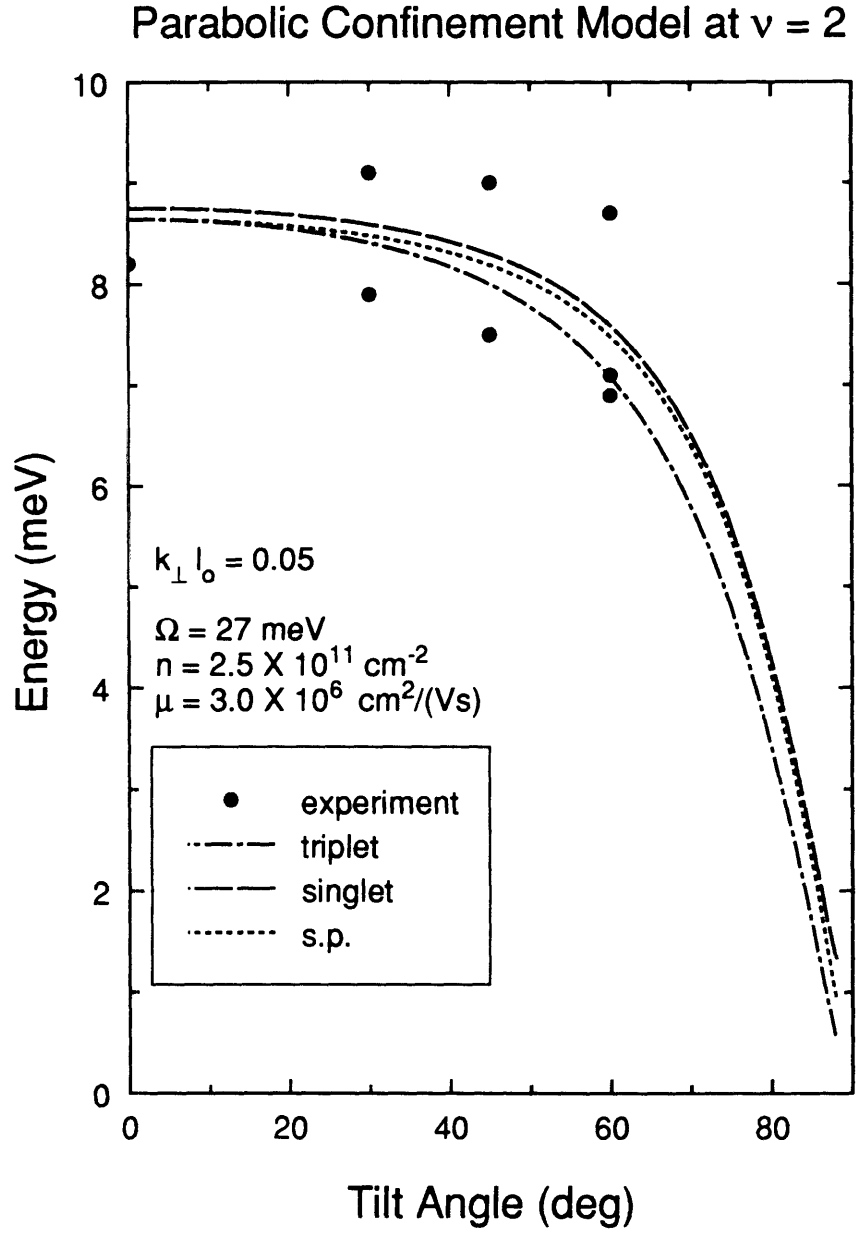

Figure 2-2: The dependence of the singlet and triplet energy as the function of the tilt angle. The in-plane wave vector value is $\frac{0.05}{\ell_o}$. The effective mass is 0.067 times the bare electron mass. The IS transition energy at zero tilt angle is taken to be $27meV$ The curves are calculated with $\nu = 2$ and $B_\perp = 5T$.

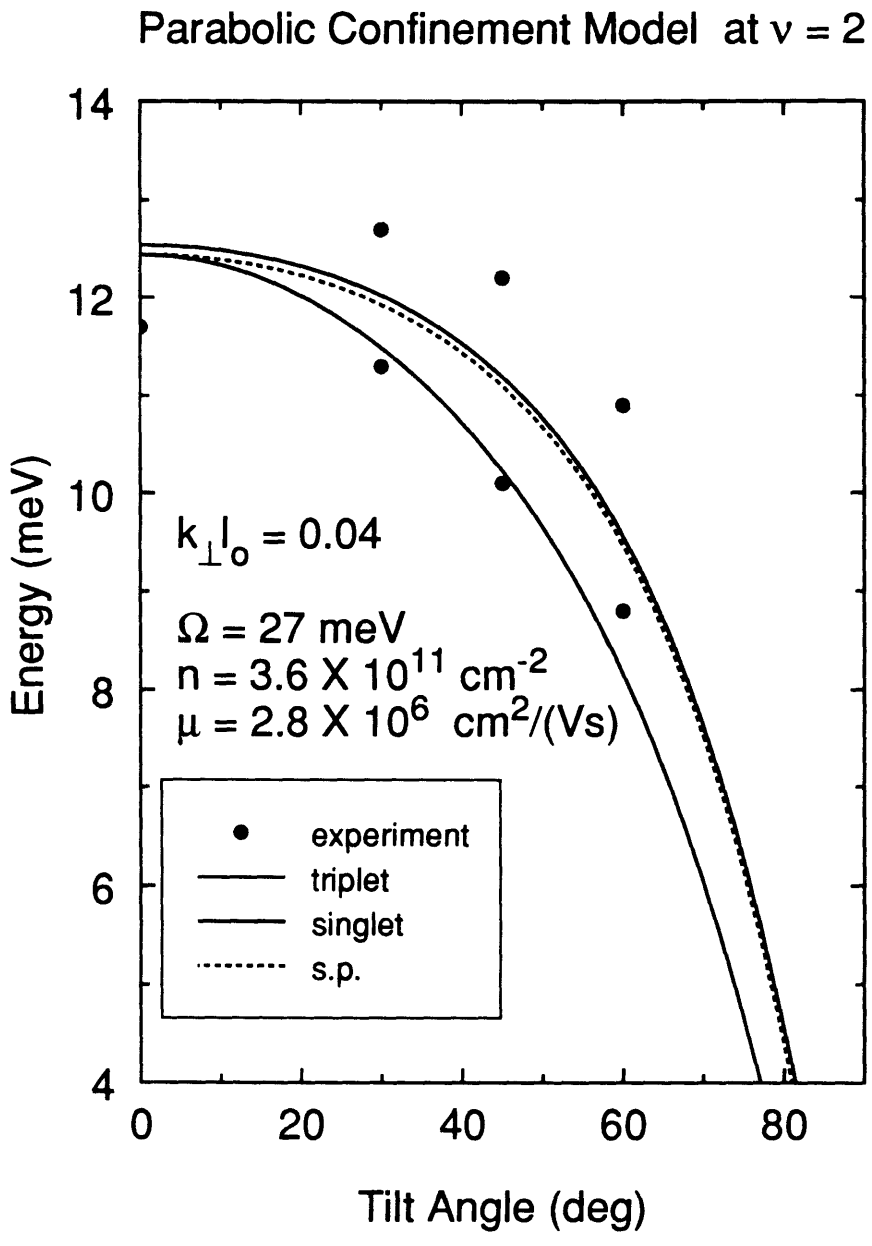

Figure 2-3: The dependence of the singlet and triplet energy as the function of the tilt angle. The in-plane wave vector value is $\frac{0.04}{\ell_o}$. The effective mass is 0.067 times the bare electron mass. The IS transition energy at zero tilt angle is taken to be $27meV$ The curves are calculated with $\nu = 2$ and $B_\perp = 7.2T$.

the exchange self-energy as was the case at $\nu = 2$. The cyclotron energy at $B = 10T$ is $17.3meV$. The charge-density excitation is still at the cyclotron energy while the spin-flip energy is now much greater than the cyclotron energy : it is roughly 21.5 meV.

2.2 Realistic Self-Consistent Calculation

The only way to obtain numerical results of sufficient accuracy is to approach the problem self-consistently and to take account of the shape and height of the well. We calculate the single-particle states by solving for the self-consistent states of the Schroedinger's equations and Poisson's equation. The other approximation terms for the electron-electron interaction would have to be calculated perturbatively. This approach may not be sufficient. The fact that we are taking into account only the Hartree potential in the self-consistent potential means that we are treating it as the dominant effect of the electron-electron interaction. This may not be the case. For example, in the preceding section on parabolic well, Kohn's Theorem guarantees that the Hartree and the RPA terms have exactly the same magnitude, but opposite signs as $q \rightarrow 0$. However, as $q \rightarrow \infty$, the RPA term is actually zero. Thus, in calculating "single particle" energy, it is probably sufficient to include just the Hartree term

2.2.1 Hamiltonian

The Hamiltonian for this system of asymmetrically doped, finite square well is

$$\begin{aligned} H &= \sum_i \frac{(\vec{p} + \frac{e}{c}\vec{A})_i^2}{2m} + V(z_i) + \frac{2\pi N e^2}{\epsilon} z_i \\ &\quad + \frac{1}{2}\sum_{i \neq j} \frac{e^2}{|\vec{r_i} - \vec{r_j}|}, \end{aligned} \tag{2.45}$$

$$V(z_i) = \begin{cases} 0 & |z_i| < \frac{L}{2} \\ V_o & \text{otherwise.} \end{cases}$$

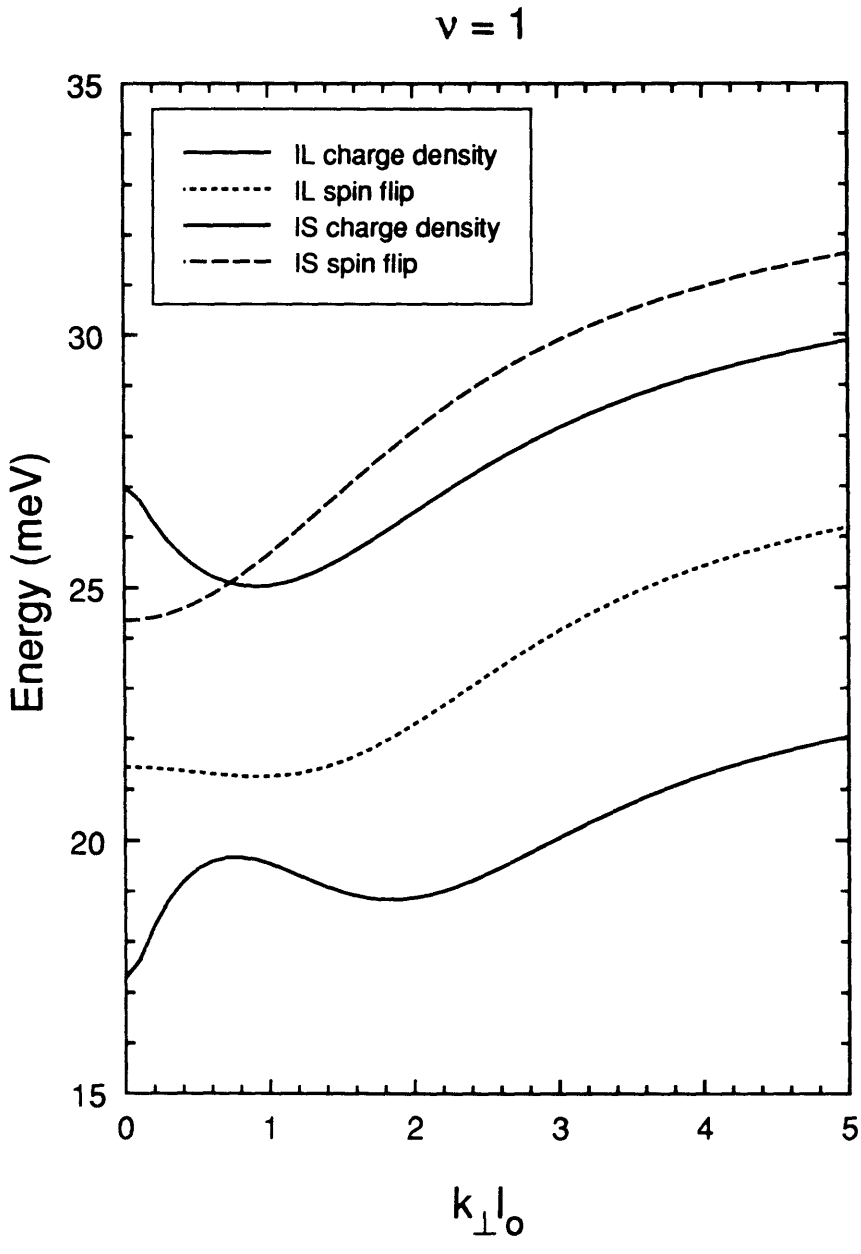

Figure 2-4: The dispersion of the charge density and spin flip excitations. The effective mass is 0.067 times the bare electron mass. The IS transition energy at zero tilt angle is $27meV$. The curves are calculated with $\nu = 1$ and $B_\perp = 10T$.

We defined V_o as the discontinuity at the edges of the well. For the junction made of GaAs/$Al_{0.3}Ga_{0.7}$As, the value of V_o is 225 meV. In Eq. (2.45), the term $2\pi Ne^2 z_i$ is due to the asymmetrically doped doners. In this case, the doners are to the left of the well. We will proceed with the same gauge as we used for the parabolic well with the exception that the parallel component of the vector potential is different from Eq. (2.6). For the numerical computation, it is easier to defined the parallel component as

$$\vec{A}_{||} = B_{||}(z, 0, 0). \tag{2.46}$$

We can now substitute the definition for the ladder operators into Eq. (2.45),

$$\begin{aligned} H &= \sum_i \hbar\omega_\perp (a_i^\dagger a_i + \frac{1}{2}) + \frac{m}{2}\left(\frac{eB_{||}}{mc}\right)^2 z_i^2 + \hbar\left(\frac{eB_{||}}{mc}\right)\sqrt{\frac{m\omega_\perp}{2\hbar}}(a_i + a_i^\dagger) z_i + \\ &\quad \frac{(p_z)_i^2}{2m} + V(z_i) + \frac{2\pi Ne^2}{\epsilon} z_i + \frac{1}{2}\sum_{i\neq j} \frac{e^2}{|\vec{r_i} - \vec{r_j}|}. \end{aligned} \tag{2.47}$$

The Hamiltonian can be separated into an unperturbed part which includes the single particle Hamiltonian and the Hartree potential and a perturbative part which includes the partial Coulomb interaction where the Hartree potential has been subtracted out:

$$\begin{aligned} H_0 &= \sum_i \hbar\omega_\perp (a_i^\dagger a_i + \frac{1}{2}) + \frac{m}{2}\left(\frac{eB_{||}}{mc}\right)^2 z_i^2 + \hbar\left(\frac{eB_{||}}{mc}\right)\sqrt{\frac{m\omega_\perp}{2\hbar}}(a_i + a_i^\dagger) z_i + \\ &\quad \frac{(p_z)_i^2}{2m} + V(z_i) + \frac{2\pi Ne^2}{\epsilon} z_i + V_{Hartree}(z_i) \end{aligned} \tag{2.48}$$

$$H_{e-e} = \frac{1}{2}\sum_{i\neq j} \frac{e^2}{|\vec{r_i} - \vec{r_j}|} - \sum_i V_{Hartree}(z_i). \tag{2.49}$$

The Hartree potential is just the solution to the Poisson's Equation,

$$V_{Hartree}(z) = -\frac{2\pi Ne^2}{\epsilon}\int_{-L/2}^{L/2} \Psi_g^* \Psi_g |x - z| dx. \tag{2.50}$$

The problem is to be solved in two stages. First, the eigenfunctions of the unperturbed Hamiltonian (Eq. (2.48) must be calculated numerically. The effect of the Eq. (2.49) can then be calculated perturbatively using many-body wave functions constructed

from the eigen-functions of Eq. (2.48), similar to the calculation carried out previously for the parabolic confinement model.

2.2.2 Self-Consistent Single-Particle States

The approach to the solution of Eq. (2.48) will be to treat half the problem numerically and half by series expansion. The solution to Eq. (2.48) is assumed to be a series expansion of the eigenstates in Landau-levels. The coefficient of the landau-levels are treated as a function of z:

$$\Psi_g = \sum_{n=0}^{nmax-1} g_n(z)|n\rangle, \tag{2.51}$$

$$\Psi_m = \sum_{n=0}^{nmax-1} f_n^m(z)|n\rangle. \tag{2.52}$$

Then, the differential equations for the coefficients $g_n(z)$ and $f_n^m(z)$ are derived by minimizing the expectation value of Eq. (2.48). Finally, the solution to the differential equations must be solved numerically. In Eqs. (2.51) and (2.52), n represents the Landau-level index, m is the excited state index, and $nmax$ is the number of Landau levels used in the expansion. It is clear that the term $\hbar\left(\frac{eB_\parallel}{mc}\right)\sqrt{\frac{m\omega_\perp}{2\hbar}}(a_i + a_i^\dagger)z_i$ in Eq. (2.48) is the term that causes the mixing of the Landau states: it couples the differential equation for the coefficient of the nth Landau level with $n \pm 1$th Landau levels. Substituting Eqs. (2.51) and (2.52) into the expectation value of Eq. (2.48) and equating the coefficients of the nth Landau-level, the set of coupled second-order differential equation for the coefficient of the Landau levels is

$$\begin{aligned} E_g g_n(\zeta) &= -\frac{\hbar\omega_\perp}{2}\frac{\partial^2 g_n(\zeta)}{\partial\zeta} + \left(\hbar\omega_\perp(n+\frac{1}{2}) + \frac{\hbar\omega_\parallel^2}{\omega_\perp}\zeta^2\right) g_n(\zeta) + \\ &\quad \hbar\omega_\parallel\sqrt{\frac{1}{2}}\zeta(\sqrt{n}\,g_{n-1}(\zeta) + \sqrt{n+1}\,g_{n+1}(\zeta)) + \\ &\quad \left(V(\zeta) + \frac{\nu e^2}{\epsilon\ell_o}\zeta + g_{n_{max}}(\zeta)\right) g_n(\zeta), \end{aligned} \tag{2.53}$$

$$\frac{\partial^2 g_{nmax}(\zeta)}{\partial\zeta^2} = -\frac{4\pi N e^2}{\epsilon}\sum_{i=0}^{nmax-1} g_i(\zeta)g_i(\zeta), \tag{2.54}$$

and

$$E_r f_n^r(\zeta) = -\frac{\hbar\omega_\perp}{2}\frac{\partial^2 f_n^r(\zeta)}{\partial\zeta} + \left(\hbar\omega_\perp(n+\frac{1}{2}) + \frac{\hbar\omega_\parallel^2}{\omega_\perp}\zeta^2\right) f_n^r(\zeta) +$$
$$\hbar\omega_\parallel\sqrt{\frac{1}{2}}\zeta(\sqrt{n}f_{n-1}^r(\zeta) + \sqrt{n+1}f_{n+1}^r(\zeta)) +$$
$$\left(V(\zeta) + \frac{\nu e^2}{\epsilon\ell_o}\zeta + g_{nmax}(\zeta)\right) f_n^r(\zeta). \tag{2.55}$$

The set of $nmax+1$ equations represented by Eqs. (2.53) and (2.54) is the differential equations for the ground state. The set of $nmax$ equations represented by Eq. (2.55) is the differential equations for the excited states. The reason for the extra variable in the set of equations for the ground state is that instead of solving for self-consistent solution iteratively, we have used a transformation mechanism where we introduced a new Hartree variable to eliminate the need for iteration. The solution to Eq. (2.54), up to a constant factor is

$$g_{nmax}(\zeta) = -\frac{2\pi Ne^2}{\epsilon}\int_{\frac{-L}{2}}^{\frac{L}{2}}\sum_{i=0}^{nmax-1}|x-\zeta|\, g_i(x)g_i(x)dx \tag{2.56}$$

Instead of an iterative $nmax$ coupled, second-order differential equations problem, we have transformed the problem into a non-iterative $nmax+1$ problem and avoided the possibility of instability that is often associated with iterative solution. The cost of this transformation is only one extra second-order equation. This is not a big cost considering that we need to use several Landau coefficients for our problem, the cost of one extra variable is negligible. The transformation actually saves computational resources because the iterative procedure usually takes many iterations before converging to a solution.

2.2.3 Correction to the Single-Particle Energy

The expressions from section 2.1.3 for the energy of the charge-density and spin-density excitations are still valid for the single quantum well case. We simply have to remember to subtract out the Hartree contribution and the evaluate $F(n_+, n_-; m_+, m_- : \vec{k_\perp})$ with the new wave functions we solved for in section 2.2.2. We will approach the problem in a less general way than in parabolic confinement potential case. We will

specialize to the situations of our experiments. We will also further simplify the problem by assuming that there is no coupling between the UH and LH transitions. This approximation is valid in our experimental situation since the UH transition is $\sim 25meV$ while the LH transition is $\leq 12meV$. The coupling is strong only when the energy levels are close. If we label the single ground-state wave function as $|g\rangle$, and the single excited-state wave function as $|+\rangle$, then the collective excitation energy can be written as $E(\vec{k}) = E_+ + E(\vec{k},+,+)$ where E_+ is the single-particle energy (including the Hartree energy) and $E(\vec{k},+,+)$ is the correction to the single-particle energy.

The charge density excitation is

$$\begin{aligned} E(\vec{k},+,+) &= \frac{\nu}{\pi}\int \frac{dq_z}{k_\perp^2+q_z^2} e^{-\frac{|k_\perp|^2}{2}} \left|F(+,g:\vec{k_\perp}-\vec{q_z})\right|^2 - \\ &\int \frac{d^3q}{(2\pi)^3}\frac{4\pi}{q^2}\ e^{-\frac{|q_\perp|^2}{2}} \Big(|F(g,+:\vec{q})|^2 - |F(g;g:\vec{q})|^2 + \\ &e^{-\frac{k_\perp q_\perp^* - k_\perp^* q_\perp}{2}} F(+,+:\vec{q})F(g,g:-\vec{q})\Big). \end{aligned} \tag{2.57}$$

The spin density at $\nu = 2$ is

$$\begin{aligned} E(\vec{k},+,+) &= -\int \frac{d^3q}{(2\pi)^3}\frac{4\pi}{q^2}\ e^{-\frac{|q_\perp|^2}{2}} \Big(|F(g,+:\vec{q})|^2 - |F(g;g:\vec{q})|^2 + \\ &e^{-\frac{k_\perp q_\perp^* - k_\perp^* q_\perp}{2}} F(+,+:\vec{q})F(g,g:-\vec{q})\Big). \end{aligned} \tag{2.58}$$

At $\nu = 1$, the spin flip excitation becomes,

$$\begin{aligned} E(\vec{k},+,+) &= \int \frac{d^3q}{(2\pi)^3}\frac{4\pi}{q^2}\ e^{-\frac{|q_\perp|^2}{2}} \Big\{ |F(g;g:\vec{q})|^2 - \\ &e^{-\frac{k_\perp q_\perp^* - k_\perp^* q_\perp}{2}} F(+,+:\vec{q})F(g,g:-\vec{q})\Big\}. \end{aligned} \tag{2.59}$$

In Eqs. (2.57), (2.58), and (2.59), $F(\sigma,\sigma':\vec{k})$ is defined as,

$$F(\sigma,\sigma':\vec{k}) = \langle\sigma|\ e^{ik_z z} A(k_\perp)|\sigma'\rangle \tag{2.60}$$

There are three types terms we need to evaluate: $F(g,+:\vec{q})$ $F(+,+:\vec{q})$ and $F(g,g:\vec{q})$. We can substitute Eqs. (2.51) and (2.52) into the definitions for $F(\sigma,\sigma',vecq)$:

$$\begin{aligned} F(+,+:\vec{q}) &= \sum_i \sum_j \int e^{iq_z z} f_i(z) f_j(z) dz \langle i|A(q_\perp)|j\rangle \\ F(g,+:\vec{q}) &= \sum_i \sum_j \int e^{iq_z z} g_i(z) f_j(z) dz \langle i|A(q_\perp)|j\rangle \\ F(g,g:\vec{q}) &= \sum_i \sum_j \int e^{iq_z z} g_i(z) g_j(z) dz \langle i|A(q_\perp)|j\rangle. \end{aligned} \tag{2.61}$$

We can evaluate the expressions of $\langle i|A(q_\perp)|j\rangle$ by the same transformation to semi-classical states that we used in appendix B. The result is

$$\langle i|A(q_\perp)|j\rangle = \sum_{p=max(j-i,0)}^{j} \frac{\sqrt{i!j!}(\frac{-|q_\perp|^2}{2})^p(\frac{q^*_\perp}{\sqrt{2}})^{i-j}}{(j-p)!(i-j+p)!p!}. \tag{2.62}$$

The integration over the variable $\vec{q}$ can be done partially by the use of complex analysis. We will break the correction terms into three parts: RPA, exchange self-energy, and local-field correction to exchange. The RPA energy is

$$E_{rpa}(\vec{k_\perp}) = \frac{\nu}{\pi} \int \frac{dq_z}{k_\perp^2 + q_z^2} e^{-\frac{|k_\perp|^2}{2}} \left|F(+,g:\vec{k_\perp} - \vec{q_z})\right|^2. \tag{2.63}$$

The exchange self-energy is

$$E_{exch} = -\int \frac{d^3q}{(2\pi)^3} \frac{4\pi}{q^2} \; e^{-\frac{|q_\perp|^2}{2}} \left\{|F(g,+:\vec{q})|^2 - |F(g;g:\vec{q})|^2\right\}. \tag{2.64}$$

The local-field correction is

$$E_{local} = -\int \frac{d^3q}{(2\pi)^3} \frac{4\pi}{q^2} \; e^{-\frac{|q_\perp|^2}{2}} \; e^{-\frac{k_\perp q^*_\perp - k^*_\perp q_\perp}{2}} F(+,+:\vec{q}) F(g,g:-\vec{q}). \tag{2.65}$$

We will now specialize to the case of $\nu = 2$ since our experiment only covers the localization region near $\nu = 2$.

2.2.4 Random-phase approximation

The integration over q_z in the correction terms can be evaluated by the Cauchy Integral Theorem: the closed-path integral is equals to the $2\pi i$ times the sum of the residues inside. If we substitute in the expression for the $F(+, g : \vec{k_\perp} - \vec{q_z})$ into Eq. (2.63), we have,

$$\begin{aligned} E_{rpa}(\vec{k_\perp}) &= \frac{\nu}{\pi}\int_{-infty}^{\infty}\frac{dq_z}{k_\perp^2+q_z^2}e^{-\frac{|k_\perp|^2}{2}}\langle +|e^{iq_z z}A(-k_\perp)|g\rangle\langle g|e^{-iq_z x}A(k_\perp)|+\rangle \\ &= \frac{\nu}{\pi}\int_{-\infty}^{\infty}dz\int_{-\infty}^{\infty}dx\int dq_z\frac{e^{iq_z(z-x)}}{k_\perp^2+q_z^2}e^{-\frac{|k_\perp|^2}{2}}\sum_{n,p,j,l}g_n(x)f_p(x)f_j(z)g_l(z) \\ &\qquad \langle n|A(k_\perp)|p\rangle\langle j|A(-k_\perp)|l\rangle. \end{aligned} \tag{2.66}$$

The integral over q_z can be done via standard contour integration:

$$\int_{-\infty}^{\infty}\frac{dq_z}{k_\perp^2+q_z^2}\ e^{iq_z(z-x)} = \pi\frac{e^{-|k_\perp||z-x|}}{|k_\perp|}, \tag{2.67}$$

then

$$\begin{aligned} E_{rpa}(k_\perp) &= \nu\frac{e^{-\frac{|k_\perp|^2}{2}}}{|k_\perp|}\int dz\int dx\sum_{n,p,j,l}e^{-|k_\perp||z-x|}g_n(x)f_p(x)f_j(z)g_l(z) \\ &\qquad \langle n|A(k_\perp)|p\rangle\langle j|A(-k_\perp)|l\rangle. \end{aligned} \tag{2.68}$$

In most optical experiments, the wave vector $\vec{k}_\perp$ is very small. For $\vec{k}_\perp = 0$, Eq. (2.68) has the limiting value

$$E_{rpa}(0) = -\nu\int dz\int dx\sum_{n,l}|z-x|g_n(x)f_n(x)f_l(z)g_l(z). \tag{2.69}$$

In deriving Eq. (2.69), we have used the fact that $\langle n|A(0)|p\rangle = \delta_{n,p}$. Equation (2.69) has the exact same form as the Hartree energy except that the wave functions involved are not just the ground state.

2.2.5 Exchange

If we substitute the definition of F into Eq. (2.64), we have

$$E_{exch} = -\frac{1}{2\pi^2}\int\frac{d^3q}{q^2}\int dx\int dz e^{iq_z(z-x)}\ e^{-\frac{|q_\perp|^2}{2}} \sum_{n,p,j,l}(g_n(z)f_p(z)f_j(x)g_l(x)-g_n(z)g_p(z)g_j(x)g_l(x))\langle n|A(q_\perp)|p\rangle\langle j|A(-q_\perp)|l\rangle. \tag{2.70}$$

The use of Eq. (2.67) for the evaluation of the integral over q_z results in

$$E_{exch} = -\frac{1}{2\pi}\int d^2q_\perp\int dx\int dz\ e^{-\frac{|q_\perp|^2}{2}}\frac{e^{-|q_\perp||z-x|}}{|q_\perp|} \sum_{n,p,j,l}(g_n(z)f_p(z)f_j(x)g_l(x)-g_n(z)g_p(z)g_j(x)g_l(x))\langle n|A(q_\perp)|p\rangle\langle j|A(-q_\perp)|l\rangle. \tag{2.71}$$

Replacing the expressions of the type $\langle n|A(q_\perp)|p\rangle$ with its definition in Eq. (2.62) and performing the integral over the angle of $q_\perp$, we can achieve the final expression for the exchange self-energy:

$$\begin{aligned}E_{exchange} = -\int dz\int dx\int_0^\infty d|q_\perp|\sum_{n,p,j,l}(-1)^{j-l}\delta(n-p+j-l)e^{-\frac{|q_\perp|^2}{2}-|q_\perp||z-x|} \\ \sqrt{n!p!j!l!}\,(g_n(z)f_p(z)f_j(x)g_l(x)-g_n(z)g_p(z)g_j(x)g_l(x)) \\ \sum_{\alpha=max(p-n,0)}^{p}\frac{(\frac{-|q_\perp|^2}{2})^\alpha}{(p-\alpha)!(n-p+\alpha)!\alpha!} \\ \sum_{\beta=max(l-j,0)}^{l}\frac{(\frac{-|q_\perp|^2}{2})^\beta}{(l-\beta)!(j-l+\beta)!\beta!}.\end{aligned} \tag{2.72}$$

Similar to the Hartree energy, the exchange self-energy is completely independent of the wave vector of the excitation. We can interpret the expression in Eq. (2.72) as the difference in the exchange self-energy of the electron in two different levels. The first term , involving $g_n(z)f_p(z)f_j(x)g_l(x)$, can be regarded as the exchange self-energy of the electron in the excited state while the second term, involving $g_n(z)g_p(z)g_j(x)g_l(x)$, can be regarded as the exchange self-energy of the electron in the ground state.

2.2.6 Local-field correction

The evaluation of the local-field correction will be very similar to the exchange self-energy term since they both arise from the exchange of electrons. The major difference is the evaluation of $e^{-\frac{k_\perp q_\perp^* - k_\perp^* q_\perp}{2}}$. We will approach the problem by expanding it in terms of Bessel functions:

$$\begin{aligned} e^{-\frac{k_\perp q_\perp^* - k_\perp^* q_\perp}{2}} &= e^{-i(k_y q_x - k_x q_y)} \\ &= e^{i\vec{k_\perp} \times \vec{q_\perp}} \\ &= e^{ik_\perp q_\perp sin(\theta_{k_\perp} - \theta_{q_\perp})} \\ &= \sum_{m=-\infty}^{\infty} e^{im(\theta_{k_\perp} - \theta_{q_\perp})} J_m(|k_\perp||q_\perp|), \end{aligned} \tag{2.73}$$

where $J_m(k_\perp q_\perp)$ is the Bessel function of order m. We can now substitute the expansion into Eq. (2.65):

$$\begin{aligned} E_{local} = & -\frac{1}{2\pi^2} \int \frac{d^3q}{q_\perp^2 + q_z^2} \; e^{-\frac{|q_\perp|^2}{2}} \sum_{m=-\infty}^{\infty} e^{im(\theta_{k_\perp} - \theta_{q_\perp})} J_m(|k_\perp||q_\perp|) \\ & \sum_{p,j} \int dz f_p(z) f_j(z) \langle p|A(q_\perp)|j\rangle e^{iq_z z} \\ & \sum_{r,s} \int dx g_r(x) g_s(x) \langle r|A(-q_\perp)|s\rangle e^{-iq_z x}. \end{aligned} \tag{2.74}$$

We can substitute in the definition of $A(k_\perp)$, integrate over q_z using Eq. (2.67), and integrate over the angle of $q_\perp$ to achieve the final expression for the local field correction,

$$\begin{aligned} E_{local}(\vec{k_\perp}) = & -\int dz \int dx \int_0^\infty d|q_\perp| \sum_{p,j,r,s} (-1)^{r-s} J_t(|k_\perp||q_\perp|) e^{-\frac{|q_\perp|^2}{2} - |q_\perp||z-x|} \\ & (\frac{|q_\perp|}{\sqrt{2}})^t \sqrt{p!j!s!r!} f_p(x) f_j(x) g_r(z) g_s(z) e^{it\theta_{k_\perp}} \\ & \sum_{\alpha=max(j-p,0)}^{j} \frac{(\frac{-|q_\perp|^2}{2})^\alpha}{(j-\alpha)!(p-j+\alpha)!\alpha!} \\ & \sum_{\beta=max(s-r,0)}^{s} \frac{(\frac{-|q_\perp|^2}{2})^\beta}{(s-\beta)!(r-s+\beta)!\beta!}. \end{aligned} \tag{2.75}$$

In Eq. (2.75), we have defined $t = p - j + r - s$. In the limit $\vec{k}_\perp \to 0$, because $J_m(0) = \delta_{m,0}$, Eq. (2.75) becomes

$$\begin{aligned} E_{local}(0) &= -\int dz \int dx \int_0^\infty d|q_\perp| \sum_{p,j,r,s} (-1)^{r-s} \delta_{t,0} e^{-\frac{|q_\perp|^2}{2} - |q_\perp||z-x|} \\ &\quad (\frac{|q_\perp|}{\sqrt{2}})^t \sqrt{p!j!s!r!} f_p(x) f_j(x) g_r(z) g_s(z) \\ &\quad \sum_{\alpha=max(j-p,0)}^{j} \frac{(\frac{-|q_\perp|^2}{2})^\alpha}{(j-\alpha)!(p-j+\alpha)!\alpha!} \\ &\quad \sum_{\beta=max(s-r,0)}^{s} \frac{(\frac{-|q_\perp|^2}{2})^\beta}{(s-\beta)!(r-s+\beta)!\beta!}. \end{aligned} \tag{2.76}$$

When the magnetic field is perpendicular to the plane of 2DEG, the dispersion of the singlet and triplet excitations are independent of the direction of the wave vector, since there is nothing to distinguish the various directions. This is shown in Fig. 2-5 for sample A. The angles of 45 degrees and 90 degrees refers to the angle between the wave vector and y-axis. When there is an in-plane component of magnetic field, the in-plane isotropy is broken. The preferred direction is the direction of the in-plane magnetic field. In the calculations carried out, the magnetic field direction is the y-axis. In Figs. 2-6 and 2-7, we have shown the dispersion of the singlet and triplet excitations. The curves are labeled by the angle between $\vec{k}_\perp$ and $B_\perp$. The curves corresponding to 90 deg have $\vec{k}_\perp$ directed along the positive x-axis while $B_\perp$ is directed along the positive y-axis. In Figs. 2-6 and 2-7, the dispersion curves of the triplet excitation are the lower energy curves with very small negative dispersion near $k_\perp = 0$, while the singlet state dispersion curves are the higher energy curves with sharp positive dispersion. Three features in tilted-field dispersion curves are worth noting. The dispersion curves are no longer isotropic. The anisotropic behavior increases with increasing tilt angle: at 30 degrees (Fig. 2-6), all directions are similar while at 60 degrees (Fig. 2-7) the dispersion curves are very different. Then, there is a energy gap between the singlet and triplet states which is not present in the case with perpendicular magnetic field. Finally, the dispersive character of the triplet state has changed. In the perpendicular field case, the minimum in the triplet state dispersion

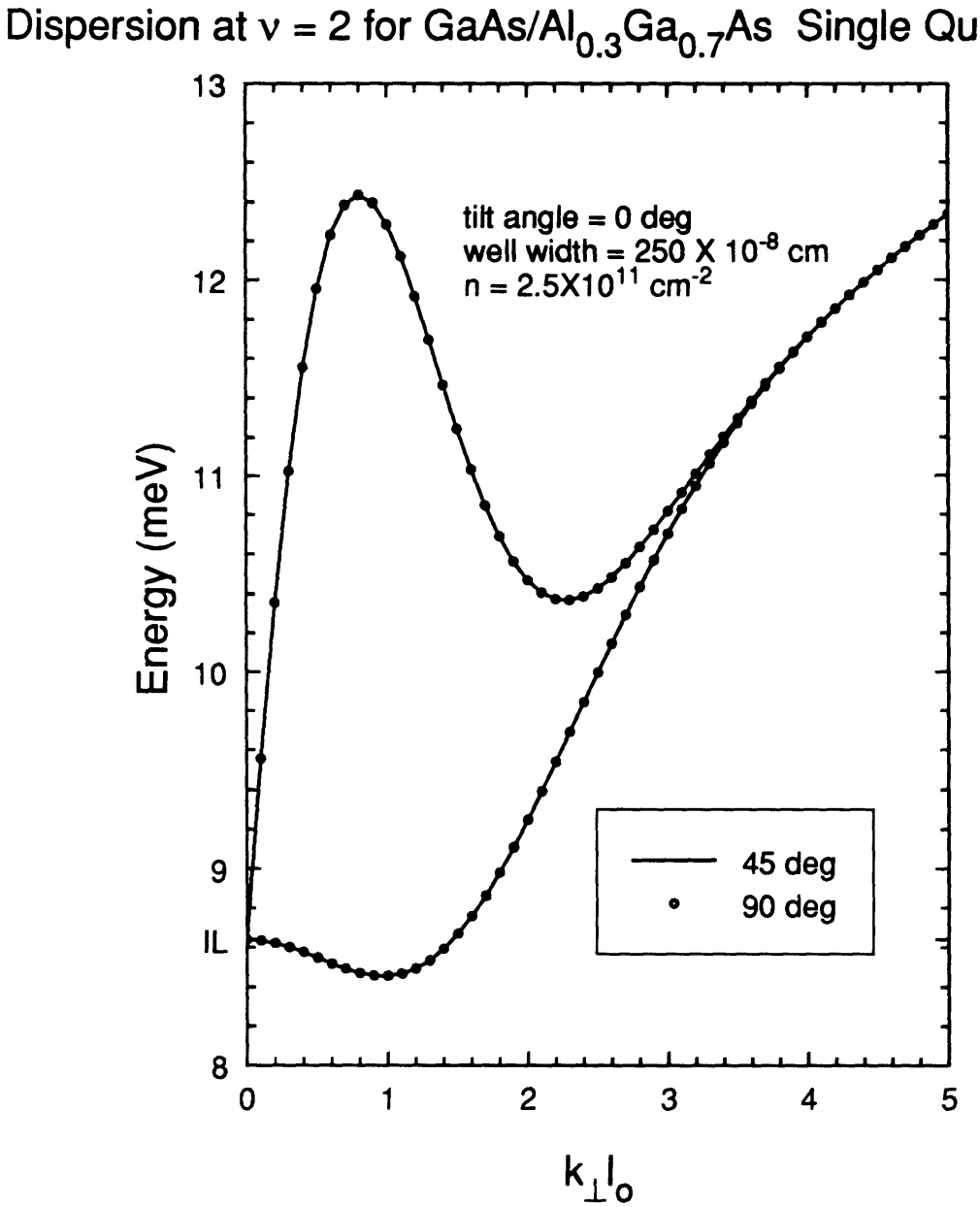

Figure 2-5: The dispersion of the singlet and triplet excitations. The effective mass is 0.067 times the bare electron mass. The parameters used in the numerical calculation is listed in table 3-1. The curves are calculated with $\nu = 2$ and $B_\perp = 5T$.

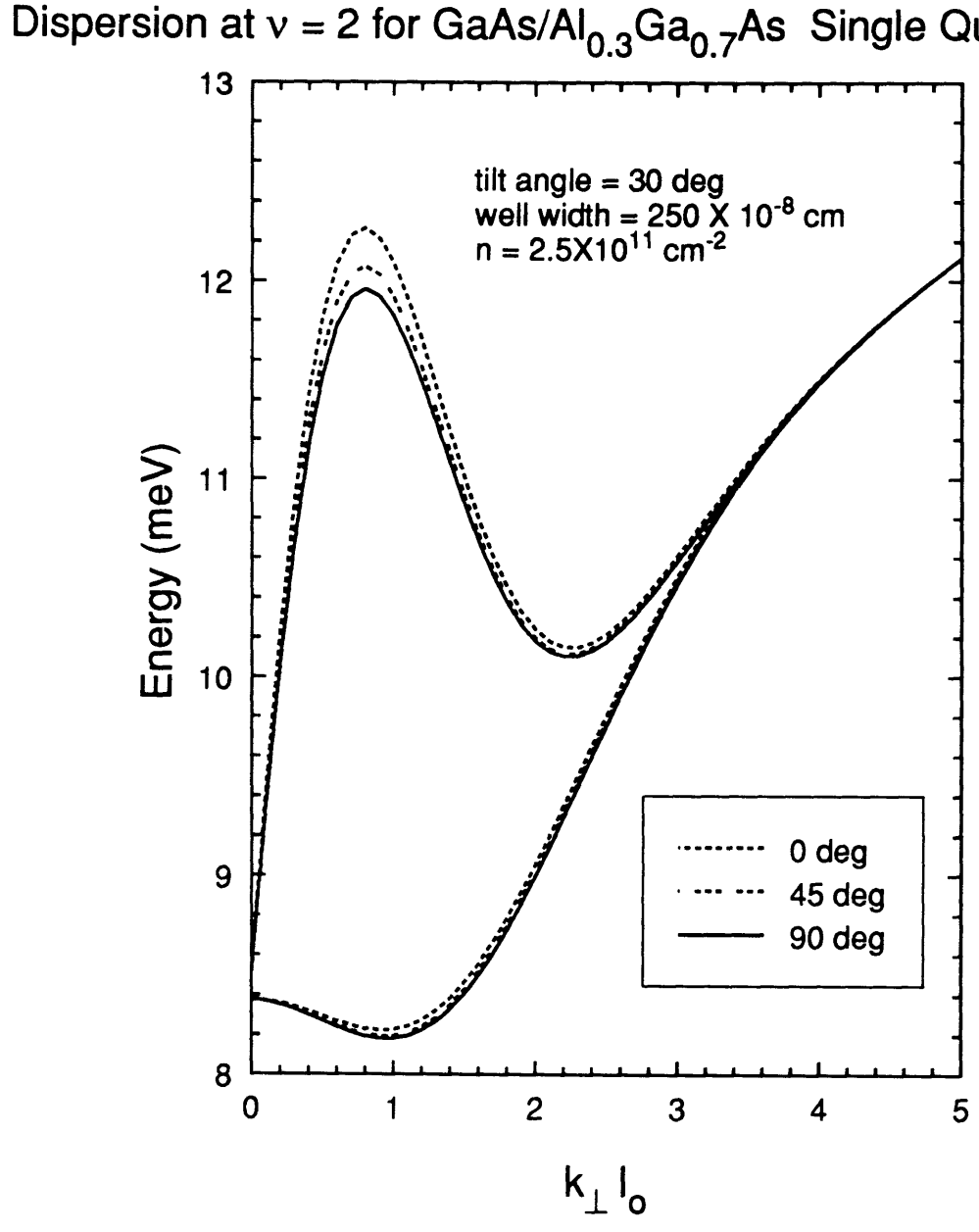

Figure 2-6: The dispersion of the singlet and triplet excitations at 30 deg tilt angle. The effective mass is 0.067 times the bare electron mass. The parameters used in the numerical calculation is listed in table 3-1. The curves are calculated with $\nu = 2$ and $B_\perp = 5T$.

is nearly 0.2 meV below the $k_\perp = 0$ energy, while at 60 degrees tilt the difference is almost zero.

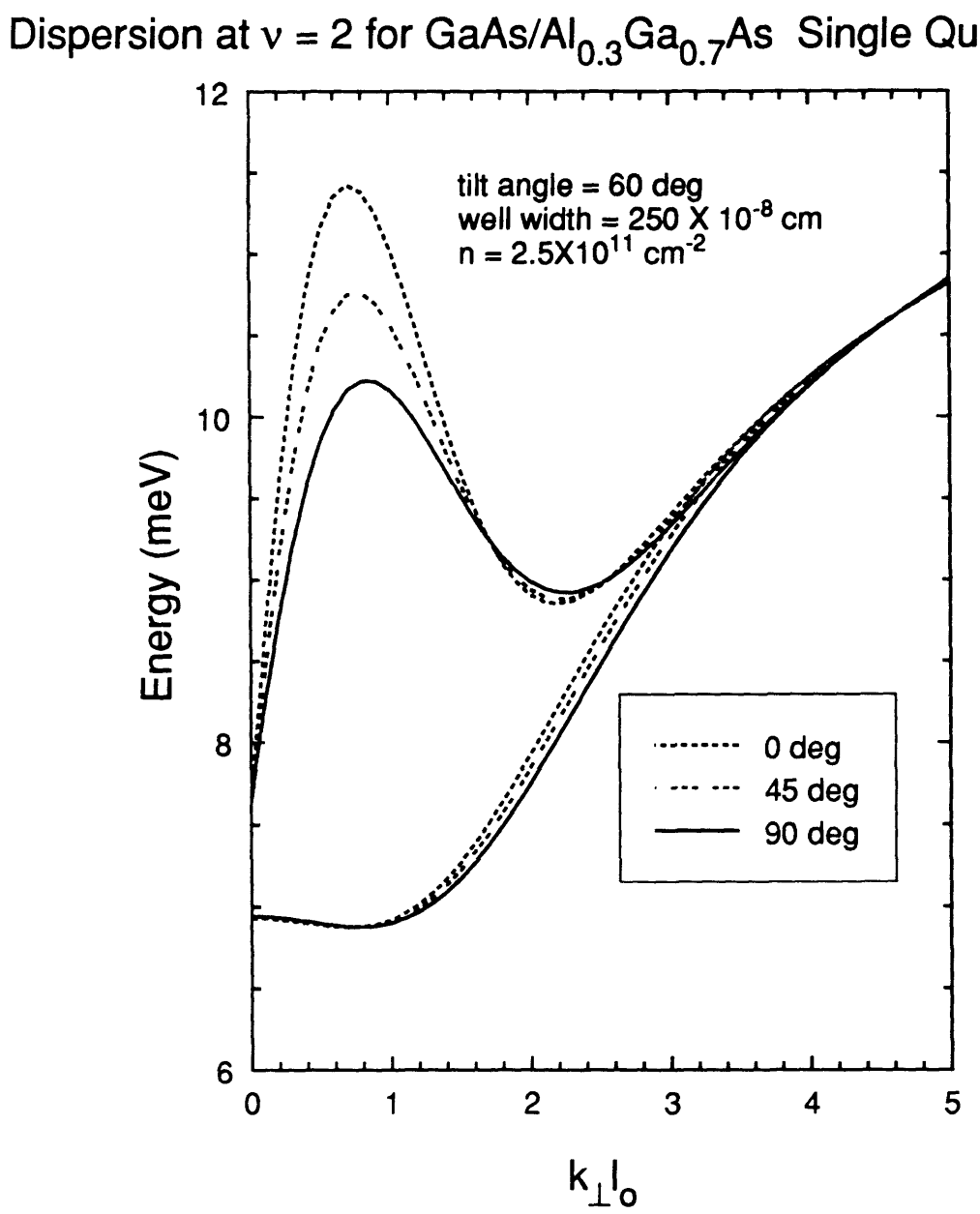

Figure 2-7: The dispersion of the singlet and triplet excitations at 60 deg tilt angle. The effective mass is 0.067 times the bare electron mass. The parameters used in the numerical calculation is listed in table 3-1. The curves are calculated with $\nu = 2$ and $B_\perp = 5T$.

Chapter 3

Square Quantum Wells

In the extreme quantum limit, interesting phenomena such as the Integer Quantum Hall Effect (IQHE) and Fractional Quantum Hall Effect (FQHE) have been observed in high-mobility single quantum wells and heterojunctions [34, 36]. IQHE is the result of gauge invariance and is extremely robust. It can be observed even in samples with low mobilities. In fact, it is critical that the sample has enough impurities so that there is localization for the IQHE to be observable. The plateau region corresponds to where the Fermi energy is pinned at the localized states. FQHE on the other hand, is the result of electron-electron interaction. Hence, FQHE is only observed in high-mobility samples. IQHE and FQHE are both phenomena in transport measurements. One would expect that the optical measurements of two-dimensional electronic system in high magnetic field will also shed light on the effect of many-body interactions between the electrons. Using inelastic light scattering, Pinczuk *et al.* [27, 29] have observed the collective modes of the two-dimensional electron gas both in IQHE regime and FQHE regime. At the IQHE plateau region where the electrons are in the mobility gap, it is possible to observe the density of the states of the charge- and spin-density excitations due to the ineffective screening [29]. In this chapter, we present the experimental results on the effects of tilted magnetic fields on the collective excitations.

Table 3.1: Single Quantum Well Sample Parameters

sample name	surface charge density	mobility	well width
A	2.5×10^{11} /cm^2	3.0×10^6 cm^2/Vs	250 Å
B	3.6×10^{11} /cm^2	2.8×10^6 cm^2/Vs	250 Å

3.1 Experimental

3.1.1 samples

Two high-mobility samples of GaAs/$Al_xGa_{1-x}As$ single quantum well with $x \cong 0.3$ were studied in detail in high magnetic fields. The parameters of the samples are listed in table 3.1. The discontinuity of the potential at the edge of the well is 225 meV for $x = 0.3$. We have studied the samples at various tilt angles, $\phi = 0°$, 30°, 45°, 60°, near $\nu = 2$. The tilt angle is defined as the angle between the normal to the sample and the magnetic field. Thus, zero tilt angle corresponds to the Faraday configuration.

3.1.2 Light-scattering set-up

The experiment was carried out either in an optical dewar or with a two-fiber optical-fiber probe. The set-up for the optical dewar in shown in Fig. 3-2. The maximum field accessible with the optical dewar is only 11 T. In order to study the higher density sample near $\nu = 2$, we had to use magnets without optical access. The delivery and collection of light in this case in done with a two-fiber optical probe. The probe has a $100\mu m$ fiber for delivery of light. The light source is a Krypton-laser pumped-continuous wave dye laser. Once the light is delivered near the sample holder, the light is collimated with a GRIN lens and then turned by an angled mirror at 22.5°. The light then hits the sample at 45°. The scattered light from the sample is then collected by a small lens. The lens position is adjusted such that the sample is located at its focal plane. The signal is then collimated after the collection lens. It enters a $600\mu m$ fiber to travel out of the probe. At the end, the light is finally focused into a

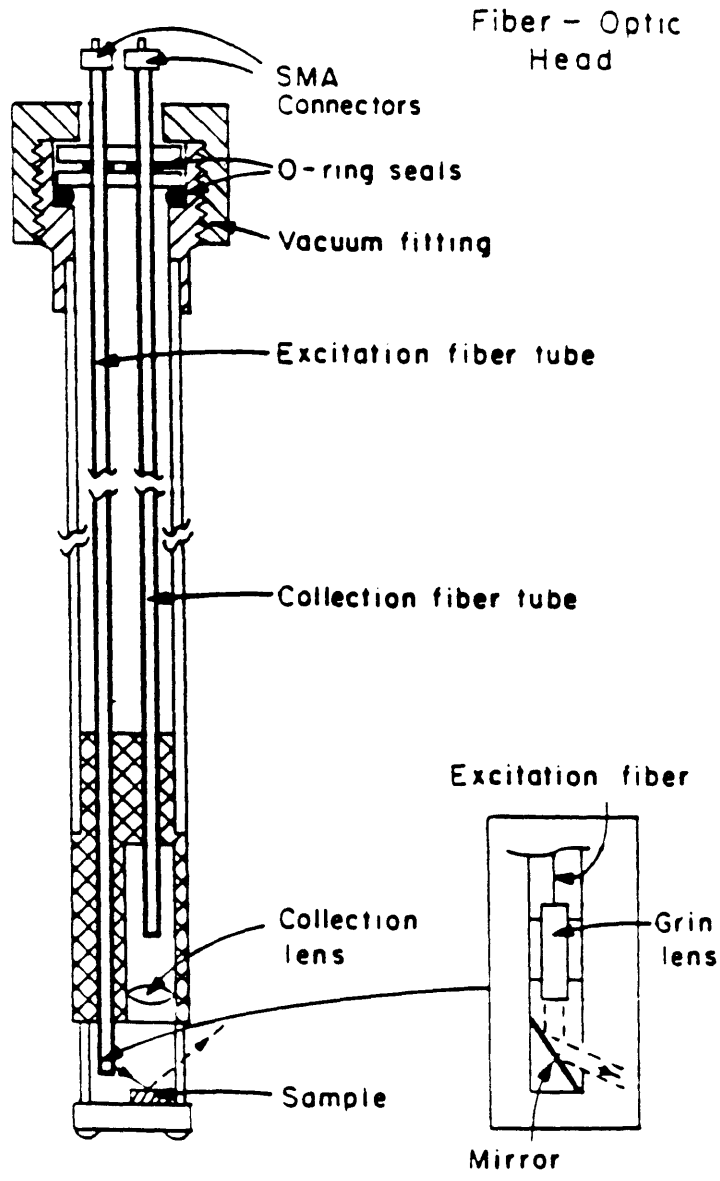

Figure 3-1: Two-fiber optical probe

spectrometer entrance slit and detected at the spectrometer output either by a PMT or CCD camera. The optics within the probe are all held in position by plates made of low-temperature epoxy. The plastic probe will allow rapid field sweeps without the associated eddy current heating. The schematic diagram for the two fiber probe is shown in Fig. 3-1.

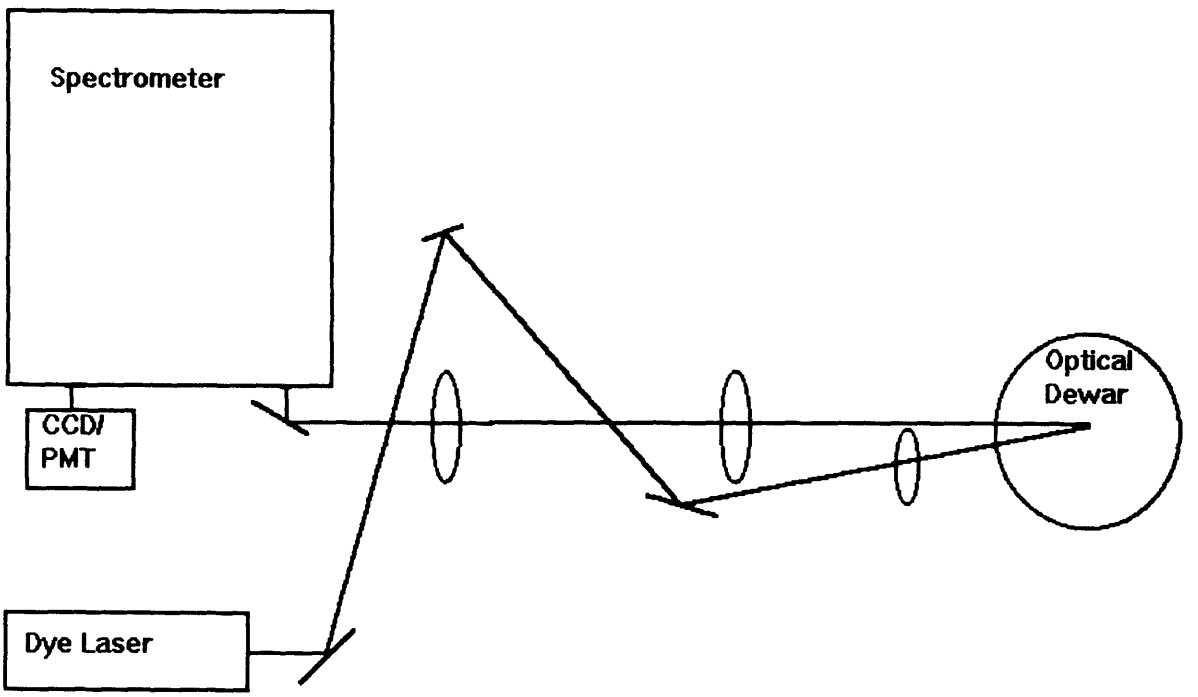

Figure 3-2: Optical dewar set up for light scattering.

3.2 Tilted Magnetic Field

As was pointed out in Ch. 2, the physical systems which realize 2DEG are only approximately two dimensional. One way to study the effect of the extent of the wave function in the z direction is to study the intersubband transition. Another is to study the 2DEG with tilted magnetic fields. If there is an in-plane component of magnetic field, it will couple the IS and IL transitions. Instead of a magnetic field independent IS transition and a field dependent IL transition, both transitions are now field dependent. The higher energy transition is labeled upper hybrid (UH) transition and the lower energy one is labeled lower hybrid (LH) transition. This chapter will concentrate on the LH transition. It is worth noting that as the tilt angle ϕ goes to zero, LH transition becomes the IL transition which is not a dipole allowed Raman transition. Thus, without tilt, the IL transition is expected to be observable only in the plateau region of IQHE, as part of the density of states. In the presence of non-zero tilt angle, the LH transition should be observable at all fields because of the mixing with the IS transition.

Figure 3-5 shows the representative spectra at $\nu = 2$ from sample B at tilt angles of 0, $\frac{\pi}{6}$, $\frac{\pi}{4}$, and $\frac{\pi}{3}$. Similar behavior is observed for both high- and low-density samples: the shifting of the entire spectral feature to lower energy as the tilt angle is increased and the presence of a strong new peak with spectral position slightly above the single particle energy. The shifting of spectra to the lower energy is explained easily by the anti-crossing of the UH and LH modes. In order to keep the $B_\perp$ constant as the tilt angle is increased, the total magnetic field must increase as well. The increase in the total magnetic field also means that the in-plane component of magnetic field, which is responsible for the coupling of UH and LH hybrid modes, is also increasing. Thus, bigger tilt angle means stronger anti-crossing. The presence of the new peak is more difficult to explain. Figure 3-3 plots the Raman spectra for sample A at several different filling factors in the range from $\nu = 2.7$ to $\nu = 1.4$. The magnetic field dependences of the peaks are worth noting in two ways: the persistence of the upper spectral peak outside of the localization region and the disappearance of the lower

energy feature to the higher magnetic field side of $\nu = 2$. The persistence of the upper energy feature at all fields suggests that it is the LH charge-density excitation. The disappearance of the spin-density excitation is not surprising since as the magnetic field is changing, the spin characteristic of the ground state is also varying. At $\nu = 2$ all three types of spin-density excitations are allowed while at $\nu = 1$ only two are allowed. The energy of the spin excitation relative to the LH transition energy also changes dramatically from $\nu = 2$ to $\nu = 1$, as shown in Figs. 2-4 and 2-1. We note that the shift from the single-particle energy for the peaks are on the order of 1 to 2 meV. This rules out the possibility that these peaks are due to impurities located in the center of the quantum well, since such impurities will have transition energy of approximately 7 meV for our experimental condition [17, 9]. Furthermore, as can be seen from Fig. 3-4, it does not depend very much on temperature in the range from 5 deg Kevin to 15 deg Kevin. This rules out the possibility that these peaks are due to shallow barrier impurity states [25, 31]. In addition to the new peak and the shift to the lower energy, we also observed a broadening of the spectral features associated with the spin-density excitation for the lower density sample as the tilt angle is increased. Figure 3-6 shows the representative spectra from sample A at $\phi = 60°$ at $\nu = 2$. The vertical dashed lines are guides for the eye. Each spectrum is labeled by the laser energy used to acquire the data. At low-excitation energy, the higher energy feature is dominant. At a laser energy of roughly 1550 meV both features are visible. For higher laser energy values, only the lower energy feature is visible. The separation between the two peaks is 0.2 meV, roughly equals to the separation between the energy at $k_\perp = 0$ and the energy at the minimum of the dispersion.

In addition to the dependence on magnetic fields and temperature, it is also useful to study the energy gap between the charge-density and spin-density excitations at $\nu = 2$ as a function of the tilt angle. At integral filling factors, we can confidently apply the self-consistent calculation developed in Ch. 2. We recall that the parabolic confinement potential model did not achieve good results (Fig. 2-2). It is necessary to apply the numerical approach outlined in section 2.2. Figures 3-7 and 3-8 show

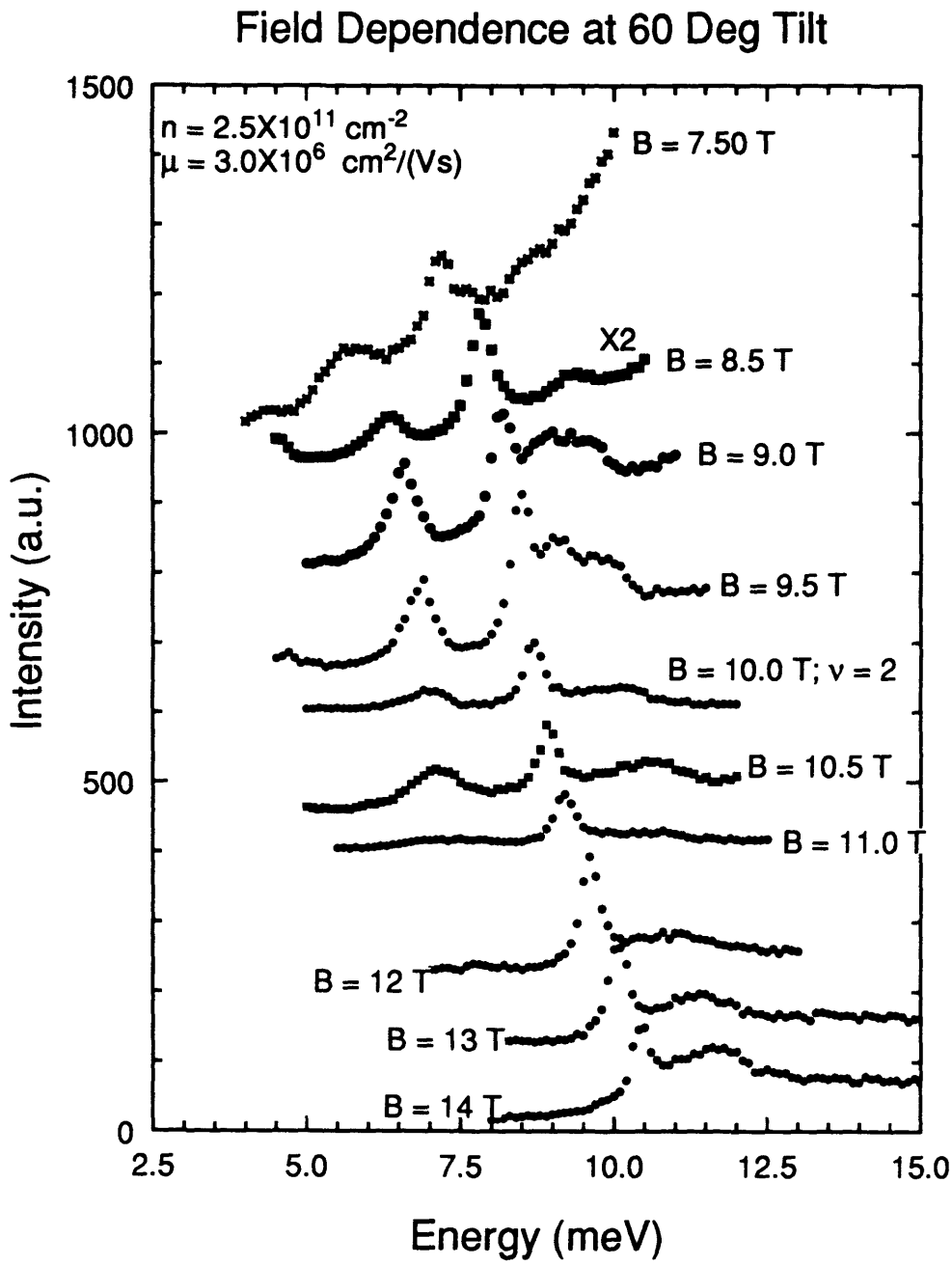

Figure 3-3: Resonant Raman spectra at 60 ° tilt angle for sample A at various filling factor values.

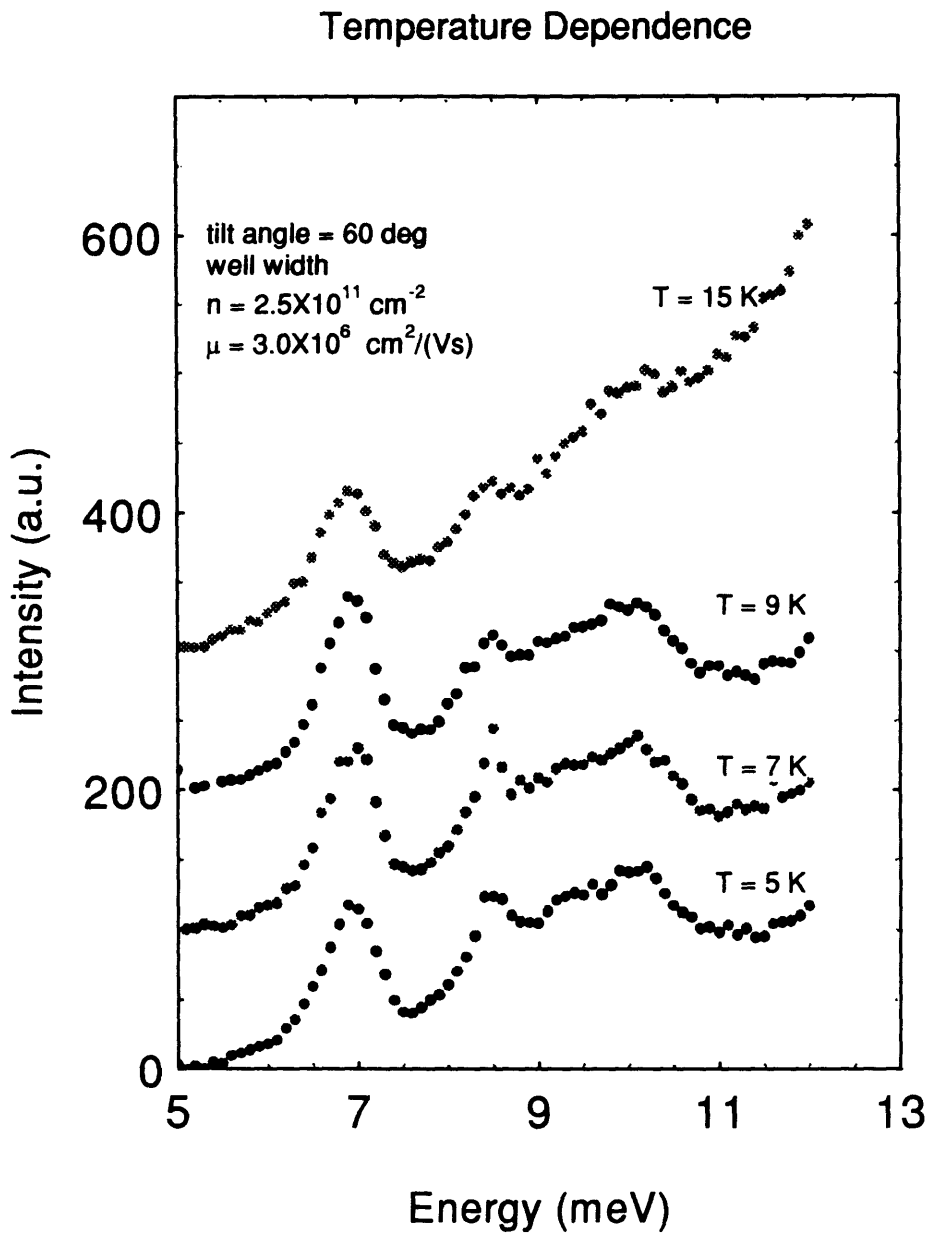

Figure 3-4: Temperature dependence at 60 ° tilt angle for sample A.

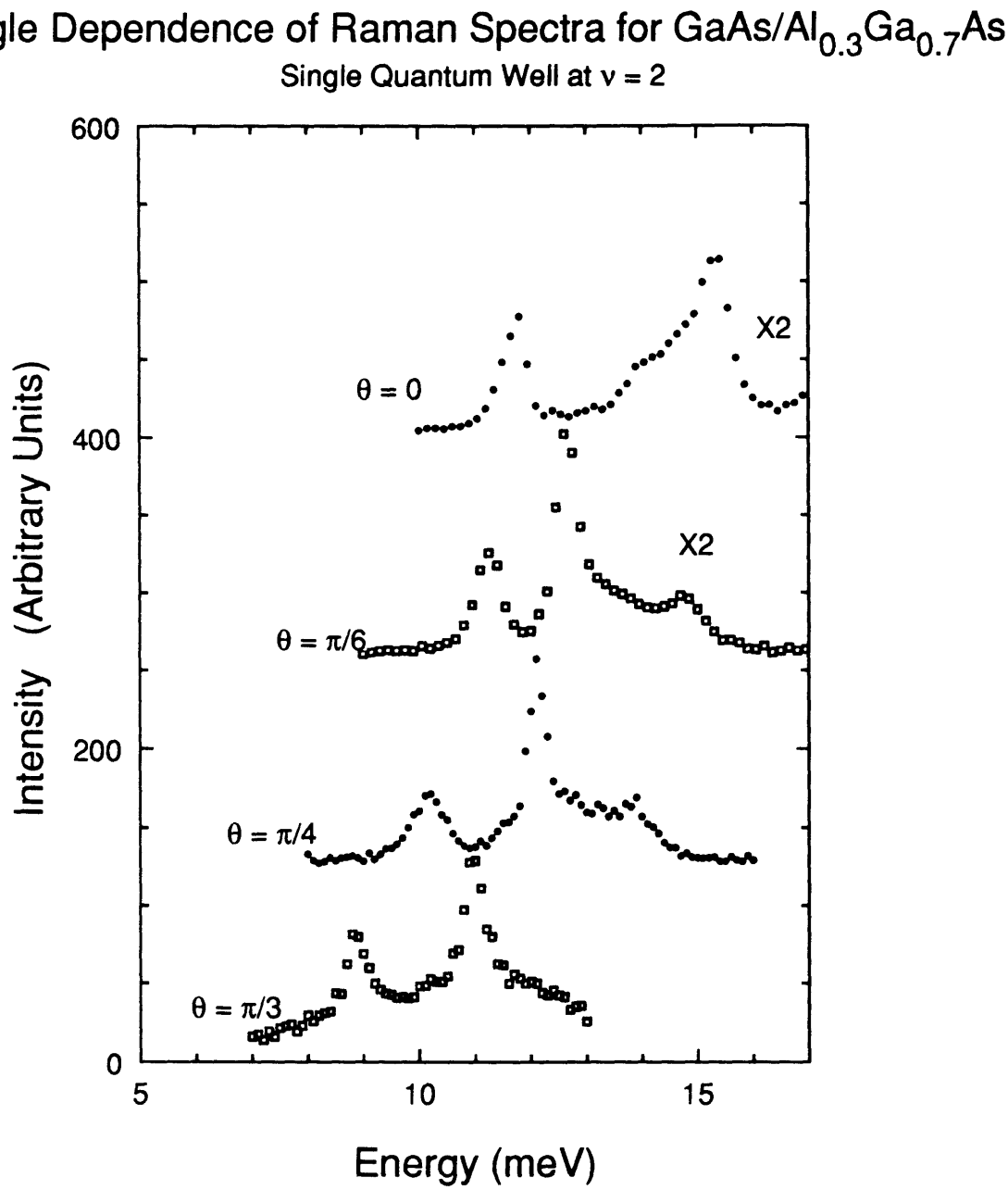

Figure 3-5: Raman spectra at various tilt angles for the higher density sample.

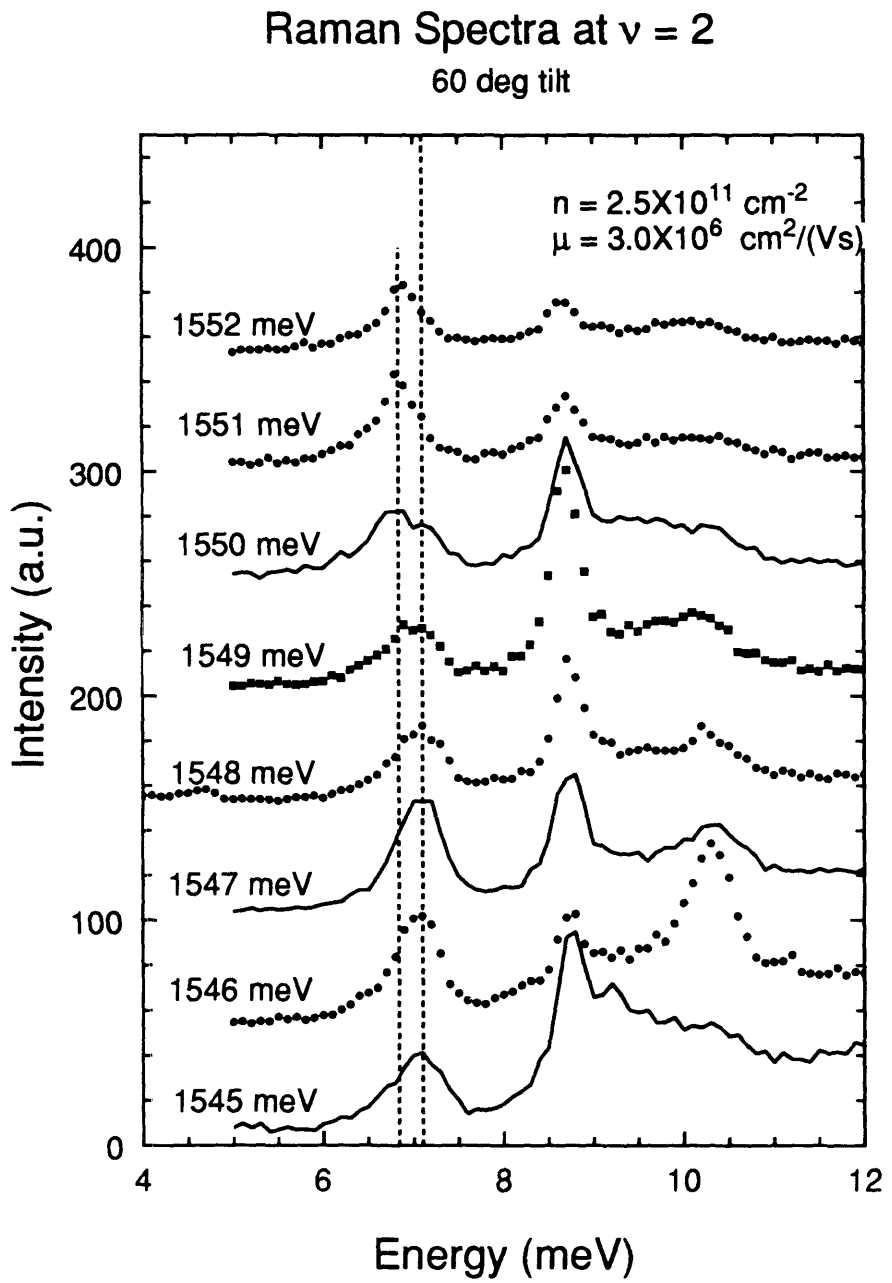

Figure 3-6: Resonant Raman spectra at 60 ^{o} tilt angle for sample A.

computational results and experimental points for the low-density and high-density samples, respectively. The agreement is much better than the parabolic confinement model. The energy gap between the charge- and spin-density excitations is a strong function of the tilt angle. It is however, not a straightforward trigonometric function, nor is it linear. In fact for the sample with the higher density, the increase in the size of the gap from 45 degrees tilt to 60 degrees tilt is much less than the corresponding increase in the lower density sample. In both Figs. 3-7 and 3-8 the spin-density spectral positions start out with energy values below the calculated curves at zero tilt angle and approaches the calculated curve as the tilt angle is increased. This can be explained by the fact that at small tilt angles, we are observing the minimum in the spin density dispersion which is lower in energy than the momentum conserving triplet excitation. As the tilt angle is increased, the minimum moves toward $k_\perp = 0$. As a result, the energy difference between the momentum conserving triplet excitation and the minimum is diminished.

The calculation outlined in Ch. 2 can also be used to calculate the density of states of the excitations at integral filling factors. Instead of calculating the density of states directly, we will weigh each state with a probability and then calculate the density of states from the weighted dispersion. We will chose the weighting such that the probability of creating a very large wave vector excitation is small. In the calculation of density of states, each state will be weighted with a factor of $e^{-\frac{|k_\perp|^2}{2}}$. This is a probabilistic weighting which assumes that the probability of observing the excitation with wave vector $\vec{k}_\perp$ is a Gaussian distribution of its difference from the momentum conserving wave vector. Basically, this procedure broadens the delta function normally associated with momentum conservation. In Fig. 3-9, we have plotted both the spectra and the calculated density of states for sample B. We have shifted all the calculated curve 0.4 meV lower in energy so that the spin density features are aligned between the experimental spectra and the calculated density of states. The spectra and the calculated curves are off set from each other for easy viewing. The strong spin density feature is retained in the calculated density of states for all tilt angles while the charge density excitation features are diminished

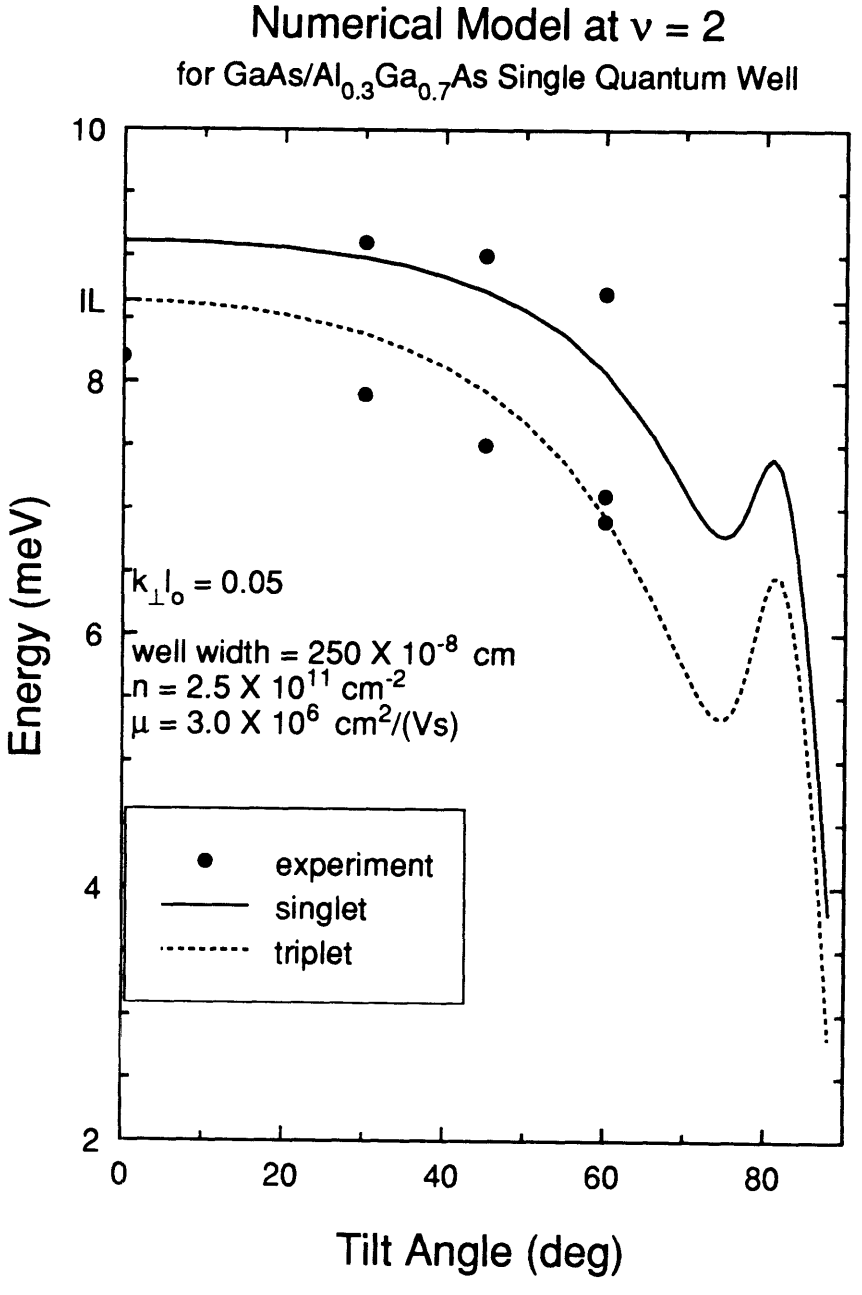

Figure 3-7: The curves are the energy curves for the singlet and triplet excitations as a function of tilt angle for sample A. The in-plane wave vector value is taken to be $|k_\perp|\ell_o = 0.05$.

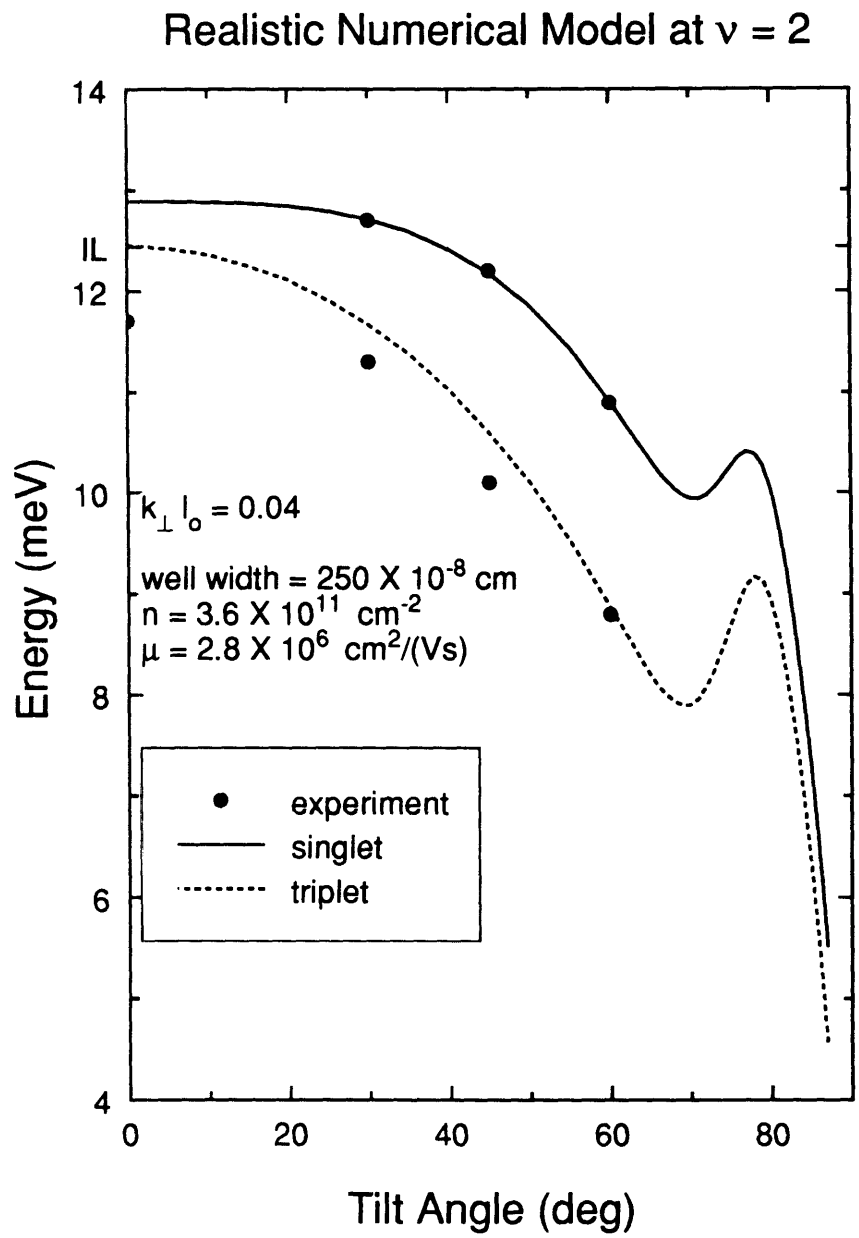

Figure 3-8: The curves are the energy curves for the singlet and triplet excitations as a function of tilt angle for sample B. The curves are calculated with $|k_\perp|\ell_o = 0.04$.

as the tilt angle increases. It is interesting to note that this appears to be the case both for the experiment and the calculated density of states. It is clear from Fig. 3-9 that the higher energy peak in the spectra does not correspond to a peak in the density of states. Instead, it must be the momentum-conserving charge-density excitation. From Fig. 3-7, 3-8, and 3-9, we see that the time-dependent Hartree-Fock calculation appears to give a reasonable account of the data provided that one models the confinement potential realistically.

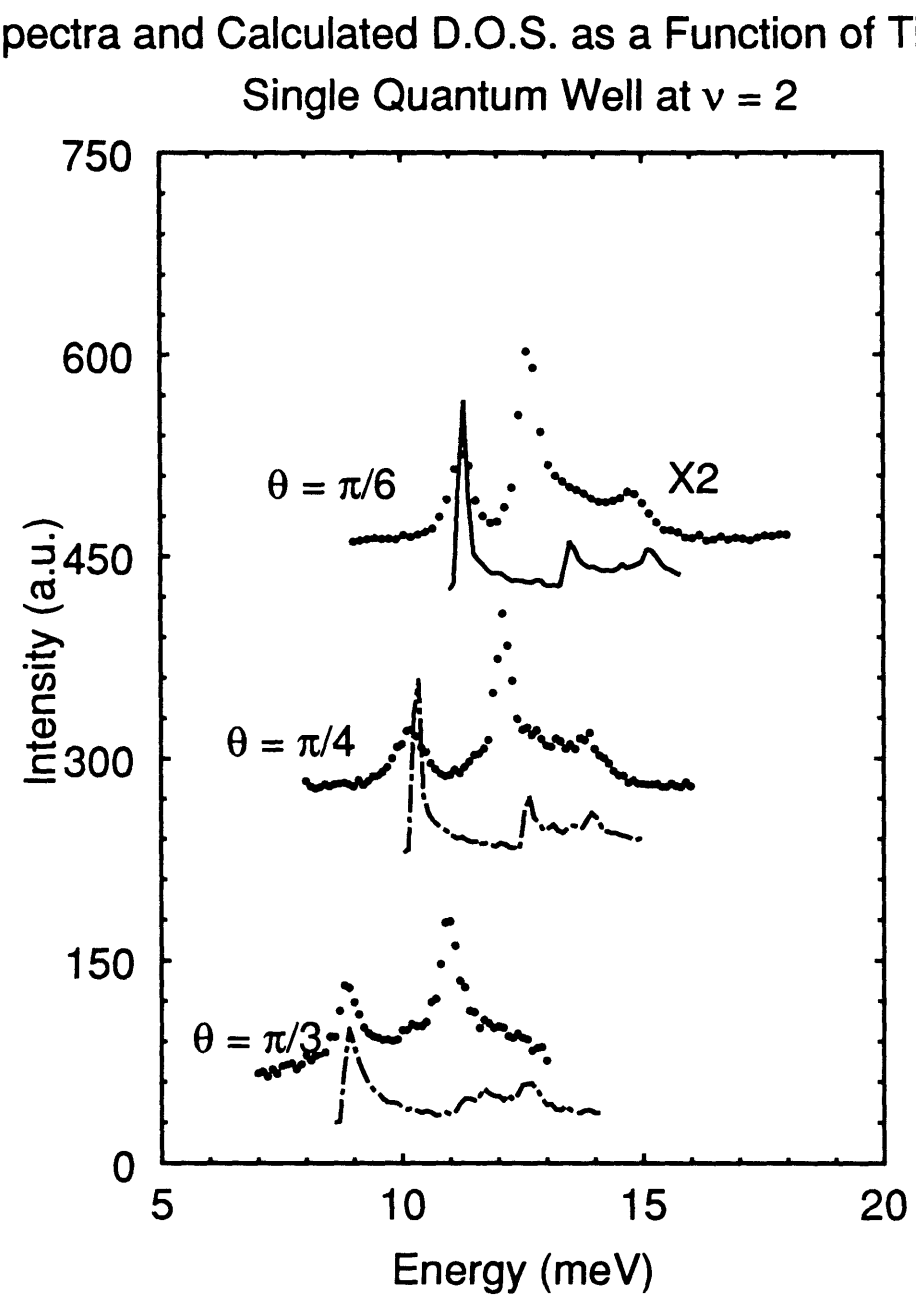

Figure 3-9: The solid dots are the experimental spectra while the dashed and solid curves are the calculated density of states. The parameters used for the calculation are those of sample B.

Chapter 4

Wide Parabolic Wells

In the previous chapters, we saw that MBE can be used to fabricate solid state systems with desired characteristics. One system which has attracted much recent attention is the parabolic quantum well. The reason this interest is that remotely-doped parabolic quantum wells are structures that realize a wide, uniform-density electron slab. Due to electrostatic interactions between electrons and between donors and electrons, electrons in a wide square well will localize around the interfaces. They separate into two coupled slabs of electron gas layers. To achieve a wide, uniform-density electron slab, a parabolic potential profile can be imposed on the conduction-band edge to simulate the potential of a uniform positive charge background. The most common type of parabolic quantum wells are made of GaAs/$Al_xGa_{1-x}As$. The parabolic potential profile is achieved by changing the average Al mole fraction as a function of the growth direction, z, in the $Al_xGa_{1-x}As$ alloy. If the parabolic conduction-band edge is $E_c(z)$, then the fictitious positive charge density in the well is $n_+ = \frac{\epsilon \mathcal{K}}{4\pi e^2}$. $\mathcal{K}$ is the curvature of the potential : $\mathcal{K} = \frac{d^2 E_c}{dz^2}$ and ϵ is the dielectric constant. In response to the fictitious positive charge background, the electrons will also form a uniform density slab inside the parabolic well such that the 3D electronic density cancels the fictitious positive charge density. The confinement subband energy levels in a parabolic quantum well in the Hartree approximation is just that of a square well with the well width equal to the width of the electron slab. Transport measurements have revealed the close subband spacings due to the wide width of the

electron slab. [10, 14]

For optical experiments such as optical absorption and Raman scattering, we need to include other approximation terms in the electron-electron interaction. For a system with parabolic potential energy, either due to magnetic field or conduction-band edge profile, Kohn's theorem states that the charge-density excitation energy must be exactly the same as the single particle-energy as $q \rightarrow 0$, [4] where q is the wave vector of the charge-density excitation. It should be pointed out that this is an exact result. Thus, optical absorption and Raman scattering must measure the bare harmonic energy of the well instead of the much reduced energy measured by transport experiments. The bare harmonic energy of the well is determined solely by the design curvature : $\hbar\Omega \equiv \hbar\sqrt{\frac{\kappa}{m^*}}$. In the case of parabolic quantum well, it can be shown that though the Hartree potential significantly reduces the subband spacings, it is exactly canceled by the time-dependent Hartree (RPA) term. Thus, it is impossible to measure any effect from the many-body interactions using Raman scattering or optical absorption as $q \rightarrow 0$. This is not the case if the well deviates from the parabolic potential or if the wave vector is finite. For example, if the well is overfilled so that the electronic wave function has appreciable amplitude near the potential step of the well, then the boundary condition is such that the modes satisfying Kohn's theorem do not exist. The possibility of detecting the effects of many-body interactions by studying the finite wave vector excitation points to a possible advantage of using Raman scattering over optical absorption. In Raman scattering, we can select the wave vector of the excitation by the geometry of the light scattering experiment. Though the wave vector will be limited to the range very near the zone center, it is still orders of magnitude larger than the wave vector of the infrared light used in the absorption experiment. In order to study the energy dispersion in the same wave vector range as Raman scattering, optical absorption experiments would require different samples with gratings of different wave vectors on the surface.

4.1 Hydrodynamic Model

Theoretically, it is very difficult to calculate the dispersion of the intersubband excitations in these wide parabolic wells. The occupations of several subbands leads to numerous coupled transitions. Thus quantum theory is very complex, requiring the diagonalization of a multidimensional many-body Hamiltonian matrix . Experimentally, however, the optical absorption spectra are very simple. They consist of one peak at the design energy. The reason is that the only charge density mode with non-zero dipole moment in a perfect parabolic well is the mode that satisfies Kohn's theorem. The situation is much more complicated if we have a slightly imperfect well. Here, we can observe various modes. One simple semi-classical approach is to use the plasma model and just calculate the dispersion using simple electrodynamics. [7] The hydrodynamic limit is achieved when the collision rate is high enough so that there is an established local equilibrium. We can then simplify the problem by starting the calculation from macroscopic consideration and avoid the need to start from Boltzmann transport equation for the distribution function. We can also simplify the problem further by assuming the mode that we are interested in is purely longitudinal. This is not too drastic an assumption since the modes of the electron slab will become radiative only when the energy of the photon is close to the energy of the excitation of interest. Retardation will become important only when the wave vector satisfies $q_r \leq \sqrt{\epsilon}\frac{\omega}{c}$. In our case, $\hbar\omega$ is roughly 10.6 meV. This leads to $q_r a \simeq 0.008$, where a is half of the well width. This is much less than the values of 0.05 and 0.21 that are relevant to our experiment. We now proceed by writing down the equations governing the system:

$$m * n[\frac{\partial v}{\partial t} + \vec{v} \cdot \nabla \vec{v}] = -en\vec{E} - en\frac{\vec{v}}{c} \times \vec{B} - n\nabla V - \nabla p, \tag{4.1}$$

$$\vec{E} = -\nabla\phi, \tag{4.2}$$

$$\nabla^2\phi = \frac{4\pi ne}{\epsilon}, \tag{4.3}$$

$$\frac{\partial n}{\partial t} + \nabla \cdot (n\vec{v}) = 0. \tag{4.4}$$

In Eq. (4.1), V is the externally imposed potential and p is the pressure of the electron gas. V is the quadratic potential profile of the conduction band: $V = \frac{1}{2}\mathcal{K}z^2 \equiv \frac{1}{2}m^*\Omega^2 z^2$. One often assumes a linear relationship between the pressure and density in hydrodynamic study of collective excitations in inhomogeneous electron systems. Thus, pressure, p is defined in terms of density,

$$\delta p = m^* s^2 \delta n. \tag{4.5}$$

The parameter s is taken to be $\sqrt{\frac{3}{5}}v_f$ where v_f is the Fermi velocity for a uniform electron gas with the design density $\overline{n} \equiv \frac{\epsilon\mathcal{K}}{4\pi e^2}$ of the parabolic well. Integrating Eq. (4.5), we have the functional form of pressure,

$$p = m^* s^2 (n - n_c). \tag{4.6}$$

In Eq. (4.6), we have introduced n_c as an integration constant. It is at the critical density where the pressure vanishes.

4.1.1 Equilibrium

It is clear that Eqs. (4.1)-(4.4) are coupled non-linear equations and that there are no analytical solution available. The approach to solving this type of problem is to assume that the the possible excited modes of the well can be described by density (n) fluctuation, velocity ($\vec{v}$) fluctuation, and field and potential ($\vec{E}$, $\vec{B}$ and ϕ) fluctuations around their equilibrium values. We can then solve the problem order by order. The simplest case is to linearize the equations by assuming $n = n_o + n_1$, $\vec{E} = \vec{E_o} + \vec{E_1}$, $\vec{B} = \vec{B_o} + \vec{B_1}$, $\vec{v} = \vec{v_o} + \vec{v_1}$, and $\phi = \phi_o + \phi_1$. Now, we must equate the terms of the same order and ignore all terms with higher than first order. When the electron gas is in equilibrium in the well, all forces on each unit volume of the electron gas vanish. As a result, we can assume that $\vec{v_o} = 0$. Since we are interested in only longitudinal plasma modes, we can also assume that $\vec{B_o}$ is due entirely to externally imposed dc magnetic fields, and $\vec{B_1} = 0$ in the first-order approximation. Thus, the zeroth-order

equation is [7]:

$$\frac{4\pi e^2}{\epsilon} n_o(z) - m^* \Omega^2 - m^* s^2 \partial_z^2 \ln n_o(z) = 0. \tag{4.7}$$

We must solve Eq. (4.7) subject to the appropriate boundary condition. The boundary condition in this case is set by the value of n_c. For n_c greater than zero, it means that that there is a position where the pressure vanishes. This determines the width of the electron slab. If we define the width of the electron slab to be $2a$, then $n_o(\pm a) = n_c$. That is, the pressure of the electron slab vanishes at the boundary. Thus, we see that the value of n_c and Eq. (4.7) determines the equilibrium properties of the electron gas. It turns out that only when $n_c = \overline{n_o}$ is the problem easily soluble. [7] This is the value of n_c we will use for our calculations. For this choice of n_c, the equilibrium density, $n_o(z)$ becomes extremely simple: it is $\overline{n_o}$ inside the electron slab and zero outside of the slab. This will appear to be a quite drastic simplification, especially for our sample, which is overfilled. Due to the high density of electron of the sample in our experiment when illuminated, the electrons have actually started to accumulate around the edges–it cannot have the constant value of $\overline{n_o}$ inside the well. However, we can take this simple model to be a reasonable approximation, as the deviation is not extreme in our case.

4.1.2 Linearized Problem

The first-order equations derived from Eq. (4.1) - (4.4) inside the well, where $n_o(z)$ is finite are:

$$\frac{\partial \vec{v}}{\partial t} = -\frac{e\vec{E}_1}{m^*} + \frac{e\vec{B}_o}{m^* c} \times \vec{v} - s^2 \nabla \frac{n_1}{n_o}, \tag{4.8}$$

$$\nabla^2 \phi_1 = \frac{4\pi e n_1}{\epsilon}, \tag{4.9}$$

$$\vec{E}_1 = -\nabla \phi_1, \tag{4.10}$$

$$\frac{\partial n_1}{\partial t} + \nabla \cdot (n_o \vec{v}) = 0. \tag{4.11}$$

Outside of the electron slab where $n_o(z)$ is zero, there is only one equation left in the linearized problem,

$$\nabla^2 \phi_1 = 0. \tag{4.12}$$

We now assume the various first-order quantities to have the functional form of

$$f_1(\vec{r}, t) = f_1(z) exp(i\vec{q} \cdot \vec{\rho} - i\omega t). \tag{4.13}$$

In Eq. (4.13), $\vec{\rho}$ is the in-plane coordinate, $\hbar\omega$ is the energy of the plasma mode, and $\vec{q}$ is the wave vector of the plasma mode. By substituting Eq. (4.13) into Eqs. (4.8) - (4.12) and imposing the appropriate boundary conditions, we can arrive at the energy dispersion for the plasma modes associated with the fluctuations.

The boundary conditions to be used to solve the problem depend on the filling of the quantum well by the remotely-doped electrons. The electron slab width is determined by the areal density of the electrons in the well , n_s, and the design density , $\overline{n_o}$: $2a = \frac{n_s}{n_o}$. When the electron slab width ,$2a$, is smaller than the actual well width, the electrons will not feel the abrupt conduction-band edge change at the actual well edge. The appropriate boundary conditions to use under this condition is the parabolic well boundary conditions: continuity of ϕ, and $\nabla \cdot v(\vec{r}, t) = 0$ at $z = \pm a$. In addition, since $v_z(\pm a) \neq 0$, there is a transfer of charge across the boundary of the electron slab. In the linearized problem, this can be treated as a delta function surface charge density at $z = \pm a$ with the surface charge density of $\mp \frac{n_c v_z(\pm a}{i\omega}$. The surface charge density leads to the final boundary condition on the discontinuity of the normal component of the electric field: $\delta E_z(\pm a) = \mp \frac{4\pi e}{i\omega\epsilon} n_c v_z(\pm a)$. On the other hand, if the areal electron density divided the well width is greater than the design density, then the correct boundary condition to use is the hard wall boundary condition: continuity of ϕ and E_z at $z = \pm a$, and $v_z(\pm a) = 0$.

By solving Eq.(4.8)-(4.11) subject to the appropriate boundary conditions, we find that there are two sets of magnetoplasma modes. The two sets of modes are distinct when the cyclotron energy is less than the bare harmonic energy: one set is associated with IL transition, while the other is associated with IS transition. When

the cyclotron energy is greater than the bare harmonic energy, the two sets of modes tend to couple to each other when they are close in energy. Thus, the distinction is clear only for the modes with large energy differences. In the case of parabolic boundary condition, there is always one mode at the bare harmonic energy when the in-plane wave vector, q, is zero. This mode is the mode which satisfies Kohn's theorem. It is the so-called center-of-mass mode, because this is the mode which involves the displacement of the slab as a whole in the z direction. It does not involve the relative coordinate between the electrons. Since electron-electron interactions involve only relative coordinates between the electrons, the energy of the center-of-mass mode cannot be affected. The displacement of the slab in the z direction creates delta function density fluctuation at the edges of the electron slab. It is clear that the crucial condition required for this mode is that the electron slab be allowed to move freely in the z direction. This is impossible under the hard-wall boundary condition. By definition, the electrons must have zero velocity in the z direction at the edges. Thus, the center-of-mass mode is absent under the hard-wall boundary condition. All IS magnetoplasma modes involve bulk density fluctuation when $q = 0$ under the hard wall boundary condition.

In the absence of the center-of-mass mode, one might ask if there is anything that can guide us to a reasonable answers. That is, are there some physical arguments that might allow estimates of what we should expect. Fortunately, we can look to the 3D plasma for guidance. When the in-plane wave vector, q, is zero, the eigenfunction of Eqs. (4.8)-(4.11) are of the form

$$\phi_1(z) \propto cos(q_z^k z), k = 1, 3, 5, \ldots \tag{4.14}$$

$$\phi_1(z) \propto sin(q_z^k z), k = 2, 4, 6 \ldots . \tag{4.15}$$

In order to satisfy the boundary conditions, we must require that q_z^k has the one of the quantized values of $\frac{k\pi}{2a}$, where k can be any positive integer value. It should be noted that the $k = 0$ case requires special consideration. When $k = 0$, the electrostatic potential eigenfunction inside of the well is $\phi_1(z) = 1 + \frac{z}{a}$. This particular

eigenfunction can satisfy only the parabolic boundary condition. It is the center-of-mass mode.

In the parabolic wells, we can consider the systems as being quasi-3D. When the in-plane wave vector, q, is zero, we see that the effective z-component of the 3D wave vector, q_z, must have the quantized values of $\frac{k\pi}{2a}$. Since the energy dispersion of plasmon in 3D increases quadratically near the zone center, we expect that the plasma modes in our system to have energy values equal to or greater than the bare harmonic energy. The mode with energy equal to the bare harmonic energy has the effective wave vector, κ, equals zero. This is the center-of-mass mode. The other modes have $\kappa = \frac{k\pi}{2a}$. Thus, the energy at $q = 0$ is expected to increase quadratically as mode index increases.

4.2 Experiment

4.2.1 Sample

Parabolic quantum wells are created by tailoring the energy band gap in semiconductor layers. A schematic diagram of a typical parabolic quantum well is shown in Fig. (4-1). The donors are set back a few hundred Åfrom the well. The advantage of remote doping is that it separates the positive donor ions from the electrons so that scattering between electrons and donors ions is minimized. This is the mechanism by which an ultra high mobility is achieved. The grading of the energy gap in $Al_xGa_{1-x}As$ is achieved by controlling the mole fraction of Al. There exists a linear relationship between the energy band gap of $Al_xGa_{1-x}As$ and Al mole fraction x for $x \leq 0.45$.[1] Thus, by controlling the variation of x, one controls the the variation of the alloy band gap of $Al_xGa_{1-x}As$. There are two ways of creating a parabolic profile of the Al mole fraction: analog alloy and digital alloy. In the case of analog alloy technique, one tries to vary the the Al flux in a controlled manner while keeping the fluxes of Ga and As constant. The Al flux is controlled by controlling the temperature of the Al oven in the molecular beam epitaxy (MBE) machine. By varying the temperature

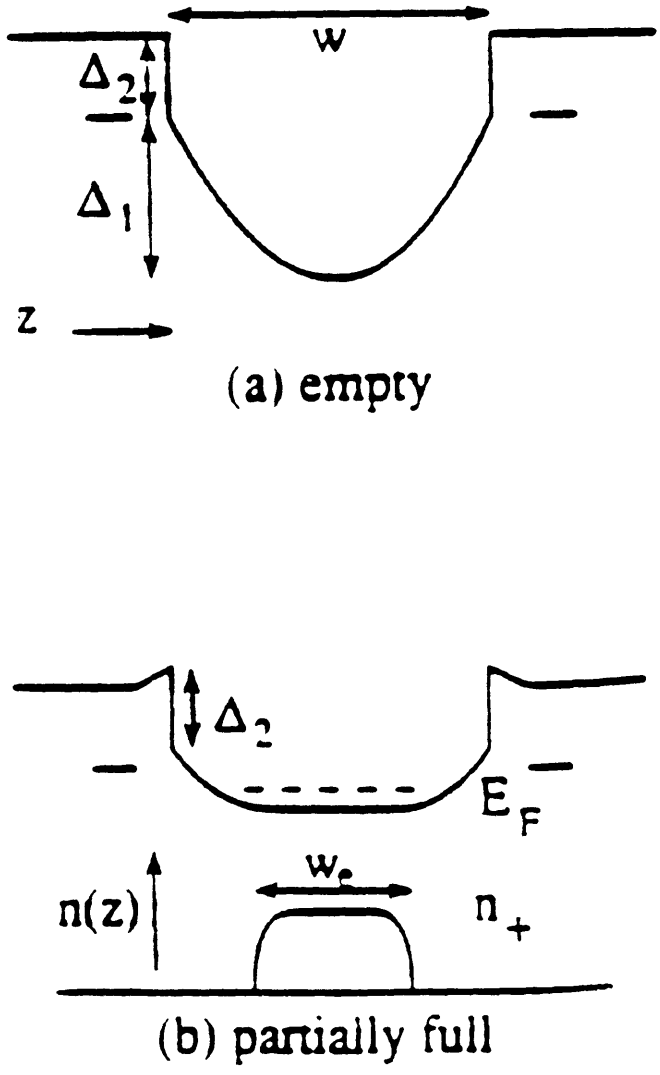

Figure 4-1: Schematic diagram of the potential profile of the parabolic quantum well.

of the Al oven as a function of time in the presence of constant Ga and As fluxes, one can create the desired Al mole fraction profile.[12] Alternatively, one can achieve the desired Al mole fraction profile by the digital alloy technique. A schematic diagram of a sample grown with digital alloy technique is shown in Fig. 4-2. In this case, one grows a superlattice with a constant period, l_z. Each period in the superlattice has two layers: GaAs and $Al_{xmax}Ga_{1-xmax}As$. The value of $xmax$ is the maximum value of the Al mole fraction desired. The usual value for $xmax$ is 0.3. The thickness of the $Al_{xmax}Ga_{1-xmax}As$ layer is varied in such a fashion that the average Al mole fraction has the desired parabolic profile. In this way, the average conduction-band edge imposes the desired parabolic confinement potential. This is not exactly the same as the continuous parabolic potential usually assumed in theoretical calculations. There is some evidence that the superlattice structure may cause some variation in the IS single particle transition energies. The evidence suggests that the IS single particle transition energies in these wells is dependent on the states involved in the transition, in contrast to the ideal parabolic potential where all transitions have the same transition energy.[24]

Samples are often grown so that the well has an abrupt change in the conduction-band edge at the physical edge of the well. The hard wall edge is usually not relevant to the energy structure of the well as long the electron slab width is less than the physical width. As long as the electron slab width, $2a$, is less than the actual well width L, the electron wave function will not have appreciable magnitude near the abrupt potential change. Hence the effect of the abrupt conduction-band edge will have little effect on the energy structure. On the other hand, if $n_s > \overline{n_o}L$, then the electrons will have appreciable wave function amplitude at the abrupt potential edge. As a result, the well will no longer be a good approximation of a truly parabolic well. In this case, the appropriate boundary conditions to use is the hard wall boundary condition.

The sample used in this work was grown by Hopkins and Gossard at UCSB with a width of 760 Å, mobility of 0.72×10^5 cm^2/Vs, and electron areal density of 8×10^{11} cm^{-2} (4.8×10^{11} cm^{-2} without illumination). We note that the well is overfilled

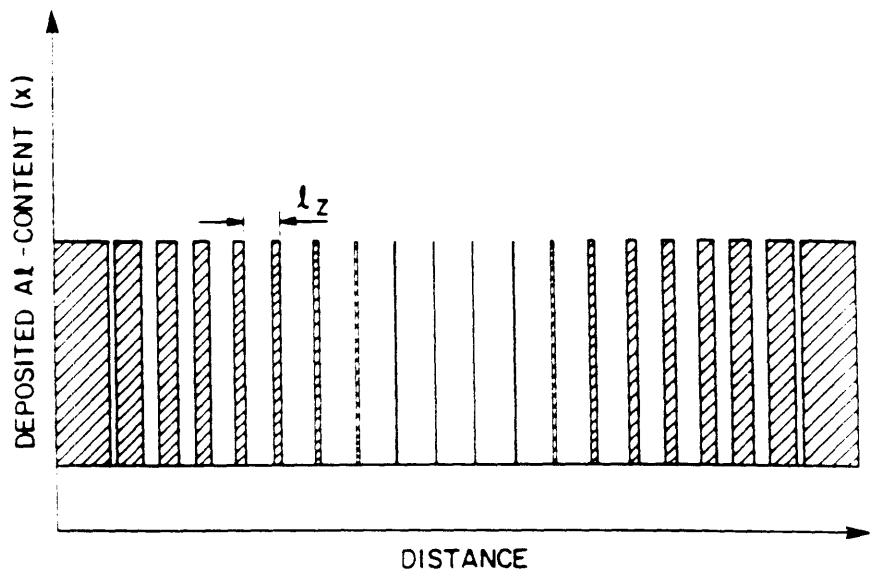

Figure 4-2: Schematic diagram of the superlattice structure of the parabolic quantum well. The shaded layers are made of $Al_{0.3}Ga_{0.7}As$ while the white region is made of GaAs.

because the electron areal density is greater than the design 3D density multiplied by the well width (5.6×10^{11} cm^{-2}). The composition inside the well alternates between GaAs and $Al_{0.3}Ga_{0.7}As$ in a 20$\AA$ superlattice. The average Al mole fraction is smoothly varied such that the conduction band edge has the desired parabolic profile with the bare harmonic energy of 10.6 meV.

4.2.2 Raman Scattering

Raman scattering experiments were carried out with either the two-fiber optical fiber probe or the optical dewar. The experiments were conducted at the temperature of 1.6 K. The excitation source was a cw dye laser. The laser is tuned so that it is near the electronic energy levels of the system. In this way, we take advantage of the resonant denominator in the Raman transition matrix element. The detector used to detect the scattered light is a CCD camera. It is crucial to use a CCD camera because of low signal from the scattered light ($\leq 5cps$), and the low noise level of the CCD camera allows for long integration times to acquire good signal to noise ratio.

4.2.3 Results

We observe two peaks in our spectra for most magnetic field values greater than 4 T. A typical set of spectra at $B = 5$ T is shown in Fig. 4-3. The lower-energy peak near the cyclotron energy is very narrow (0.3 meV) and the higher-energy peak near the bare harmonic energy is broad (1.0 meV). Figure 4-4 shows the behavior of the two peaks in magnetic fields. If the perpendicular magnetic field is varied, the narrow peak scales linearly with the magnetic field in the same fashion as the cyclotron energy. This is identified as the IL magnetoplasmon. The broad peak, on the other hand is nearly independent of the applied perpendicular magnetic field. It has an energy of 10.8 meV which is what one would expect from the hydrodynamics for an IS magnetoplasmon. Thus, it is identified as the IS magnetoplasmon. The puzzling effect occurs near the crossover of the cyclotron energy with the bare harmonic energy. After the crossover, the IS magnetoplasmon shifts abruptly to lower energy by $\sim$0.6

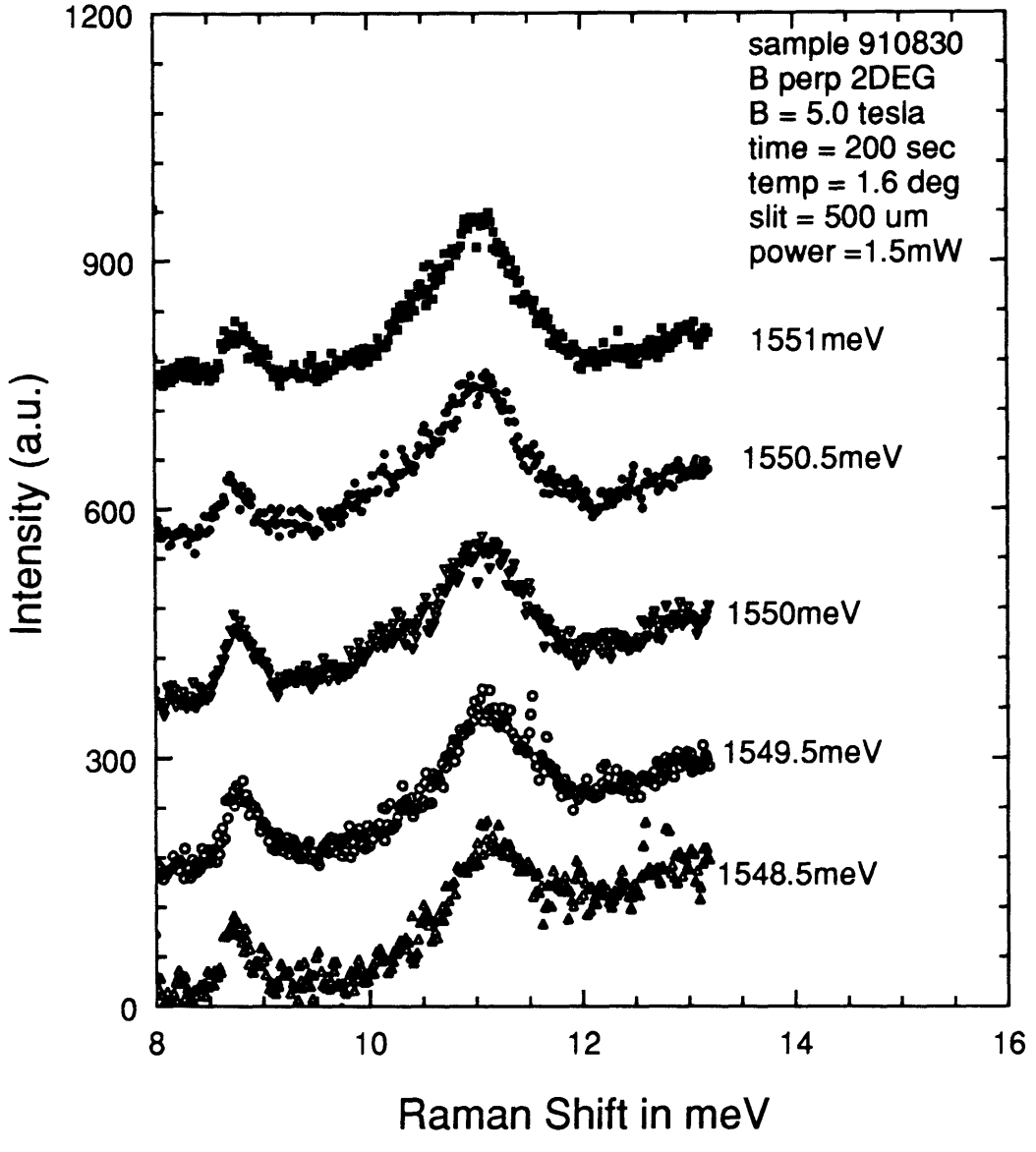

Figure 4-3: Typical inelastic light scattering spectra from GaAs/$Al_xGa_{1-x}As$ parabolic quantum well. Representative spectra for $qa = 0.05$ at B=5 T, where $a = 380\mathring{A}$ is half the well width and q is the in-plane wave vector. The spectra are labeled by the exciting laser energy. The temperature for the experiment was 1.6 K.

meV. This can be seen clearly in Fig. 4-4. If we examine the spectra from 7 T (just after the crossover) and 7.5 T, we see that though both spectra have the same low energy onset, the spectrum from 7 T has an higher energy shoulder which is not present at 7.5 T. The position of the shoulder is where the IS magnetoplasmon peak was before the crossover. This suggests that the apparent shift in energy is a shift in oscillator strength between two different IS magnetoplasma modes and that both modes are observable near the crossover at 7 T. Before the crossover, we can observe only the higher-energy IS magnetoplasma mode while after the crossover, only the lower-energy IS magnetoplasmon is observable. In addition to the study of the dependence of energy on magnetic fields, it is useful to study the energy dispersion (the dependence of energy on the wave vector) of the modes. The dispersion will help to identify the two IS magnetoplasma modes. The spectra in Figs. 4-3 and 4-4 are taken with very small in-plane wave vector, $qa = 0.05$. We can increase the in-plane wave vector to $qa = 0.21$ by increasing the incident photon angle. Figure 4-5 shows the spectra from various magnetic fields with the bigger in-plane wave vector. We can see similar, but more dramatic, behavior in Fig. 4-5 as in Fig. 4-4. Before the crossover, only the higher-energy magnetoplasmon is observed while after the crossover only the lower-energy magnetoplasmon is observed. Near the crossover, at 7 T, we can now confidently fit three peaks to the feature in the spectra: two IS magnetoplasmons and one IL magnetoplasmon. The energy separation between the two IS magnetoplasma modes is roughly 1.2 meV.

4.2.4 Discussion

The fact that the separation between the two IS magnetoplasma modes increases with the in-plane wave vector suggests that they are the two lowest-energy odd-symmetry density oscillation modes. The lowest-energy odd-symmetry mode is a surface-like mode and it has a sharp negative dispersion near $q = 0$. All higher energy modes are bulk-like and they have only very slight dispersion. Before the crossover, the bulk-like IS modes have small positive dispersion while after the crossover they have small negative dispersion. In both cases, the energy spacings between the bulk-like modes

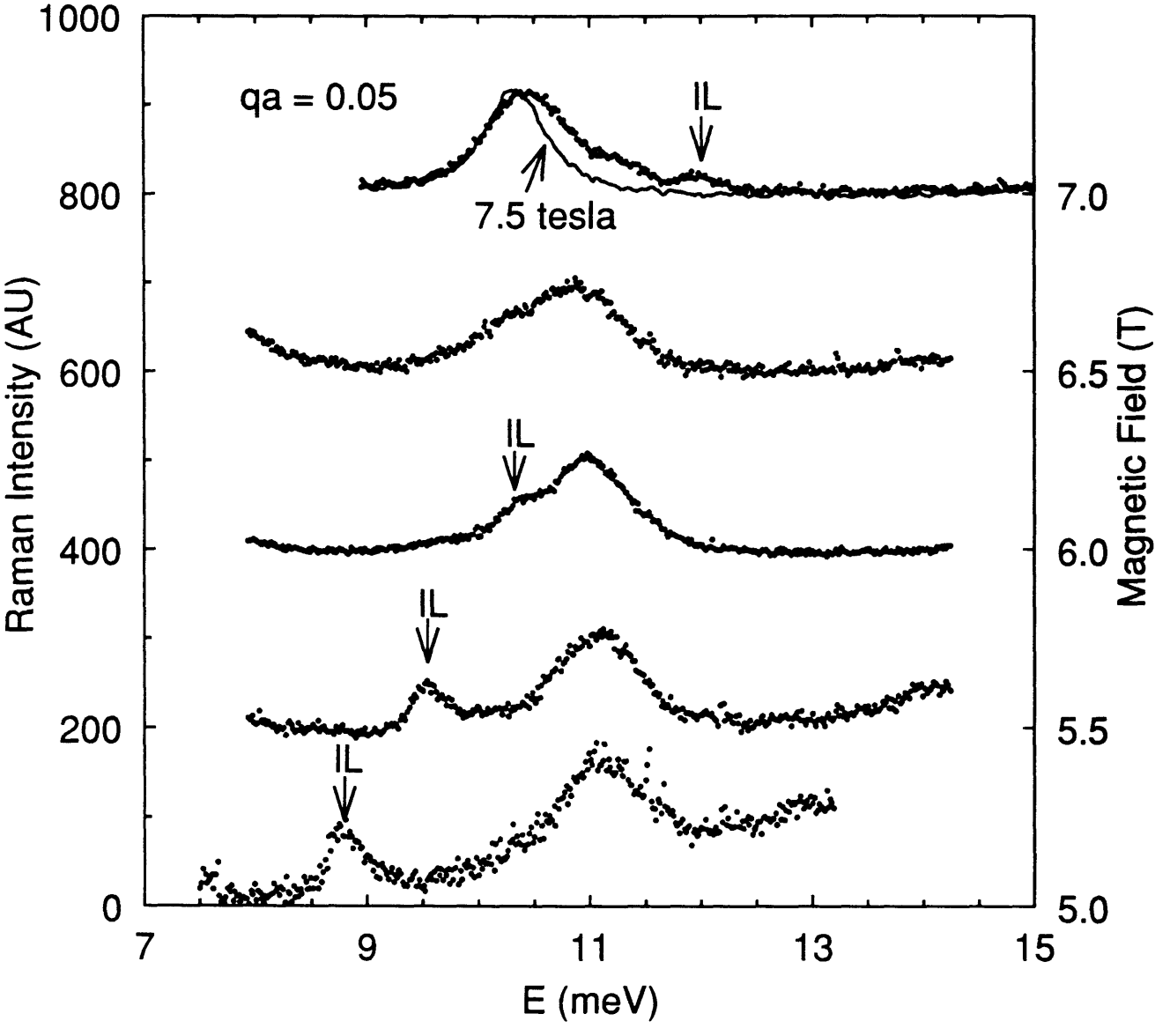

Figure 4-4: Inelastic light scattering spectra from a wide GaAs/$Al_xGa_{1-x}As$ parabolic quantum well. Representative spectra (normalized) for $qa = 0.05$ at various perpendicular magnetic fields, where $a = 380\mathring{A}$ is half the well width and q is the in-plane wave vector. The spectra were taken with laser energy near 1550 meV and temperature of 1.6 K. The laser energy was varied slightly at the different magnetic fields.

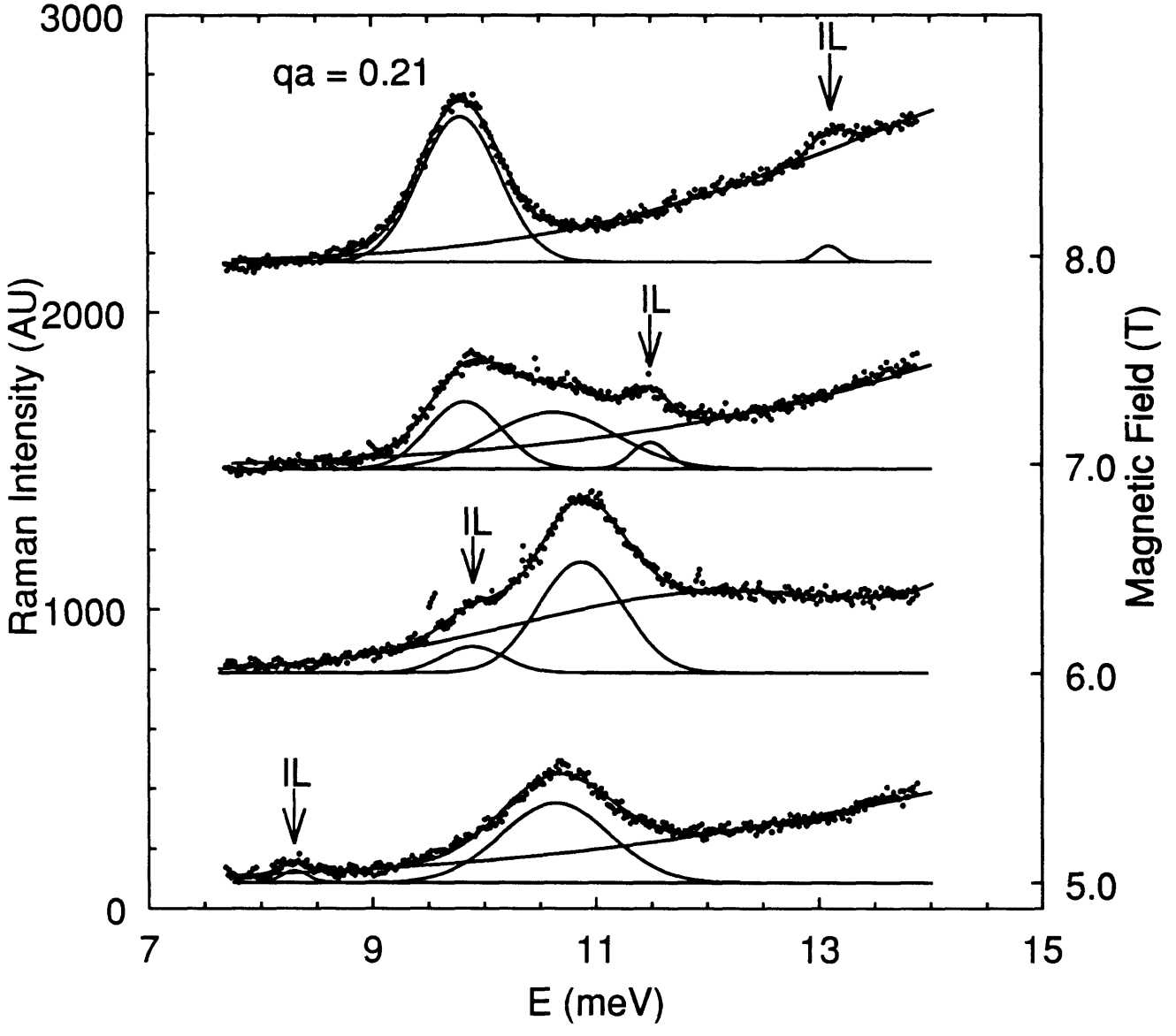

Figure 4-5: Inelastic light scattering spectra from a wide GaAs/$Al_xGa_{1-x}As$ parabolic quantum well. Representative unnormalized spectra for $qa = 0.21$ at various magnetic fields. The laser is set at 1550 meV. The solid curves are Gaussian line-shape fits to the experimental spectra, including a substantial background due to photoluminescence.

are nearly constant for small wave vectors. The surface-like mode, on the other hand, has a very sharp negative dispersion. The energy separations between the surface-like mode and the bulk-like modes are expected to be a rapidly increasing function of the wave vector, q. Figure 4-6 shows the theoretical calculation (solid curves) of the odd-symmetry magnetoplasma modes and the experimental points for $qa = 0.05$ while Fig. 4-7 shows the results for $qa = 0.21$. We see that the spacings for the bulk-like modes increases quadratically with the increasing mode index. Comparing the solid curves from Fig. 4-6 and Fig. 4-7, it is clear that the energy separations between the bulk-like modes are nearly independent of the value of qa. On the other hand, the energy separations between the bulk-like modes and the surface-like mode are sensitive to the small change in qa. In Fig. 4-8, the dispersion curves of the two lowest odd IS magnetoplasmons and data points are shown for three different magnetic field values. The calculated energy separation between the two IS magnetoplasmon modes increases with the in-plane wave vector consistent with the experimental points.

In addition to the behavior of the IS magnetoplasmons, the behavior of the IL magnetoplasmon is also interesting. In Fig. 4-6 the IL magnetoplasmon follows the the cyclotron energy closely while in Fig. 4-7 it tends to fall below the cyclotron energy. Before the crossover with the IS magnetoplasmon mode, the IL magnetoplasmon has negative dispersion. This is contrary to the usual behavior of the IL surface magnetoplasmon. It is identified as a bulk-like IL magnetoplasmon. At very high magnetic field after crossover, the energy of the IL magnetoplasmon deviates from the calculated curves. This is due to the anticrossing behavior between the IL magneoplasmons and IS magnetoplasmons. Usually, the IL magnetoplasmon is not a dipole allowed Raman transition. We speculate that the IL magnetoplasmon is observed only when it has acquired enough hybrid IS characteristics. Since the coupling between the IS and IL magnetoplasmons increases with q, the bigger in-plane wave vector implies stronger anticrossing behavior. At present, we do not have a model to explain the mechanism involved in the shift in the oscillator strength between the IS magnetoplasma modes.

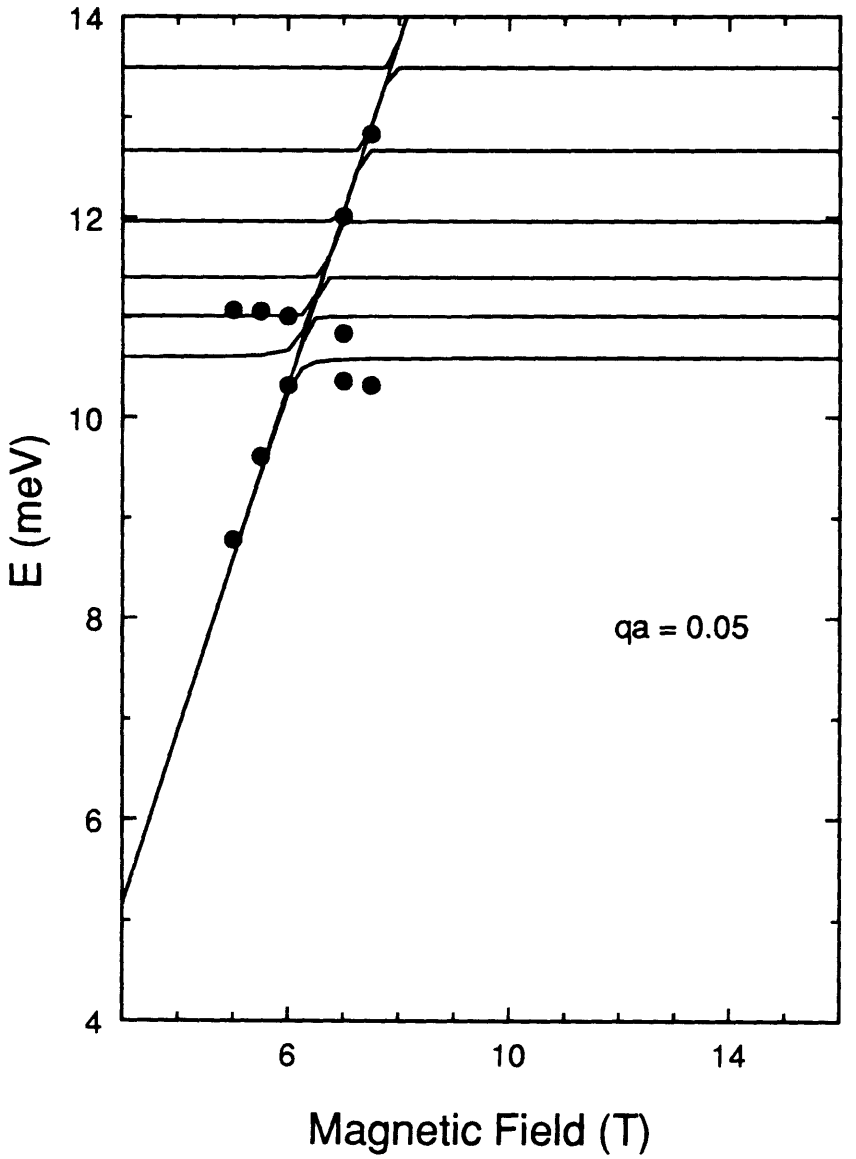

Figure 4-6: The solid curves represent the calculated odd-symmetry density oscillation modes of a wide parabolic quantum well in the hydrodynamic model with hard-wall boundary conditions. We used 10.8 meV as the value of the bare harmonic energy, and $qa = 0.05$.

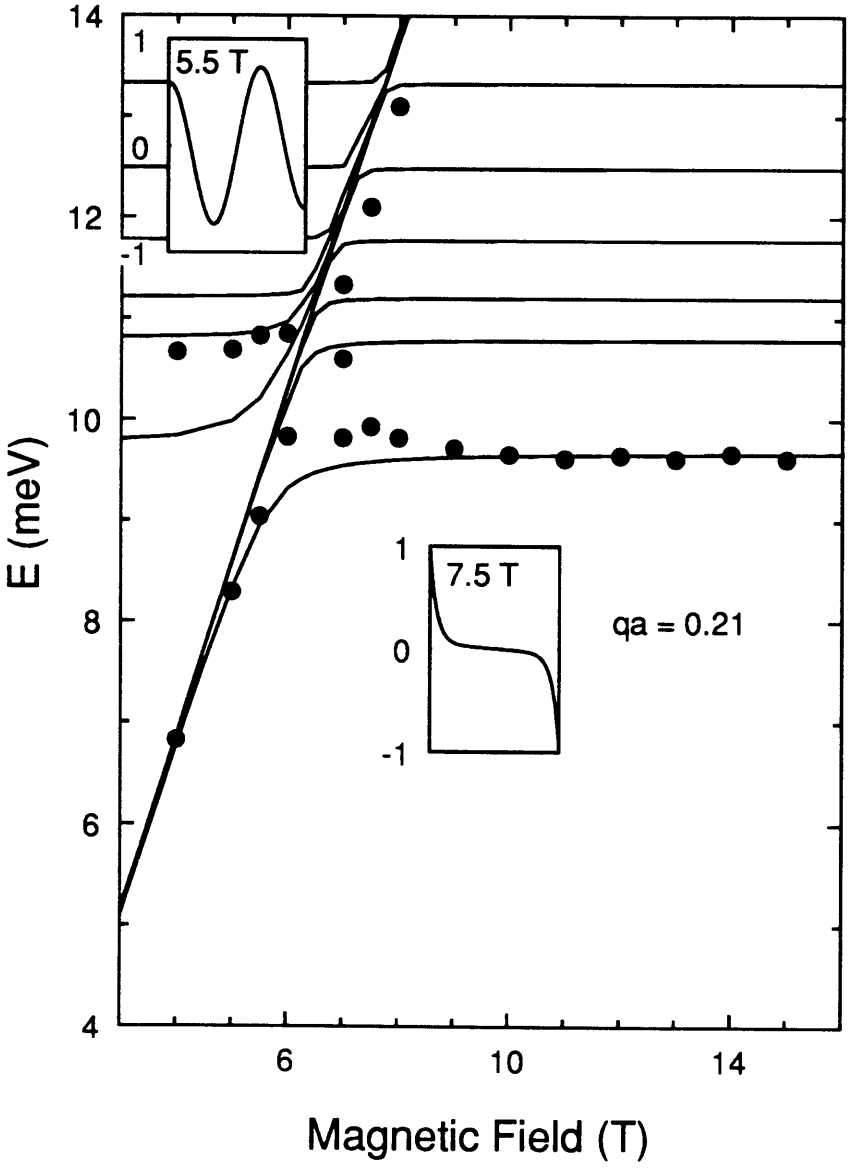

Figure 4-7: The solid curves represent the calculated odd-symmetry density oscillation modes of a wide parabolic quantum well in the hydrodynamic model with hard-wall boundary conditions. We used 10.6 meV as the value of the bare harmonic energy and $qa = 0.21$. The insets are the normalized density fluctuations inside the well for the odd-symmetry modes at low fields (left hand side) and high fields (right hand side).

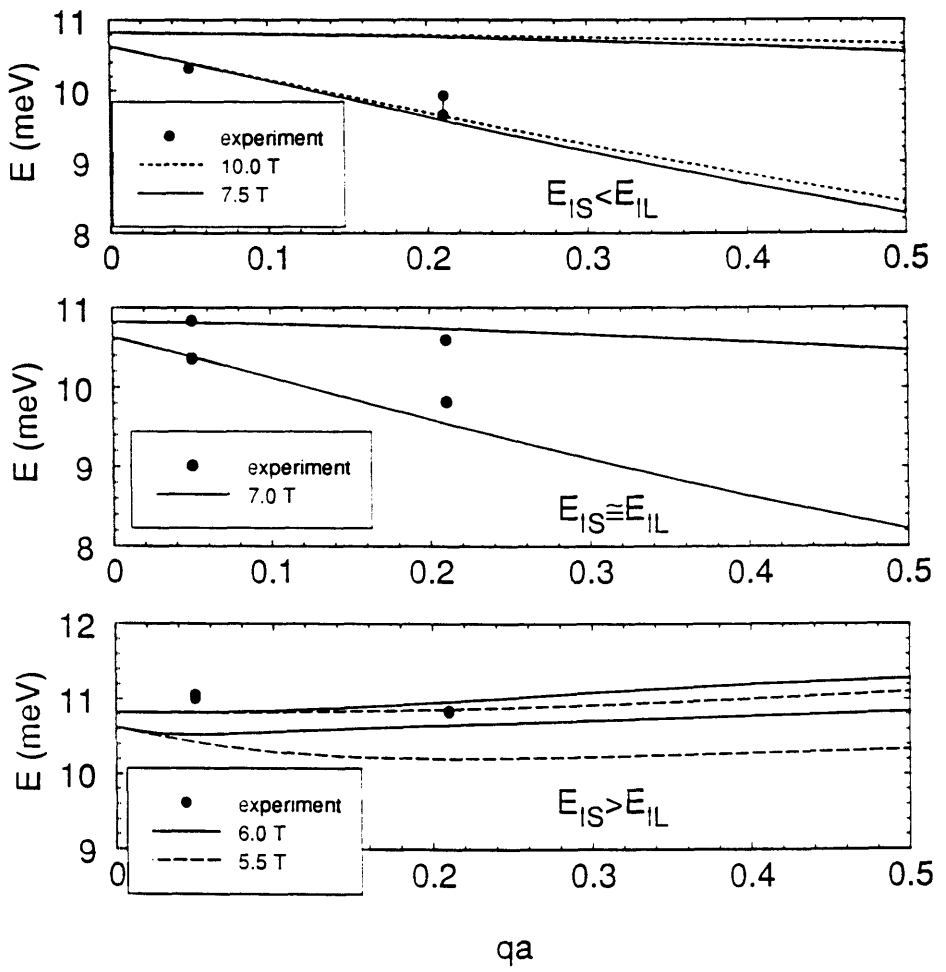

Figure 4-8: Theoretical wave vector dispersion curves and experimental points for the lowest two odd-symmetry intersubband plasma modes at various magnetic fields.

Chapter 5

Conclusions

The high mobilities achievable in GaAs/$Al_xGa_{1-x}As$ modulation-doped quantum wells make them ideal for use as extremely fast ($\sim 10^{-12}$ sec) and low-power transistors. In addition to desirable electrical properties, direct optical transitions in GaAs/$Al_xGa_{1-x}As$ quantum wells either between different confinement subband states or between conduction band and valence band makes these systems ideal for fabricating optical devices. Eventually, it would be desirable to integrate an entire electro-optical system on a single chip of GaAs/$Al_xGa_{1-x}As$. In order to optimize the design of such electro-optical systems, it is essential to understand both the transport and optical properties of GaAs/$Al_xGa_{1-x}As$ quantum wells. In this thesis, I have studied the optical properties of these systems both theoretically and experimentally.

Two types of systems were studied using resonant Raman scattering: the single quantum well made from two abrupt junctions of GaAs/$Al_{0.3}Ga_{0.7}As$, and the parabolic quantum well made from graded $Al_xGa_{1-x}As$. For the single quantum well samples, the wells are asymmetrically doped on one side, while the parabolic quantum well is symmetrically doped. The experimental data revealed that in two dimensional systems, it is important to take into account many-body interactions. It is observed (either through IS magnetoplasmon or through the hybrid of IL and IS plasmon) that confinement subband energy levels can not be accounted for with simple static calculations. The confinement subband energy levels are important in applications to optical devices. For example, one might want to have the transition energy between

subbands to be in resonance with the signal for an optical detector or one might want to have some desired energy separation for laser applications. A review of the literature reveals that the energy levels measured by transport measurements can be calculated with simple static (Hartree and exchange energy terms) calculations. The experimental data acquired as part of this thesis reveal that the static calculations are insufficient for spectroscopic measurements. The energy levels as measured with inelastic light-scattering are very different from the levels measured with transport measurements. This is because that while the transport measurements measure the cost of creating a quasi-hole and quasi-electron pair ($\vec{k} \rightarrow \infty$), the optical measurement measure the energy of collective modes of the electrons ($\vec{k} \rightarrow 0$).

The experimental part of the thesis measured charge-density excitation energy and spin-density excitation energy. In the single quantum well experiments, the samples were subjected to magnetic fields not normal to the 2DEG plane. The in-plane component of the magnetic field couples the IL and IS transition and allows for the study of the effect of the electronic wave function in the confinement direction. In the wide parabolic quantum well experiments, the IL and IS magnetoplasmons were studied in detail. In order to understand the physics and develop predictive models, I developed a time-dependent Hartree-Fock model for the single quantum wells and a hydrodynamic model for the wide parabolic quantum well. The models agree quantitatively with the experimental data only when the electron-electron interactions are included self-consistently. I found that while electrostatic interactions between the electrons (Hartree potential) reduce the energy separations between subband states, the time-dependent Hartree potential (RPA) always compensate for the Hartree potential. For the wide parabolic quantum wells, in particular, the two terms cancel exactly.

In the thesis, I have presented quantitative models which agree with the experimental data in the study of collective modes of 2DEG. It is hoped that since the models quantify the behavior of electrons in 2DEG systems, they will be useful for future device design.

Appendix A

Coulomb Correction

From section 2.1.2, we found that the expectation value of the Hamiltonian in the many-body charge density or spin density excited states is

$$\langle \Psi'_\sigma | H | \Psi_\sigma \rangle = (E_g + \hbar\Omega_\sigma)\delta_{\sigma,\sigma'} + \mathcal{C}^*\mathcal{C}\langle \Psi_g | \rho^\dagger_{\sigma'} \left[V_{e-e}(\vec{r_i}, \vec{r_j}), \rho_\sigma \right] | \Psi_g \rangle. \tag{A.1}$$

The term E_g in the Eq. (A.1) is the ground state energy and $\hbar\Omega_\sigma$ is the single particle energy. The last term in Eq. (A.1) is the correction to the single particle energy from the many-body interaction of electrons. We will define this energy to be $E(\vec{k}, \sigma', \sigma)$. The purpose of this appendix is to relate $E(\vec{k}, \sigma', \sigma)$ to the matrix elements $F(n_+, n_-; m_+, m_- : \vec{q})$.

In order to write the coulomb correction to the single particle energy in terms of $F(n_+, n_-; m_+, m_- : \vec{q})$, we need to write the commutator in Eq. (A.1) in terms of the density operator $e^{i\vec{q}\cdot\vec{r}}$. This can be achieve easily by simply substituting Eq. (2.21) into the commutator in Eq. (A.1). The commutator becomes

$$\begin{aligned}
\left[V_{e-e}(\vec{r_i}, \vec{r_j}), \rho_\sigma \right] &= \int \frac{d^3q}{(2\pi)^3} \frac{2\pi e^2}{\epsilon q^2} \sum_{i \neq j} \sum_l \left[e^{i\vec{q}\cdot(\vec{r_i} - \vec{r_j})}, |n_\sigma, n_{-\sigma} = 0, s\rangle_{l\ l}\langle n_\pm = 0, s| \delta_l B_l(k_\perp) \right], \\
&= \int \frac{d^3q}{(2\pi)^3} \frac{2\pi e^2}{\epsilon q^2} \sum_{i \neq j} \sum_l \\
&\quad \left\{ e^{i\vec{q}\cdot\vec{r_i}} \left[e^{-i\vec{q}\cdot\vec{r_j}}, |n_\sigma, n_{-\sigma} = 0, s\rangle_{l\ l}\langle n_\pm = 0, s| \delta_l B_l(k\ \perp) \right] + \right.
\end{aligned}$$

$$\left[e^{i\vec{q}\cdot\vec{r_i}}, |n_\sigma, n_{-\sigma}=0,s\rangle_{l\ l}\langle n_\pm=0,s|\delta_l B_l(k_\perp)\right] e^{-i\vec{q}\cdot\vec{r_j}}\Big\}. \tag{A.2}$$

In Eq. (A.2), the commutators vanishes unless the indices in the commutator have the same value. Thus, the first commutator must satisfy $j = l$ and the second must satisfy $i = l$. In Eq. (A.2), we have written $B(k_\perp)$ instead of $B(k_\perp \ell_o)$. The natural length unit used is the magnetic length, ℓ_o. The natural energy unit is the Coulomb energy $\frac{e^2}{\epsilon \ell_o}$ where ϵ is the dielectric constant.

The correction to the single particle energy can now be written as

$$\begin{aligned} E(\vec{k},\sigma',\sigma) &= \mathcal{C}^*\mathcal{C}\int \frac{d^3q}{(2\pi)^3}\frac{2\pi}{q^2}\Bigg\{\sum_{i\neq l}\sum_j \langle\Psi_g|\delta_j B_j(-k_\perp)|n_\pm=0,s'\rangle_{j\ j}\langle n_{\sigma'}, n_{-\sigma'}=0,s'| \\ &\quad e^{i\vec{q}\cdot\vec{r_i}}\left[\ e^{-i\vec{q}\cdot\vec{r_l}}, |n_\sigma, n_{-\sigma}=0,s\rangle_{l\ l}\langle n_\pm=0,s|\delta_l B_l(k\perp)\right]|\Psi_g\rangle + \\ &\quad \langle\Psi_g|\delta_j B_j(-k_\perp)|n_\pm=0,s'\rangle_{j\ j}\langle n_{\sigma'}, n_{-\sigma'}=0,s'| \\ &\quad \left[\ e^{i\vec{q}\cdot\vec{r_l}}, |n_\sigma, n_{-\sigma}=0,s\rangle_{l\ l}\langle n_\pm=0,s|\delta_l B_l(k_\perp)\right]\ e^{-i\vec{q}\cdot\vec{r_i}}|\Psi_g\rangle\Bigg\}, \end{aligned} \tag{A.3}$$

where we have used the fact that $B^\dagger(k_\perp) = B(-k_\perp)$. We must keep in mind that Eq. (A.3) is already written in the length unit of ℓ_o and energy unit of $\frac{e^2}{\epsilon\ell_o}$. We can simplify Eq. (A.3) by making some variable transformations. Since $i \neq l$ in the summation, we can move the term $e^{-i\vec{q}\cdot\vec{r_i}}$ to the left of the commutator bracket. Next, we replace $\vec{q}$ by $-\vec{q}$. This does not change the result of the integration since we are integrating over the entire q space. Once we have made these transformations, the second term is exactly the same as the first term. Thus, $E(\vec{k},\sigma',\sigma)$ is just twice the first commutator in Eq. (A.3):

$$\begin{aligned} E(\vec{k},\sigma',\sigma) &= \mathcal{C}^*\mathcal{C}\int \frac{d^3q}{(2\pi)^3}\frac{4\pi}{q^2}\sum_{i\neq l}\sum_j \langle\Psi_g|\delta_j B_j(-k_\perp)|n_\pm=0,s'\rangle_{j\ j}\langle n_{\sigma'}, n_{-\sigma'}=0,s'| \\ &\quad e^{i\vec{q}\cdot\vec{r_i}}\left[\ e^{-i\vec{q}\cdot\vec{r_l}}, |n_\sigma, n_{-\sigma}=0,s\rangle_{l\ l}\langle n_\pm=0,s|\delta_l B_l(k_\perp)\right]|\Psi_g\rangle. \end{aligned} \tag{A.4}$$

In order to get a simplified expression for Eq. (A.4), we will write the terms as $E(\vec{k},\sigma',\sigma,p)$ where $E(\vec{k},\sigma',\sigma) = \mathcal{C}^*\mathcal{C}\left(E(\vec{k},\sigma',\sigma,1) - E(\vec{k},\sigma',\sigma,2)\right)$.

A.1 Evaluation of $E(\vec{k}, \sigma', \sigma, p)$

The first term we need to evaluate is

$$E(\vec{k},\sigma',\sigma,1) = \int \frac{d^3q}{(4\pi)^3}\frac{4\pi}{q^2}\sum_{i\neq l}\sum_j \langle\Psi_g|\delta_j B_j(-k_\perp)|n_\pm=0,s'\rangle_j\ {}_j\langle n_{\sigma'},n_{-\sigma'}=0,s'| \\ e^{i\vec{q}\cdot\vec{r}_i}\ e^{-i\vec{q}\cdot\vec{r}_l}|n_\sigma,n_{-\sigma}=0,s\rangle_l\ {}_l\langle n_\pm=0,s|\delta_l B_l(k_\perp)|\Psi_g\rangle. \quad (A.5)$$

Since ${}_j\langle n_{\sigma'},n_{-\sigma'}=0|e^{i\vec{q}\cdot\vec{r}_i}e^{-i\vec{q}\cdot\vec{r}_l}|n_\sigma,n_{-\sigma=0}\rangle_l$ vanishes unless $i=j$ or $l=j$, we have two contributions from $E(\vec{k},\sigma',\sigma,1)$. The first contribution comes from $i=j$:

$$E(\vec{k},\sigma',\sigma,1)_{i=j} = \int \frac{d^3q}{(2\pi)^3}\frac{4\pi}{q^2}\sum_{i\neq l}\langle\Psi_g|\delta_i B_i(-k_\perp)|n_\pm=0,s'\rangle_i\ {}_i\langle n_{\sigma'},n_{-\sigma'}=0,s'| \\ e^{i\vec{q}\cdot\vec{r}_i}\ e^{-i\vec{q}\cdot\vec{r}_l}|n_\sigma,n_{-\sigma}=0,s\rangle_l\ {}_l\langle n_\pm=0,s|\delta_l B_l(k_\perp)|\Psi_g\rangle. \quad (A.6)$$

We can replace $e^{i\vec{q}\cdot\vec{r}}$ by $e^{iq_z z}A(q_\perp)B(q_\perp)$ in Eq. (A.6)

$$E(\vec{k},\sigma',\sigma,1)_{i=j} = \int \frac{d^3q}{(2\pi)^3}\frac{4\pi}{q^2}\sum_{i\neq l}\langle\Psi_g|\delta_i B_i(-k_\perp)B_i(q_\perp)B_l(-q_\perp)\delta_l B_l(k\perp)|\Psi_g\rangle \\ \langle s_i|s_g\rangle\langle s_g|s_l\rangle F(n_{\sigma'},n_{-\sigma'}=0,0,0:\vec{q})F(0,0;n_\sigma,n_{-\sigma}=0:-\vec{q}). \quad (A.7)$$

In Eq. (A.7), s_g refers to the ground spin states of electrons labeled i and l. The other contribution comes from $l=j$:

$$E(\vec{k},\sigma',\sigma,1)_{l=j} = \int \frac{d^3q}{(2\pi)^3}\frac{4\pi}{q^2}\sum_{i\neq l}\langle\Psi_g|\delta_l B_l(-k_\perp)|n_\pm=0,s'\rangle_l\ {}_l\langle n_{\sigma'},n_{-\sigma'}=0,s'| \\ e^{i\vec{q}\cdot\vec{r}_i}\ e^{-i\vec{q}\cdot\vec{r}_l}|n_\sigma,n_{-\sigma}=0,s\rangle_l\ {}_l\langle n_\pm=0,s|\delta_l B_l(k\perp)|\Psi_g\rangle. \quad (A.8)$$

We again substitute in the definition of $e^{i\vec{q}\cdot\vec{r}}$. The $l=j$ term becomes

$$E(\vec{k},\sigma',\sigma,1)_{l=j} = \int \frac{d^3q}{(2\pi)^3}\frac{4\pi}{q^2}\sum_{i\neq l}\langle\Psi_g|\delta_l B_l(-k_\perp)B_i(q_\perp)B_l(-q_\perp)\delta_l B_l(k_\perp)|\Psi_g\rangle \\ \langle s_l|s_l\rangle F(n_{\sigma'},n_{-\sigma'}=0,n_\sigma,n_{-\sigma}=0:-\vec{q})F(0,0,0,0:\vec{q}).$$

(A.9)

The second term of the commutator is

$$E(\vec{k},\sigma',\sigma,2) = \int \frac{d^3q}{(2\pi)^3}\frac{4\pi}{q^2}\sum_{i\neq l}\sum_j \langle\Psi_g|\delta_j B_j(-k_\perp)|n_\pm=0\rangle_j\ {}_j\langle n_{\sigma'},n_{-\sigma'}=0|$$
$$e^{i\vec{q}\cdot\vec{r}_i}|n_\sigma,n_{-\sigma}=0\rangle_l\ {}_l\langle n_\pm=0|\delta_l B_l(k\perp)\ e^{-i\vec{q}\cdot\vec{r}_l}|\Psi_g\rangle. \quad \text{(A.10)}$$

The term ${}_j\langle n_{\sigma'},n_{-\sigma'}=0|\ e^{i\vec{q}\cdot\vec{r}_i}|n_\sigma,n_{-\sigma}=0\rangle_l$ in Eq. (A.10) vanishes unless $l=j$. Thus, there is only one contribution from $E(\vec{k},\sigma',\sigma,2)$:

$$E(\vec{k},\sigma',\sigma,2) = \int \frac{d^3q}{(2\pi)^3}\frac{4\pi}{q^2}\sum_{i\neq l}\langle\Psi_g|\delta_l B_l(-k_\perp)B_i(q_\perp)\delta_l B_l(k_\perp)B_l(q_\perp)|\Psi_g\rangle$$
$$\langle s_l\ |s_l\rangle F(0,0,0,0:\vec{q})F(0,0,0,0:-\vec{q})\delta_{\sigma,\sigma'}. \quad \text{(A.11)}$$

We have now reduced the problem to the calculation of the expectation value of intra-level operators between the ground states and $F(n_+,n_-;m_+,m_-:\vec{q})$.

A.2 Expectation Values of Intra-Level Operators

In order to evaluate the expectation values of the intra-level operators between the ground states in Eq. (A.7), Eq. (A.9), and Eq. (A.11), we need to know the properties of the operator $B(q_\perp)$. The definition of the operator $B(q_\perp)$ is

$$B(q_\perp) = e^{i\frac{q_\perp^* b}{\sqrt{2}}}\ e^{-i\frac{q_\perp b^\dagger}{\sqrt{2}}}. \quad \text{(A.12)}$$

In Eqs. (A.7), (A.9), and (A.11), the intra-level operators occur in the form of products. The product of two intra-level operators is

$$B(k_1)B(k_2) = e^{i\frac{k_1^* b}{\sqrt{2}}}\ e^{-i\frac{k_1 b^\dagger}{\sqrt{2}}}\ e^{i\frac{k_2^* b}{\sqrt{2}}}\ e^{-i\frac{k_2 b^\dagger}{\sqrt{2}}}. \quad \text{(A.13)}$$

Since the intra-level operator is an exponential operator, one would expect the product of two such operators might be related to the exponential of the sum of the exponents.

This would be the case if the exponents were complex numbers instead of operators. In our case, we need to invoke the Glauber's formula: if the commutator of two operators commutes with both operators, then the product of the exponential can be written as

$$e^a \ e^b = e^{a+b} e^{-[a,b]}. \tag{A.14}$$

If we apply Glauber's formula to Eq. (A.13) until we achieve the form of the exponential desired, it can be written as:

$$B(k_1)B(k_2) = B(k_1 + k_2) \ e^{\frac{k_1 k_2^*}{2}}. \tag{A.15}$$

Eqs. (A.7), (A.9), and (A.11) can now be written as

$$\begin{aligned} E(\vec{k}, \sigma', \sigma, 1)_{i=j} &= \int \frac{d^3q}{(2\pi)^3} \frac{4\pi}{q^2} \sum_{i \neq l} \langle \Psi_g | \delta_i \delta_l B_l(k_\perp - q_\perp) B_i(-(k_\perp - q_\perp)) | \Psi_g \rangle e^{-\frac{k_\perp q_\perp^* + k_\perp^* q_\perp}{2}} \\ &\quad \langle s_i \, | s_l \rangle F(n_{\sigma'}, n_{-\sigma'} = 0, 0, 0 : \vec{q}) F(0, 0; n_\sigma, n_{-\sigma} = 0 : -\vec{q}), \end{aligned} \tag{A.16}$$

$$\begin{aligned} E(\vec{k}, \sigma', \sigma, 1)_{l=j} &= \int \frac{d^3q}{(2\pi)^3} \frac{4\pi}{q^2} \sum_{i \neq l} \langle \Psi_g | |\delta_l|^2 B_l(-q_\perp) B_i(q_\perp) | \Psi_g \rangle e^{\frac{k_\perp q_\perp^* - k_\perp^* q_\perp}{2}} e^{-\frac{|k_\perp|^2}{2}} \\ &\quad \langle s_l \, | s_l \rangle F(n_{\sigma'}, n_{-\sigma'} = 0, n_\sigma, n_{-\sigma} = 0 : -\vec{q}) F(0, 0, 0, 0 : \vec{q}), \end{aligned} \tag{A.17}$$

and

$$\begin{aligned} E(\vec{k}, \sigma', \sigma, 2) &= \int \frac{d^3q}{(2\pi)^3} \frac{4\pi}{q^2} \sum_{i \neq l} \langle \Psi_g | |\delta_l|^2 B_i(-q_\perp) B_l(q_\perp) | \Psi_g \rangle e^{-\frac{|k_\perp|^2}{2}} \\ &\quad \langle s_l \, | s_l \rangle F(0, 0, 0, 0 : \vec{q}) F(0, 0, 0, 0 : -\vec{q}) \delta_{\sigma, \sigma'}. \end{aligned} \tag{A.18}$$

Expressions of the type $\langle \Psi_g | \sum_{i \neq j} \delta_i \delta_x B_i(k) B_j(-k) | \Psi_g \rangle$ where $x = i$ or $x = j$ in Eqs. (A.16), (A.17) and (A.18) are the correlation functions of the electrons in the ground state. They can be written as [3]

$$\begin{aligned} \sum_{i \neq j} \langle \Psi_g | B_i(k) B_j(-k) | \Psi_g \rangle &= \sum_{i,j} \langle i, j | B(k)_1 B_2(-k) | i, j \rangle - \\ &\quad \sum_{i,j} \langle i, j | B(k)_1 B_2(-k) | j, i \rangle_i \langle s \, | s \rangle_j \, _j \langle s' \, | s' \rangle_i, \end{aligned}$$

(A.19)

where B_1 acts on the index in position 1 and B_2 acts on the index in position 2. The first term is the direct interaction term while the second term is the exchange term. The spin part in the exchange term froces the spin of ith electron to line up with the jth electron. The exchange term can now be written as

$$-\sum_{i,j}\langle i,j|B_1(k)B_2(-k)|j,i\rangle(s_i \parallel s_j) = -\sum_{i,j}\langle i|B(k)|j\rangle\langle j|B(-k)|i\rangle(s_i \parallel s_j). \quad \text{(A.20)}$$

Since we are considering only filled levels, the sum over the particle indices is the same as the sum over the intra-level indices.

$$\begin{aligned} -\sum_{i,j}\langle i,j|B_1(k)B_2(-k)|j,i\rangle(s_i \parallel s_j) &= -\sum_{i}\langle i|B(k)B(-k)|i\rangle(s_i \parallel s_j) \\ &= -\sum_{i}\langle i\,|i\rangle\ e^{-\frac{|k|^2}{2}}(s_i \parallel s_j). \end{aligned} \quad \text{(A.21)}$$

In Eq. (A.21), $(s_i \parallel s_j)$ means that the spins of ith and jth electrons are aligned. In arriving at Eq. (A.21), we have used the closure relation, $\sum_j |j\rangle\langle j| \equiv 1$ and Eq. (A.15). The direct term can be written as

$$\sum_{i,j}\langle i,j|B(k)_1B_2(-k)|i,j\rangle = \sum_{i}\langle i|B(k)|i\rangle\sum_{j}\langle j|B(-k)|j\rangle. \quad \text{(A.22)}$$

When we substitute Eqs (A.21) and (A.22) into Eqs. (A.16), (A.17) and (A.18) become

$$\begin{aligned} E(\vec{k},\sigma',\sigma,1)_{i=j} &= \int\frac{d^3q}{(2\pi)^3}\frac{4\pi}{q^2}\left(\sum_i\delta_i\sum_l\delta_l\langle i|B(k_\perp-q_\perp)|i\rangle\langle l|B(-(k_\perp-q_\perp))|l\rangle - \right. \\ &\qquad \left.\sum_i e^{-\frac{|k_\perp-q_\perp|^2}{2}}\right)e^{-\frac{k_\perp q_\perp^* + k_\perp^* q_\perp}{2}} \\ &\qquad \langle s_i\,|s_l\rangle F(n_{\sigma'},n_{-\sigma'}=0,0,0:\vec{q})F(0,0;n_\sigma,n_{-\sigma}=0:-\vec{q}), \end{aligned} \quad \text{(A.23)}$$

$$E(\vec{k},\sigma',\sigma,1)_{l=j} = \int \frac{d^3q}{(2\pi)^3}\frac{4\pi}{q^2}\left(\sum_i\sum_l |\delta_l|^2\langle l|B_l(-q_\perp)|l\rangle\langle i|B_i(q_\perp)|i\rangle - \sum_i e^{-\frac{|q_\perp|^2}{2}}\right)$$
$$e^{\frac{k_\perp q_\perp^* - k_\perp^* q_\perp}{2}} e^{-\frac{|k_\perp|^2}{2}} F(n_{\sigma'}, n_{-\sigma'}=0, n_\sigma, n_{-\sigma}=0 : -\vec{q}) F(0,0,0,0:\vec{q}), \tag{A.24}$$

$$E(\vec{k},\sigma',\sigma,2) = \int \frac{d^3q}{(2\pi)^3}\frac{4\pi}{q^2}\left(\sum_i\sum_l |\delta_l|^2\langle i|B(-q_\perp)|i\rangle\langle l|B(q_\perp)|l\rangle - \sum_i e^{-\frac{|q_\perp|^2}{2}}\right)$$
$$e^{-\frac{|k_\perp|^2}{2}} F(0,0,0,0:\vec{q}) F(0,0,0,0:-\vec{q})\delta_{\sigma,\sigma'}. \tag{A.25}$$

A.2.1 $\nu = 2$

When the filling factor of the ground state is two, there are equal numbers of spins parallel to the magnetic field and anti-parallel to the magnetic field. In this case, we can split the excitation into two sets: singlet and triplet states. The singlet state results when $\delta = 1$. The excited electron will have the same spin orientation as when it was in the ground state. The correction terms are

$$E(\vec{k},\sigma',\sigma,1)_{i=j} = \int \frac{d^3q}{(2\pi)^3}\frac{4\pi}{q^2}\left(\left|\sum_i \langle i|B(k_\perp - q_\perp)|i\rangle\right|^2 - N\ e^{-\frac{|k_\perp - q_\perp|^2}{2}}\right) e^{-\frac{k_\perp q_\perp^* + k_\perp^* q_\perp}{2}}$$
$$F(n_{\sigma'}, n_{-\sigma'}=0,0,0:\vec{q}) F(0,0;n_\sigma, n_{-\sigma}=0:-\vec{q}), \tag{A.26}$$

$$E(\vec{k},\sigma',\sigma,1)_{l=j} = \int \frac{d^3q}{(2\pi)^3}\frac{4\pi}{q^2}\left(\left|\sum_i \langle i|B_i(q_\perp)|i\rangle\right|^2 - N\ e^{-\frac{|q_\perp|^2}{2}}\right) e^{\frac{k_\perp q_\perp^* - k_\perp^* q_\perp}{2}} e^{-\frac{|k_\perp|^2}{2}}$$
$$F(n_{\sigma'}, n_{-\sigma'}=0, n_\sigma, n_{-\sigma}=0:-\vec{q}) F(0,0,0,0:\vec{q}), \tag{A.27}$$

and

$$E(\vec{k},\sigma',\sigma,2) = \int \frac{d^3q}{(2\pi)^3}\frac{4\pi}{q^2}\left(\left|\sum_i \langle i|B(q_\perp)|i\rangle\right|^2 - N\ e^{-\frac{|q_\perp|^2}{2}}\right) e^{-\frac{|k_\perp|^2}{2}}$$
$$F(0,0,0,0:\vec{q}) F(0,0,0,0:-\vec{q})\delta_{\sigma,\sigma'}. \tag{A.28}$$

The term $|\sum_i \langle i|B(k)|i\rangle|^2$ evaluates to $N^2\delta_{\vec{k},0} \equiv N^2(2\pi)^2\delta^2(\vec{k})$. The corretion terms become

$$E(\vec{k},\sigma',\sigma,1)_{i=j} = \int \frac{d^3q}{(2\pi)^3}\frac{4\pi}{q^2}\left(N^2(2\pi)^2\delta^2(k_\perp + q_\perp) - N\ e^{-\frac{|k_\perp + q_\perp|^2}{2}}\right) e^{\frac{k_\perp q_\perp^* + k_\perp^* q_\perp}{2}}$$

$$F(n_{\sigma'}, n_{-\sigma'} = 0,0,0 : -\vec{q}) F(0,0; n_\sigma, n_{-\sigma} = 0 : \vec{q}), \tag{A.29}$$

$$\begin{aligned} E(\vec{k}, \sigma', \sigma, 1)_{l=j} &= \int \frac{d^3q}{(2\pi)^3} \frac{4\pi}{q^2} \left(N^2 (2\pi)^2 \delta^2(q_\perp) - N \; e^{-\frac{|q_\perp|^2}{2}} \right) e^{-\frac{k_\perp q_\perp^* - k_\perp^* q_\perp}{2}} e^{-\frac{|k_\perp|^2}{2}} \\ & F(n_{\sigma'}, n_{-\sigma'} = 0, n_\sigma, n_{-\sigma} = 0 : \vec{q}) F(0,0,0,0 : -\vec{q}), \end{aligned} \tag{A.30}$$

and

$$\begin{aligned} E(\vec{k}, \sigma', \sigma, 2) &= \int \frac{d^3q}{(2\pi)^3} \frac{4\pi}{q^2} \left(N^2 (2\pi)^2 \delta^2(q_\perp) - N \; e^{-\frac{|q_\perp|^2}{2}} \right) e^{-\frac{|k_\perp|^2}{2}} \\ & F(0,0,0,0 : \vec{q}) F(0,0,0,0 : -\vec{q}) \delta_{\sigma,\sigma'}. \end{aligned} \tag{A.31}$$

Once apparopriately normalized, the correction to the single particle energy for the charge density excitation is

$$\begin{aligned} E(\sigma', \sigma) &= e^{\frac{|k_\perp|^2}{2}} \int \frac{d^3q}{(2\pi)^3} \frac{4\pi}{q^2} \left(N(2\pi)^2 \delta^2(k_\perp + q_\perp) - \; e^{-\frac{|k_\perp + q_\perp|^2}{2}} \right) e^{\frac{k_\perp q_\perp^* + k_\perp^* q_\perp}{2}} \\ & F(n_{\sigma'}, n_{-\sigma'} = 0,0,0 : -\vec{q}) F(0,0; n_\sigma, n_{-\sigma} = 0 : \vec{q}) + \\ & \int \frac{d^3q}{(2\pi)^3} \frac{4\pi e^2}{q^2} \left(N(2\pi)^2 \delta^2(q_\perp) - \; e^{-\frac{|q_\perp|^2}{2}} \right) \\ & \Big\{ F(n_{\sigma'}, n_{-\sigma'} = 0, n_\sigma, n_{-\sigma} = 0 : \vec{q}) F(0,0,0,0 : -\vec{q}) e^{-\frac{k_\perp q_\perp^* - k_\perp^* q_\perp}{2}} - \\ & \delta_{\sigma,\sigma'} F(0,0,0,0 : \vec{q}) F(0,0,0,0 : -\vec{q}) \Big\}. \end{aligned} \tag{A.32}$$

We can now rearrange the terms in Eq. (A.32) so that we can identify the various contribution to the coulomb correction. We will group all the direct terms into one group and the exchange terms into the other group.

$$\begin{aligned} E(\sigma', \sigma) &= 2N \int \frac{dq_z}{k_\perp^2 + q_z^2} e^{-\frac{|k_\perp|^2}{2}} F(n_{\sigma'}, n_{-\sigma'} = 0,0,0 : \vec{k_\perp} - \vec{q_z}) \\ & F(0,0; n_\sigma, n_{-\sigma} = 0 : -(\vec{k_\perp} - \vec{q_z})) + \\ & 2N \int \frac{dq_z}{q_z^2} \Big\{ F(n_{\sigma'}, n_{-\sigma'} = 0, n_\sigma, n_{-\sigma} = 0 : \vec{q_z}) F(0,0,0,0 : -\vec{q_z}) - \\ & \delta_{\sigma,\sigma'} |F(0,0,0,0 : \vec{q_z})|^2 \Big\} - \\ & \int \frac{d^3q}{(2\pi)^3} \frac{4\pi}{q^2} \; e^{-\frac{|q_\perp|^2}{2}} \Big(F(n_{\sigma'}, n_{-\sigma'} = 0,0,0 : -\vec{q}) F(0,0; n_\sigma, n_{-\sigma} = 0 : \vec{q}) + \\ & e^{-\frac{k_\perp q_\perp^* - k_\perp^* q_\perp}{2}} F(n_{\sigma'}, n_{-\sigma'} = 0, n_\sigma, n_{-\sigma} = 0 : \vec{q}) F(0,0,0,0 : -\vec{q}) - \end{aligned}$$

$$\delta_{\sigma,\sigma'}|F(0,0,0,0:\vec{q})|^2\Big) \tag{A.33}$$

The first term in Eq. (A.33) is the so called random-phase approximation (RPA) term. The second term is the difference in the Hartree energy for an electron in the ground state and an electron in the excited state.

The triplet states are the results of $\delta = s_\xi, s_+$ and $\delta = s_-$, where $\hat{\xi}$ is the direction of magnetic field. For $\nu = 2$, we can evaluate just the case with $\delta = s_\xi$. The differences between the energies of states $\delta = s_+, s_-$ and $\delta = s_\xi$ are the respective Zeeman energy. In this case, the sum $\sum_i \delta_i \langle i|B(q_\perp)|i\rangle$ sums to zero because there are equal number of spin up electron as spin down electrons. The spin density energy is the same as the charge density energy except for the RPA term

$$\begin{aligned}
E(\sigma',\sigma) \;=\; & 2N\int \frac{dq_z}{q_z^2}\Big(F(n_{\sigma'},n_{-\sigma'}=0,n_\sigma,n_{-\sigma}=0:\vec{q_z})F(0,0,0,0:-\vec{q_z})- \\
& \delta_{\sigma,\sigma'}|F(0,0,0,0:\vec{q_z})|^2\Big) - \\
& \int \frac{d^3q}{(2\pi)^3}\frac{4\pi}{q^2}\; e^{-\frac{|q_\perp|^2}{2}}\Big(F(n_{\sigma'},n_{-\sigma'}=0,0,0:-\vec{q})F(0,0;n_\sigma,n_{-\sigma}=0:\vec{q})+ \\
& e^{-\frac{k_\perp q_\perp^* - k_\perp^* q_\perp}{2}}F(n_{\sigma'},n_{-\sigma'}=0,n_\sigma,n_{-\sigma}=0:\vec{q})F(0,0,0,0:-\vec{q}) - \\
& \delta_{\sigma,\sigma'}|F(0,0,0,0:\vec{q})|^2\Big)
\end{aligned} \tag{A.34}$$

A.2.2 $\nu = 1$

In the case of the filling factor of 1, the ground state is spin polarized with the spin aligned with the magnetic field. (This is contrary to the free-electron case because GaAs has negative g-factor.) Because the ground state is spin polarized, the spin flip up is not allowed. The spin-polarized ground state also implies that the charge density, with $\delta_i = 1$ and spin density , with $\delta_i = s_\xi$ have same correction to the single particle energy. The term $E(\vec{k},\sigma',\sigma,1)_{i=j}$ is zero for the spin flp excitation also for the same reason: the excited electron with flipped spin state is orthogonal to the spin states of all the ground state electrons. The excitation energy for the charge and spin

density exciataions is

$$
\begin{aligned}
E(\sigma',\sigma) &= 2N\int \frac{dq_z}{k_\perp^2+q_z^2} e^{-\frac{|k_\perp|^2}{2}} F(n_{\sigma'}, n_{-\sigma'}=0,0,0:\vec{k_\perp}-\vec{q_z}) \\
&\quad F(0,0;n_\sigma,n_{-\sigma}=0:-(\vec{k_\perp}-\vec{q_z}))+ \\
&\quad 2N\int \frac{dq_z}{q_z^2}\Big(F(n_{\sigma'},n_{-\sigma'}=0,n_\sigma,n_{-\sigma}=0:\vec{q_z})F(0,0,0,0:-\vec{q_z})- \\
&\quad \delta_{\sigma,\sigma'}|F(0,0,0,0:\vec{q_z})|^2\Big) - \\
&\quad \int \frac{d^3q}{(2\pi)^3}\frac{4\pi}{q^2}\ e^{-\frac{|q_\perp|^2}{2}}\Big(F(n_{\sigma'},n_{-\sigma'}=0,0,0:-\vec{q})F(0,0;n_\sigma,n_{-\sigma}=0:\vec{q})+ \\
&\quad e^{-\frac{k_\perp q_\perp^* - k_\perp^* q_\perp}{2}} F(n_{\sigma'},n_{-\sigma'}=0,n_\sigma,n_{-\sigma}=0:\vec{q})F(0,0,0,0:-\vec{q}) - \\
&\quad \delta_{\sigma,\sigma'}|F(0,0,0,0:\vec{q})|^2\Big) \qquad \text{(A.35)}
\end{aligned}
$$

The energy to the spin flip excitation, on the other hand , is

$$
\begin{aligned}
E(\sigma',\sigma) &= 2N\int \frac{dq_z}{q_z^2}\Big(F(n_{\sigma'},n_{-\sigma'}=0,n_\sigma,n_{-\sigma}=0:\vec{q_z})F(0,0,0,0:-\vec{q_z})- \\
&\qquad \delta_{\sigma,\sigma'}|F(0,0,0,0:\vec{q_z})|^2\Big) - \\
&\quad \int \frac{d^3q}{(2\pi)^3}\frac{4\pi}{q^2}\ e^{-\frac{|q_\perp|^2}{2}}\Big\{F(n_{\sigma'},n_{-\sigma'}=0,n_\sigma,n_{-\sigma}=0:\vec{q})F(0,0,0,0:-\vec{q}) \\
&\qquad e^{-\frac{k_\perp q_\perp^* - k_\perp^* q_\perp}{2}} - \delta_{\sigma,\sigma'}|F(0,0,0,0:\vec{q})|^2\Big\}. \qquad \text{(A.36)}
\end{aligned}
$$

Appendix B

Evaluation of $F(n_+, n_-; m_+, m_- : \vec{k})$

This appendix will derive the matrix elements needed in the evaluation of the effects of electron-electron interaction. The matrix element we would like to evaluate is

$$F(n_+, n_-; m_+, m_- : \vec{k}) = \langle n_+, n_- |\ e^{ik_z z} A(k_\perp) | m_+, m_- \rangle, \tag{B.1}$$

where we have defined $k_\perp = k_x + ik_y$. The operator $e^{ik_z z}A(k_\perp)$ can be written in terms of the raising and lowering hybrid ladder operators. The trick that will be used to evaluate $F(n_+, n_-; m_+, m_- : \vec{k})$ is to arrange the terms in $e^{ik_z z}A(k_\perp)$ so that all the lowering operators are to the right of the raising operators:

$$e^{ik_z z} A(k_\perp) = \Gamma\ \ e^{\gamma_+ a_+^\dagger}\ \ e^{\gamma_- a_-^\dagger}\ \ e^{-\gamma_+^* a_+}\ \ e^{-\gamma_-^* a_-}, \tag{B.2}$$

where $\Gamma, \gamma_\pm$ are defined as

$$\begin{aligned}
\Gamma &= exp\left[\frac{\ell_o^2}{4}(kx^2 + ky^2) - \frac{\ell_o^2}{4} ky^2 (sin^2(\theta)\frac{\Omega_+}{\omega_\perp} + cos^2(\theta)\frac{\Omega_-}{\omega_\perp}) \right. \\
&\quad \left. -\frac{\hbar}{4m\Omega_-}(k_x cos(\theta) - k_z sin(\theta))^2 - \frac{\hbar}{4m\Omega_+}(k_x sin(\theta) + k_z cos(\theta))^2 \right], \qquad \text{(B.3)} \\
\gamma_+ &= k_z cos(\theta)\sqrt{\frac{\hbar}{2m\Omega_+}} + \frac{\ell_o sin(\theta)}{\sqrt{2}}\left(k_x\sqrt{\frac{\omega_\perp}{\Omega_+}} - ik_y\sqrt{\frac{\omega_\perp}{\Omega_+}}\right), \qquad \text{(B.4)} \\
\gamma_- &= -k_z sin(\theta)\sqrt{\frac{\hbar}{2m\Omega_-}} + \frac{\ell_o cos(\theta)}{\sqrt{2}}\left(k_x\sqrt{\frac{\omega_\perp}{\Omega_-}} - ik_y\sqrt{\frac{\omega_\perp}{\Omega_-}}\right). \qquad \text{(B.5)}
\end{aligned}$$

The variables Ω_+, Ω_- and θ are introduced in the process of diagonalizing the the single particle Hamiltonian. They are defined as

$$\tan(2\theta) = -\frac{2\omega_{\|}\omega_{\perp}}{\tilde{\Omega}^2 - \omega_{\perp}^2}, \tag{B.6}$$

$$\Omega_{\pm} = \sqrt{\frac{\omega_{\perp}^2 + \tilde{\Omega}^2}{2} \pm \sqrt{\left(\frac{\omega_{\perp}^2 - \tilde{\Omega}^2}{2}\right)^2 + \omega_{\perp}^2\omega_{\|}^2}}. \tag{B.7}$$

Since the semi-classical states are the eigen-states of the lowering ladder operator, the expectation value of Eq. (B.2) between the semi-classical states can be evaluated easily: the lowering operators will simply return complex numbers when operating on the semi-classical states. It is easiest to evaluate Eq. (B.1) if we can make a transformation from the number eigen-states $|n_{\pm}\rangle$ to the semi-classical states $|alpha_{\pm}\rangle$.

B.1 Semi-Classical States

The semi-classical states are the eigen-states of the lowering ladder operator. They are defined as

$$a_{\pm}|\alpha_{\pm}\rangle = \alpha_{\pm}|\alpha_{\pm}\rangle. \tag{B.8}$$

In order to use the semi-classical states in the evaluation of Eq. (B.1), we need to be able to relate the semi-classical state to the number states. Consider an expansion of the semi-classical state, $|\alpha\rangle$, in terms of the number states, $|m\rangle$,

$$|\alpha\rangle = \sum_m c_m|m\rangle. \tag{B.9}$$

We need to evaluate the coefficients c_m. Let us operate on Eq. (B.9) with the lowering ladder operator

$$a|\alpha\rangle = \alpha|\alpha\rangle \tag{B.10}$$

$$= \sum_m \alpha c_m|m\rangle \tag{B.11}$$

$$= \sum_m c_m\sqrt{m}|m-1\rangle. \tag{B.12}$$

Since the $|m\rangle$ states are the states of a complete and orthonormal set, we must require that each coefficient of $|m\rangle$ in the sum be equal

$$c_{m+1} = \frac{\alpha}{\sqrt{m+1}} c_m \tag{B.13}$$

$$c_m = = \frac{\alpha^m}{\sqrt{m!}} c_0. \tag{B.14}$$

By substituting Eq. (B.14) into Eq. (B.9), the expansion is determined to within a constant

$$|\alpha\rangle = c_0 \sum_m \frac{\alpha^m}{\sqrt{m!}} |m\rangle. \tag{B.15}$$

The constant c_0 is chosen to be real and to normalize the state of $|\alpha\rangle$

$$1 = c_0^* c_0 \sum_m \frac{|\alpha|^2}{m!} \tag{B.16}$$

The sum on the right hand side of the equation is $e^{|\alpha|^2}$. The normalization constant to within a phase factor is

$$c_0 = e^{-\frac{|\alpha|^2}{2}}. \tag{B.17}$$

By substituting the appropriate value of c_0 into Eq. (B.15), we achieve the desired expansion of the semi-classical state:

$$|\alpha\rangle = \sum_m \frac{\alpha}{\sqrt{m!}} \; e^{-\frac{|\alpha|^2}{2}} |m\rangle. \tag{B.18}$$

The equation can be inverted to achieve the expansion of $|m\rangle$ in terms of the semi-classical states:

$$|m\rangle = \frac{1}{\pi} \int d^2\alpha \frac{\alpha^{*m}}{\sqrt{m!}} \; e^{-\frac{|\alpha|^2}{2}} |\alpha\rangle. \tag{B.19}$$

The semi-classical states are not the usual set of basis states in the sense that the semi-classical states are complete but not orthonormal. The over-lap between states corresponding to different eigen values is non-zero

$$\langle \beta \, | \alpha \rangle = e^{-\frac{|\alpha|^2 + |\beta|^2}{2}} \sum_m \frac{\beta^*}{\sqrt{m!}} \frac{\alpha}{\sqrt{m!}}. \tag{B.20}$$

The sum adds to an exponential

$$\langle\beta\,|\alpha\rangle = \; e^{-\frac{|\alpha|^2+|\beta|^2}{2}} \; e^{\alpha\beta^*}. \tag{B.21}$$

B.2 Evaluation of Matrix Elements

If we substitute Eq. (B.19) in Eq. (B.1), the problem is reduced to evaluating the matrix elements of $e^{ik_z z}A(k_\perp)$ between states $|\alpha_\pm\rangle$. We will define the matrix elements as

$$S(\beta_+,\beta_-;\alpha_+,\alpha_- : \vec{k}) = \langle\beta_+,\beta_-|\; e^{ik_z z}A(k_\perp)|\alpha_+,\alpha_-\rangle. \tag{B.22}$$

$F(n_+,n_-;m_+,m_- : \vec{k})$ can be written as a function of $S(\beta_+,\ beta_-;\alpha_+,\alpha_- : \vec{k})$:

$$\begin{aligned} F(n_+,n_-;m_+,m_- : \vec{k}) \;=\; & \frac{1}{\pi^4}\int d^2\beta_+ \int d^2\beta_- \int d^2\alpha_+ \int d^2\alpha_- S(\beta_+,\beta_-;\alpha_+,\alpha_- : k) \\ & \frac{\alpha_+^{*m_+}\alpha_-^{*m_-}\beta_+^{n_+}\beta_-^{n_-}}{\sqrt{m_+!m_-!n_+!n_-!}} \; e^{-\frac{|\alpha_+|^2+|\alpha_-|^2+|\beta_+|^2+|\beta_-|^2}{2}}. \end{aligned} \tag{B.23}$$

The two dimensional integrals can be done easily if we can evaluate the S matrix elements. This can be done easily since in Eq. (B.2) we have written all the lowering operators to the right of the raising operators. The effect of the raising and lowering operators on the semi-classical states is

$$f(a_\pm)|\alpha_\pm\rangle \;=\; f(\alpha_\pm)|\alpha_\pm\rangle \tag{B.24}$$

$$\langle\beta_\pm|g(a_\pm^\dagger) \;=\; g(\beta_\pm^*)\langle\beta_\pm| \tag{B.25}$$

The S matrix elements can now be written as

$$\begin{aligned} S(\beta_+,\beta_-;\alpha_+,\alpha_- : \vec{k}) \;&=\; \Gamma\langle\beta_+,\beta_-|\; e^{\gamma_+ a_+^\dagger} \; e^{\gamma_- a_-^\dagger} \; e^{-\gamma_+^* a_+} \; e^{-\gamma_-^* a_-}|\alpha_+,\alpha_-\rangle \\ &=\; \Gamma \; e^{\alpha_+\beta_+^*} \; e^{\alpha_-\beta_-^*} \; e^{\gamma_+\beta_+^*} \; e^{\gamma_-\beta_-^*} \; e^{-\gamma_+^*\alpha_+} \; e^{-\gamma_-^*\alpha_-}. \end{aligned} \tag{B.26}$$

By substituting Eq. (B.26) into Eq. (B.23) and do the four integrals, we arrive at the solution for $F(n_+, n_-; m_+, m_- : k)$

$$F(n_+, n_-; m_+, m_- : \vec{k}) = \frac{\Gamma \gamma_+^{n_+} \gamma_-^{n_-} (-\gamma_+^*)^{m_+} (-\gamma_-^*)^{m_-}}{\sqrt{m_+! m_-! n_+! n_-!}} \sum_{j}^{min(m_+, n_+)} \sum_{l}^{min(m_-, n_-)}$$
$$(-|\gamma_+|^2)^{-j} (-|\gamma_-|^2)^{-l} \frac{m_+! m_-! n_+! n_-!}{(n_+ - j)!(m_+ - j)! j! (n_- - l)!(m_- - l)! l!}. \quad \text{(B.27)}$$

Bibliography

[1] S. Adachi. GaAs, AlAs and $Al_xGa_{1-x}As$: Material parameters for use in research and device applications. *J. Appl. Phys.*, 58:R1, 1985.

[2] T. Ando. Inter-subband optical transitions in a surface space-charge layer. *Solid State Commun.*, 21:133, 1977.

[3] H.A. Bethe and R. Jackiw. *Intermediate Quantum Mechanics.* Benjamin-Cummings, Menlo Park, CA, third edition, 1986.

[4] L. Brey, N.F. Johnson, and B.I. Halperin. Optical and magneto-optical absorption in parabolic quantum wells. *Phys. Rev. B.*, 40:10647, 1989.

[5] H. Daembkes, editor. *Modulation-Doped Field Effect Transistors.* IEEE Press, New York, 1990.

[6] M. Dahl, D. Heiman, A. Pinczuk, B.B. Goldberg, L.N. Pfeiffer, and K.W. West. Suppression of ground-state optical recombination in the quantum hall regime. *Phys. Rev. B.*, 45:6957, 1992.

[7] J. Dempsey and B.I. Halperin. Magnetoplasma excitation in parabolic quantum wells : Hydrodynamic model. *Phys. Rev. B.*, 45:1719, 1992.

[8] D. Goldberg, B.B. Heiman, A. Pinczuk, L.N. Pfeiffer, and K. West. Optical investigation fo the integer and fractional quantum hall effects: Energy plateaus, intensity minima, and line splitting in band-gap emission. *Phys. Rev. Lett.*, 65:641, 1990.

[9] R.L. Greene and K.K. Bajaj. Effect of magnetic field on the energy levels of a hydrogenic impurity center in GaAs/$Ga_{1-x}Al_xAs$ quantum-well structures. *Phys. Rev. B.*, 31:913, 1985.

[10] E.G. Gwinn, P.F. Hopkins, A.J. Rimberg, R.M. Westervelt, M. Sundaram, and A.C. Gossard. Characterization of the electron gas in wide parabolic GaAs/$Al_xGa_{1-x}As$ quantum wells. *Phys. Rev. B.*, 41:10700, 1990.

[11] B. I. Halperin. Quantized hall conductance, current-carrying edge states, and the existence of extended states in a two-dimensional disordered potential. *Phys. Rev. B.*, 23:5632, 1981.

[12] J.P. Harbison, L.D. Peterson, and J. Levkoff. Precisely controlled compositional gradients in MBE grown AlGaAs/GaAs structures. *J. Cryst. Growth*, 81:34, 1987.

[13] D. Heiman, B.B. Goldberg, A. Pinczuk, C.W. Tu, A.C. Gossard, and J.H. English. Optical anomalies of the two-dimensional electron gas in the extremem magnetic quantum limit. *Phys. Rev. Lett.*, 61:605, 1988.

[14] P.F. Hopkins, A.J. Rimberg, E.G. Gwinn, R.M. Westervelt, M. Sundaram, and A.C. Gossard. Low-density high-mobility electron gas in wide parabolic GaAs/$Al_xGa_{1-x}As$ wells. *Appl. Phys. Lett.*, 57:2823, 1990.

[15] J.D. Jackson. *Classical Electrodynamics.* John Wiley & Sons, New York, second edition, 1975.

[16] J. K. Jain, S.A. Kivelson, and Nandini Trivedi. Scaling theory of the fractional quantum hall effect. *Phys. Rev. Lett.*, 64:1297, 1990.

[17] N.C. Jarosik, B.D. McCombe, B.V. Shanabrook, J. Comas, J. Ralston, and G. Wicks. Binding of shallow donor impurities in quantum-well structures. *Phys. Rev. Lett.*, 54:1283, 1985.

[18] C. Kallin and B.I. Halperin. Excitation from a filled landau level in the two-dimensional electron gas. *Phys. Rev. B.*, 30:5655, 1984.

[19] M. Kaloudis, K. Ensslin, A. Wixforth, M. Sundaram, English J.H., and A.C. Gossard. Resonant coupling of collective intra- and intersubband excitations in a parabolically confined electron sytem. *Phys. Rev. B.*, 46:12469, 1992.

[20] W. Kohn. Cyclotron resonance and de Hass-van Alphen oscillations of an interacting electron gas. *Physical Review*, 123:1242, 1961.

[21] R. B. Laughlin. Quantized hall conductivity in two dimensions. *Phys. Rev. B.*, 23:5632, 1981.

[22] L.B. Liao, D. Heiman, P.F. Hopkins, and A.C. Gossard. Inelastic-light-scattering study of magnetoplasma modes in a wide parabolic quantum wells. *Phys. Rev. B.*, 49:16825, 1994.

[23] A.H. MacDonald, H.C.A. Oji and S.M. Girvin. Magnetoplasmon excitations from partially filled Landau levels in two dimensions. *Phys. Rev. Lett.*, 55:2208, 1985.

[24] J. Menendez, A. Pinczuk, A.C. Gossard, M.G. Lamont, and F. Cerdeira. Light scattering in GaAs parabolic quantum wells. *Solid State Commun.*, 61:601, 1987.

[25] J.M. Mercy, B.D. McCombe, J. Beard, W. Ralston, and G. Wicks. Barrier impurity states in modulation doped AlGaAs/GaAs multi-quantum wells. *Surface Science*, 196:334, 1988.

[26] A. Pinczuk, B.S. Dennis, D. Heiman, C. Kallin, L. Brey, C. Tejedor, S. Schmitt-Rink, L. Pfeiffer, and K. West. Measurement of enhanced exchange of a spin-polarized 2d electron gas by inelastic light scattering. *Preprint*, 1992.

[27] A. Pinczuk, B.S. Dennis, L. Pfeiffer, and K. West. Observation of collective excitation in the fractional quantum hall efect. *Phys. Rev. Lett.*, 70:3983, 1993.

[28] A. Pinczuk, S. Schmitt-Rink, G. Danan, J.P. Valladares, L. Pfeiffer, and K. West. Large exchange interactions in the electron gas of GaAs quantum wells. *Phys. Rev. Lett.*, 63:1633, 1989.

[29] A. Pinczuk, J. P. Valladares, A.C. Gossard, J.H. English, C.W. Tu, L. Pfeiffer, and K. West. Observation of roton density of states in two-dimensional landua-level excitations. *Phys. Rev. Lett.*, 61:2701, 1988.

[30] R.E. Prange and S.M. Girvin, editors. *The Quantum Hall Effect.* Springer-Verlag, Berlin, second edition, 1990.

[31] A.A. Reeder, J.M. Mercy, and B.D. McCombe. Photoluminescence excitation spectroscopy of remotely doped wide parabolic GaAs/$Al_xGa_{1-x}As$ quantum wells. *IEEE Journal of Quantum Electronics*, 24:1690, 1988.

[32] F. Stern and S. Das Sarma. Electron energy levels in GaAs–$Ga_{1-x}Al_xAs$ hetrojunctions. *Phys. Rev. B.*, 30:840, 1984.

[33] M. Sundaram, S.A. Chalmers, P.F. Hopkins, and A.C. Gossard. New quantum structures. *Science*, 254:1326, 1991.

[34] D.C. Tsui, H.L. Stormer, and A.C. Gossard. Two-dimensional magnetotransport in the extreme quantum limit. *Phys. Rev. Lett.*, 48:1559, 1982.

[35] A.J. Turberfield, S.R. Haynes, P.A. Wright, R.A. Ford, R.G. Clark, J.F. Ryan, J.J. Harris, and C.T. Foxon. Optical detection of the integer and fractional quantum hall effects in GaAs. *Phys. Rev. Lett.*, 65:637, 1990.

[36] K. v. Klitzing, G. Dorda, and M. Pepper. New method for high-accuracy determination of the fine-structure constant based on quantized hall resistance. *Phys. Rev. Lett.*, 45:494, 1980.